Complex Langevin simulations of quantum systems with the sign problem

Mitsuaki Hirasawa

Department of Particle and Nuclear Physics, School of High Energy Accelerator Science,
The Graduate University for Advanced Studies, SOKENDAI,
1-1 Oho, Tsukuba, Ibaraki 305-0801, Japan

abstract

The non-perturbative dynamics plays important roles in quantum field theories and superstring theory. Monte Carlo calculation of the systems is one of the useful methods to study non-perturbative dynamics. There are many successful works. However, the usual Monte Carlo methods are not applicable, for example, in the Lorentzian metric case, theories with a θ term, theories at finite density, and so on. In such cases, since the Boltzmann weight becomes complex, it is not possible to interpret the weight as the probability. This problem is called the sign problem. Some methods to overcome the sign problem have been proposed. The complex Langevin method (CLM) is one of such methods. An advantage of the method compared with others is that the numerical cost for increasing the system size is reasonable.

This method was applied to many toy models, in which it worked well. However, the applications to physically interesting models are not so many. In our work, we apply the CLM to the gauge theories with a θ term and the Lorentzian type IIB matrix model.

As a validity test of the CLM for the gauge theories with a θ term, we first apply the CLM to the 2d U(1) gauge theory on the torus with a θ term which is solvable with finite lattice spacing and finite volume on an arbitrary manifold. We find that a naive implementation of the method fails because of the topological nature of the θ term. In order to circumvent this problem, we simulate the same theory on a punctured torus, which is equivalent to the original model in the infinite volume limit for $|\theta| < \pi$. Rather surprisingly, we find that the CLM works and reproduces the exact results for a punctured torus even at large θ, where the link variables near the puncture become very far from being unitary.

Since the application of the CLM to the 2d U(1) case is successful, we next apply the CLM to the 4d SU(2) case. There are interesting predictions for the phase structure around $\theta = \pi$ by using 't Hooft anomaly matching condition. Therefore our aim is to investigate the phase structure by the first principle calculation. We apply the CLM to the theory on a torus and find that, in the coarse lattice case, there is no freezing of topological charge. Although the CLM works well even at large θ, we cannot see the 2π periodicity due to the finite lattice spacing effects. Therefore, we need to decrease the lattice spacing. However, there is the freezing problem in the fine lattice case. We try to solve the problem by imposing the periodic boundary conditions We find that imposing the open boundary condition in all spatial directions alleviates the topology freezing sufficiently, and the CLM works well at large θ. However, the finite volume effect occurs as a drawback of the open boundary conditions. We also discuss the possible way to investigate the phase structure.

The Lorentzian type IIB matrix model was proposed as a non-perturbative formulation of superstring theory in 1996. The emergence of (3+1)-dimensional expanding space-time in the model is an intriguing phenomenon which was observed in Monte Carlo studies of

this model. In this work we investigate the space-time structure of the matrices generated by simulating this model and its simplified versions by using the hybrid Monte Carlo method, and find that the expanding part of the space is described essentially by the Pauli matrices. We argue that this is due to an approximation used in the simulation to avoid the sign problem, which actually amounts to replacing $e^{iS_{\rm b}}$ by $e^{\beta S_{\rm b}}$ ($\beta > 0$) in the partition function, where $S_{\rm b}$ is the bosonic part of the action.

In order to treat the weight $e^{iS_{\rm b}}$ appropriately, we use the CLM instead of the approximation to overcome the sign problem. We generalize the model by introducing two parameters which correspond to the Wick rotation on the world sheet and that in the target space. This generalized model interpolates among the Lorentzian case, the Euclidean case, and a model with $e^{\beta S_{\rm b}}$. We apply the CLM to this generalized model and find that the singular structure phase is not stable in the Lorentzian case. We also find that a new phase appears in the Lorentzian case where the CLM works well although the Boltzmann weight becomes a pure phase factor. In the bosonic model which is a simplified model of the type IIB matrix model, we cannot see the spontaneous breaking of SO(9) symmetry as in the case of the Euclidean bosonic model. We also discuss the possible scenario for emerging a regular space-time with the (3+1)-dimensional expanding behavior in the original model.

Contents

Chapter 1

Introduction

Sign problem is the main obstacle in studying the non-perturbative dynamics of some systems by using Monte Carlo simulations. The sign problem occurs in the Lorentzian metric cases, theories with a θ term, theories at finite density, and so on. In such cases, since the Boltzmann weight becomes complex, it is not possible to interpret the weight as the probability. Therefore, usual Monte Carlo methods are not applicable. This problem is called the sign problem.

Some methods to overcome the sign problem have been proposed. For example, the complex Langevin method [1, 2, 3, 4, 5, 6], the tensor renormalization method [7, 8, 9, 10, 11], the generalized Lefschetz thimble method [12, 13, 14, 15, 16, 17], the path optimization method[18, 19, 20, 21], and so on. Each method has its pros and cons. In this thesis, we mainly focus on the complex Langevin method (CLM). An advantage of the method compared with others is that the numerical cost for increasing the system size is reasonable. This method was applied to many toy models, in which they worked well. However, the applications for physically interesting models are not so many.

In this thesis, we apply the CLM to gauge theories with a θ term and the Lorentzian type IIB matrix model.

1.1 Gauge theories with a θ term

The θ term provides an interesting avenue of research in quantum field theories. Due to its topological nature, its effects on physics should be genuinely nonperturbative, if present at all. In particular, it does not affect the equation of motion, which implies that θ is a parameter that does not exist in the corresponding classical theory. For instance, the θ term in QCD is given by $S_\theta = -i\theta Q$, where Q is the topological charge defined by

$$Q = \frac{1}{32\pi^2}\epsilon_{\mu\nu\rho\sigma}\int d^4x \,\mathrm{tr} F_{\mu\nu}F_{\rho\sigma} \ , \tag{1.1.1}$$

which takes integer values on a compact space. The θ term breaks parity and time-reversal symmetries, and hence the CP symmetry. This leads to a non-vanishing electric dipole

moment of a neutron, which is severely restricted by experiments. The current upper bound on θ thus obtained is $|\theta| \lesssim 10^{-10}$ [22, 23], which is extremely small although there is no reason for it theoretically. This is a naturalness problem known as the strong CP problem.

A popular solution to this problem is the Peccei-Quinn mechanism [24, 25, 26, 27], which introduces axions as a pseudo Nambu-Goldstone boson of a hypothetical global $\mathrm{U}(1)_{\mathrm{PQ}}$ symmetry. In this mechanism, the potential for the axions induced by QCD chooses a CP invariant vacuum automatically. Recently, gauge theories with a θ term have attracted attention also from the viewpoint of the 't Hooft anomaly matching condition [28, 29, 30] and the gauge-gravity correspondence [31, 32, 33, 34]. In particular, there is an interesting prediction for a phase transition at $\theta = \pi$, which claims that either spontaneous CP breaking or deconfinement should occur there [28, 29, 35]. In order to investigate gauge theories from first principles in the presence of a θ term motivated either by the physics related to axions or by the recent predictions, one needs to perform non-perturbative calculations based on Monte Carlo methods. However, this is known to be extremely difficult because the θ term appears as a purely imaginary term in the Euclidean action S. The Boltzmann weight e^{-S} becomes complex, and one cannot interpret it as the probability distribution as one does in Monte Carlo methods.

One can still use the reweighting method by treating the phase of the complex weight as a part of the observable. In the case at hand, this amounts to obtaining the histogram of the topological charge at $\theta = 0$ and taking an average over the topological sectors characterized by the integer Q with the weight $\mathrm{e}^{i\theta Q}$. Various results obtained in this way are nicely reviewed in Ref. [36]. Clearly, the calculation becomes extremely difficult due to huge cancellations between topological sectors when topological sectors with $|Q| \gg \pi/|\theta|$ make significant contributions to the partition function, which occurs either for $|\theta| \sim \pi$ or for smaller $|\theta|$ with sufficiently large volume.

1.1.1 2D U(1) lattice gauge theory with a θ term

In chapter 3, we apply the CLM to the 2D U(1) lattice gauge theory with a θ term on the torus [37]. The model can be solved analytically with finite lattice spacing and finite volume on an arbitrary manifold [38, 39, 40]. Therefore this model is a useful testing ground for new methods [38, 41, 42, 43, 44] aiming at solving the sign problem. By using the reweighting method [42], for instance, one can only reach $\theta \sim 2.2$ with a 16×16 lattice, and in particular, it seems almost impossible to approach $\theta = \pi$ by this method. Note also that the region of θ that can be explored by this method shrinks to zero as one increases the lattice size.

We find that a naive implementation of the CLM fails. The reason for this is that the configurations that appear when the topology change occurs during the Langevin process necessarily result in a large drift term. Due to this fact, the criterion [6] for the validity

of the method based on the histogram of the drift term cannot be satisfied. If one tries to suppress the appearance of the problematic configurations by approaching the continuum limit, the criterion can be satisfied, but the topology change does not occur during the Langevin process, hence the ergodicity is lost.

In order to cure this problem, we introduce a puncture on the torus, which makes the base manifold noncompact. We have obtained exact results for this punctured model as well. Even in the continuum limit, the topological charge is no longer restricted to integer values and the 2π periodicity in θ does not hold. However, if we take the infinite volume limit with $|\theta| < \pi$, one cannot distinguish the model from the original non-punctured model as far as the observables that make sense in that limit are concerned. Note that in that limit, the topological charge can take arbitrarily large values and therefore it does not really matter whether it is an integer or not.

On the other hand, the situation of the complex Langevin simulation changes drastically for the punctured model. The topology change occurs freely and the appearance of the problematic configurations can be suppressed by simply approaching the continuum limit. Thus the criterion for the validity of the CLM is met without losing the ergodicity, and we are able to reproduce the exact results for the punctured model.

The most striking aspect of our results is that the CLM works even if the link variables close to the puncture become very far from being unitary. This can happen because the direct effect of the θ term on the complex Langevin dynamics is actually concentrated on these link variables. While the link variables are allowed to be non-unitary in the CLM in general in order to include the effects of the complex action, all the previous work suggested that the condition for the validity cannot be satisfied unless the non-unitarity is sufficiently suppressed. Precisely for this reason, the gauge cooling [45, 5, 6] was invented as a crucial technique in applying the CLM to gauge theories. In fact, we also use the gauge cooling in our simulation, but the link variables close to the puncture nevertheless become far from being unitary when θ or the physical volume gets large. Yet the criterion for the drift term is not violated and the exact results are perfectly reproduced.

1.1.2 4D SU(2) lattice gauge theory with a θ term

In chapter 4, we study the 4D SU(2) gauge theory with a θ term. In pure SU(2) gauge theory, there is a mixed 't Hooft anomaly between CP and the center symmetry at $\theta = \pi$. Due to the 't Hooft anomaly matching condition, there are some constraints on the phase structure. Therefore, some possible phase diagrams are expected depending on the nature of the vacuum at $\theta = \pi$ [28].

Assuming that the theory is in the confined phase at the low temperature, the condition indicates that the CP symmetry should be spontaneously broken in the confined phase because the center symmetry is preserved. Therefore the following relation should be

satisfied

$$T_{\rm dec}(\theta = \pi) \leq T_{\rm CP}, \tag{1.1.2}$$

where $T_{\rm dec}(\theta = \pi)$ is the critical temperature for the confinement-deconfinement phase transition at $\theta = \pi$.

The holographic Yang-Mills model with $N \gg 1$ supports $T_{\rm dec}(\theta = \pi) = T_{\rm CP}$ scenario [33]. On the other hand, softly-broken $\mathcal{N} = 1$ supersymmetric SU(2) Yang-Mills theory supports $T_{\rm dec}(\theta = \pi) < T_{\rm CP}$ scenario [46]. Therefore, our aim is to determine the phase diagram by the first principle calculation. Since there is the sign problem, we apply the CLM to the 4D SU(2) lattice gauge theory with a θ term.

First, we naively apply the CLM to the theory, and we find that, unlike the case of the 2D U(1) model, there is a region where the simulations are free from both the topology freezing problem and the wrong convergence problem for $|\theta| < 2\pi$. However, we cannot see the 2π periodicity in this region due to the large UV fluctuations. Since we cannot use a cooling procedure such as the gradient flow in the CLM, we need to decrease the lattice spacing to see the 2π periodicity. We find that, in the fine lattice case, the topology freezing problem also occurs in the 4D SU(2) case.

It is known that the open boundary conditions alleviate the topology freezing. Therefore, we impose the boundary conditions and find that the open boundaries for all spatial directions alleviate the problem sufficiently. The criterion is satisfied for $|\theta| < 2\pi$ also in this case. However, we find that the finite volume effects occur as a drawback of the open boundary condition. We will discuss a possible way to investigate the phase diagram.

1.2 The Lorentzian type IIB matrix model

Superstring theory is one of the promising candidates for quantum gravity. The theory is defined on 10d instead of 4d space-time due to the consistency. One of the most amazing things for the theory is that all of the four fundamental interactions are treated in one quantum theory. However, there are still many open problems that must be answered. One of the problems in superstring theory is the relation between the 4d universe and the 10d space-time. Compactification is a procedure to obtain the 4d space-time from the 10d space-time. However, there is an enormous number of perturbative vacua. This circumstance is called the string landscape. It is difficult to determine the vacuum which actually describes our universe.

The type IIB matrix model was proposed as a non-perturbative formulation of superstring theory [47]. The action of the model is formally obtained by the dimensional reduction [48] of the action for 10d $\mathcal{N} = 1$ SYM theory to 0d [49]. Therefore, in this model, the space-time does not exist a priori, and it emerges from dynamical degrees of the matrices. There is evidence that the model is considered as one of the promising candidates for the non-perturbative formulation. One reason is that this model can

be interpreted as the matrix regularization of the type IIB matrix model in the Schild gauge [50]. Another reason is that this model describes the well known interaction between D-branes. In addition, this model reproduces the light-cone string filed theory [51] in the large N limit [52]. Therefore, this model has the potential to clarify a possible non-perturbative mechanism for dynamical compactification in superstring theory.

The Euclidean version of the theory was investigated, and the SSB of SO(10) symmetry was suggested by some approaches [53, 54, 55, 56, 57, 58, 59]. However, latest calculation based on the CLM suggested that the SO(10) symmetry spontaneously breaks to SO(3) instead of SO(4).

These results provided a strong motivation to study the Lorentzian type IIB matrix model. In the previous works, the Monte Carlo simulation of this model was performed, and interesting results are obtained. At some point in time, the SO(9) symmetry spontaneously breaks to SO(3) [60]. After the SSB, the 3d space expands exponentially in early time [61]. And the expansion law changes from exponential to power-law as time proceeds [62]. These results are interesting also from the viewpoint of cosmology. However, the structure of the space has not been investigated in detail yet.

In chapter 5, we study the space-time structure in detail [63]. In order to study the space-time structure, we investigate how the space spreads in the radial direction. We find that the space is essentially described by the Pauli matrices. Namely, the space is actually more like a fuzzy sphere. We call this structure the Pauli matrix structure. We also observed the situation remains in the late time or in the continuum limit. This structure is different from the space-time we observe. We consider that the cause of the problem is an approximation that was used to avoid the sign problem. The approximation corresponds to replacing e^{iS} by $e^{\beta S}$ (β is a real positive value) in the partition function. It is expected that, when the complex-valued weight is appropriately treated, the smooth structure dynamically appears without losing the (3+1)d expanding behavior.

In chapter 6, we use the CLM to overcome the sign problem instead of the approximation which was used so far. We generalize the model by introducing two parameters that correspond to the Wick rotation on the world sheet and that in the target space. This generalized model interpolates among the Lorentzian case, the Euclidean case, and a model with $e^{\beta S_{\rm b}}$. We applied the CLM to the generalized model, and find that a new phase appears at the Lorentzian case. In this phase, continuous space appears, however, there is no clear expansion and the SSB either yet in this preliminary study. We also find that the new phase is smoothly connected to a phase that appears in the Euclidean model. We also discuss, the possible scenario for the emergence of expanding (3+1)d space-time.

Chapter 2

Sign problem

First of all, we consider the case of a real-valued action $S(x) \in \mathbb{R}$ where x is a set of real variables $x = (x_1, x_2, ..., x_N) \in \mathbb{R}^N$. The partition function is given by

$$Z = \int dx e^{-S(x)}. \tag{2.0.1}$$

In usual Monte Carlo case, we consider the Boltzmann weight $e^{-S(x)}$ as a probability and generate configurations under the probability:

$$P(x) \propto e^{-S(x)}. \tag{2.0.2}$$

The expectation values of a observable $\mathcal{O}(x)$ is calculated by the ensemble average as

$$\langle \mathcal{O}(x) \rangle = \frac{1}{N_{\text{config}}} \sum_{n=1}^{N_{\text{config}}} \mathcal{O}_n(x), \tag{2.0.3}$$

where N_{config} is the number of configurations.

However, in a complex-valued action $S(x) \in \mathbb{C}$ case, since the Boltzmann weight becomes complex, it is impossible to interpret the weight as the probability. This problem is called "sign problem". In principle, we can calculate the expectation value of the observable $\mathcal{O}(x)$ by using the reweighting method,

$$\langle \mathcal{O}(x) \rangle = \frac{\langle \mathcal{O}(x) e^{-i \operatorname{Im}(S(x))} \rangle_{e^{-\operatorname{Re}(S(x))}}}{\langle e^{-i \operatorname{Im}(S(x))} \rangle_{e^{-\operatorname{Re}(S(x))}}} \tag{2.0.4}$$

where the brackets of the right-hand side are expectation value evaluated by using configurations which are obtained under the weight $e^{-\operatorname{Re}(S(x))}$. This method is useful when the phase of the weight does not highly oscillate. However, when the phase highly oscillates the denominator and the numerator become very small, and we need to obtain the finite value from two very small values. In order to do that, we need a very large number of configurations. Thus the reweighting method is not useful in that situation.

2.1 Review of the complex Langevin method

The real Langevin method was introduced by Parisi and Wu in [64] as a stochastic quantization approach to quantum field theories. This method widely used in particle physics. However, in general, we cannot use this method for systems with the sign problem.

In 1983, Klauder and Parisi proposed the complex Langevin method independently as a method to overcome the sign problem [1, 2]. After the proposals, the method applied many systems, and a problem that the method sometimes gives wrong results was reported. This problem is called as the wrong convergence problem. The mechanism of this problem was not understood completely. Due to this situation, results obtained by this method was not reliable and the application of the method was limited.

Recently, the conditions for the correct convergence was studied in [3], and a practical criterion for correct convergence was proposed in [6]. After the breakthrough, the method applied many systems.

2.1.1 Real Langevin method

First, we review the real Langevin method. Therefore, we consider a system with a real-valued action $S(x) \in \mathbb{R}$. In this method, the configuration is generated by the Langevin equation as

$$x_i(t + \Delta t) = x_i(t) - \Delta t \frac{\partial S(x)}{\partial x} + \sqrt{(\Delta t)}\eta_i(t), \tag{2.1.1}$$

where t is a fictitious time so-called the Langevin time, Δt is the Langevin step size, and $\eta_i(t)$ is the Gaussian noise. The noise satisfies

$$\langle \eta_i(s)\eta_j(t) \rangle_\eta = 2\delta_{i,j}\delta_{s,t}, \tag{2.1.2}$$

where the expectation value $\langle \cdots \rangle_\eta$ is defined by

$$\langle \cdots \rangle_\eta = \frac{\int \prod_k d\eta(t_k) \cdots e^{-\frac{1}{4}\Delta t \sum_k \eta^2(t_k)}}{\int \prod_k d\eta(t_k) e^{-\frac{1}{4}\Delta t \sum_k \eta^2(t_k)}}. \tag{2.1.3}$$

Here we consider an arbitrary $f(x)$ and its expectation value

$$\big\langle f\big(x(t)\big) \big\rangle_\eta = \int dx f(x) P(x;t), \tag{2.1.4}$$

where $P(x;t)$ is the probability distribution of $x(t)$ defined by

$$P(x;t) = \left\langle \prod_i \delta\Big(x_i - x_i(t) \Big) \right\rangle_\eta. \tag{2.1.5}$$

If we consider the evolution of $f(x)$, one obtains

$$\begin{aligned}\left\langle f\big(x(t+\Delta t)\big)\right\rangle_\eta - \left\langle f\big(x(t)\big)\right\rangle_\eta &= \left\langle \frac{\partial f}{\partial x_i}\left(-\Delta t\frac{\partial S}{\partial x_i}\right) + \frac{1}{2}\frac{\partial^2 f}{\partial x_i \partial x_j}(\sqrt{\Delta t})^2\eta_i(t)\eta_j(t)\right\rangle_\eta + O\left(\Delta t^2\right) \\ &= \Delta t\int dx\left(-\frac{\partial f}{\partial x_k}\frac{\partial S}{\partial x_k} + \frac{\partial^2 f}{\partial x_k^2}\right)P(x;t) + O\left(\Delta t^2\right) \\ &= \Delta t\int dx f(x)\frac{\partial}{\partial x_k}\left(\frac{\partial S}{\partial x_k} + \frac{\partial}{\partial x_k}\right)P(x;t) + O\left(\Delta t^2\right).\end{aligned} \tag{2.1.6}$$

Using (2.1.4), this quantity should be rewritten as

$$\left\langle f\big(x(t+\Delta t)\big)\right\rangle_\eta - \left\langle f\big(x(t)\big)\right\rangle_\eta = \int dx f(x)\Big(P(x;t+\Delta t) - P(x;t)\Big). \tag{2.1.7}$$

Comparing (2.1.6) and (2.1.7), one obtains

$$P(x;t+\Delta t) - P(x;t) = \Delta t\frac{\partial}{\partial x_k}\left(\frac{\partial S}{\partial x_k} + \frac{\partial}{\partial x_k}\right)P(x;t) + O\left(\Delta t^2\right). \tag{2.1.8}$$

(2.1.8) is the discretized version of the Fokker-Planck equation [1]. After the thermalization, the probability distribution is independent from t, therefore, the distribution is obtained by solving

$$\Delta t\frac{\partial}{\partial x_k}\left(\frac{\partial S}{\partial x_k} + \frac{\partial}{\partial x_k}\right)P(x) + O\left(\Delta t^2\right) = 0, \tag{2.1.9}$$

where $P(x)$ is the time independent probability distribution. The solution is

$$P(x) = e^{-S(x)+O(\Delta t)}. \tag{2.1.10}$$

Therefore, in the Langevin process, the configurations are generated under this probability.

2.1.2 Complex Langevin method

Next we review the complex Langevin method. In the CLM, a real variable x_i is promoted to a complex variable $z_i \in \mathbb{C}$:

$$x_i \to z_i = x_i + iy_i \tag{2.1.11}$$

This variable is updated by the complex Langevin equation:

$$z_i(t+\Delta t) = z_i(t) - \Delta t\frac{\partial S(z)}{\partial z_i} + \sqrt{(\Delta t)}\eta_i(t), \tag{2.1.12}$$

[1] The Fokker-Plank equation

$$\frac{\partial P(x;t)}{\partial t} = \frac{\partial}{\partial x_k}\left(\frac{\partial S}{\partial x_k} + \frac{\partial}{\partial x_k}\right)P(x;t)$$

is obtained by taking $\Delta t \to 0$ limit of (2.1.8).

where t is a fictitious time so-called the Langevin time, Δt is the Langevin step size, and $\eta_i(t)$ is the Gaussian noise. $\eta_i(t)$ is construct from two independent real-valued Gaussian noise as

$$\eta_i(t) = \sqrt{c_{\mathrm{R}}}\eta_i^{(\mathrm{R})}(t) + i\sqrt{c_{\mathrm{I}}}\eta_i^{(\mathrm{I})}(t), \tag{2.1.13}$$

where $\eta_{i,\mathrm{R}}(t)$ and $\eta_{i,\mathrm{I}}(t)$ satisfy

$$\begin{aligned}
\langle \eta_i^{(\mathrm{R})}(s)\eta_j^{(\mathrm{R})}(t)\rangle_\eta &= 2\delta_{i,j}\delta_{s,t} \ , \\
\langle \eta_i^{(\mathrm{I})}(s)\eta_j^{(\mathrm{I})}(t)\rangle_\eta &= 2\delta_{i,j}\delta_{s,t} \ , \\
\langle \eta_i^{(\mathrm{R})}(s)\eta_j^{(\mathrm{I})}(t)\rangle_\eta &= 0 \ ,
\end{aligned} \tag{2.1.14}$$

where the expectation value $\langle\cdots\rangle_\eta$ is defined by

$$\langle\cdots\rangle_\eta = \frac{\int\prod_k d\eta^{(\mathrm{R})}(t_k)d\eta^{(\mathrm{I})}(t_k)\cdots e^{-\frac{1}{4}\Delta t\sum_k\{\eta^{(\mathrm{R})}(t_k)^2+\eta^{(\mathrm{I})}(t_k)^2\}}}{\int\prod_k d\eta^{(\mathrm{R})}(t_k)d\eta^{(\mathrm{I})}(t_k)e^{-\frac{1}{4}\Delta t\sum_k\{\eta^{(\mathrm{R})}(t_k)^2+\eta^{(\mathrm{I})}(t_k)^2\}}}. \tag{2.1.15}$$

The coefficients $\sqrt{c_{\mathrm{R}}}$ and $\sqrt{c_{\mathrm{I}}}$ in (2.1.13) should be satisfy $c_{\mathrm{I}} \geq 0$ and $c_{\mathrm{R}} - c_{\mathrm{I}} = 1$.

The time evolution of the expectation value of a holomorphic observable $\mathcal{O}(x+iy)$ is given by

$$\big\langle \mathcal{O}\big(x(t+\Delta t)+iy(t+\Delta t)\big)\big\rangle_\eta = \int dxdy\mathcal{O}_{\Delta t}(x+iy)P(x,y;t), \tag{2.1.16}$$

where $\mathcal{O}_{\Delta t}(x+iy)$ is defined as

$$\mathcal{O}_{\Delta t}(x+iy) = \frac{1}{2\pi}\int d\eta^{(\mathrm{R})}d\eta^{(\mathrm{I})}e^{-\frac{1}{4}\{(\eta^{(\mathrm{R})})^2+(\eta^{(\mathrm{I})})^2\}}\mathcal{O}(z+\Delta t v(z)+\sqrt{\Delta t}\eta), \tag{2.1.17}$$

where $v(z)$ is the drift term defined by

$$v(z) = \frac{\partial S(z)}{\partial z}. \tag{2.1.18}$$

Note that we assume $v(z)$ is a holomorphic quantity. We expand (2.1.17) with respect to Δt and we perform the integration for η, then we obtain

$$\mathcal{O}_{\Delta t}(z) = \sum_{n=0}^{\infty}\frac{1}{n!}(\Delta t)^n : L^n : \mathcal{O}(z), \tag{2.1.19}$$

where L is defined by

$$L = \left(\mathrm{Re}\, v_i(z) + c_{\mathrm{R}}\frac{\partial}{\partial x_i}\right)\frac{\partial}{\partial x_i} + \left(\mathrm{Im}\, v_i(z) + c_{\mathrm{I}}\frac{\partial}{\partial y_i}\right)\frac{\partial}{\partial y_i}, \tag{2.1.20}$$

and $:\cdots:$ means that the operators are ordered in such a way that derivative operators appear on the right. Since the observable is holomorphic quantity, we obtain

$$\begin{aligned}
L\mathcal{O}(z) &= \left(v_i(z) + (c_{\mathrm{R}} - c_{\mathrm{I}})\frac{\partial}{\partial z_i}\right)\frac{\partial\mathcal{O}}{\partial z_i} \\
&= \tilde{L}\mathcal{O}(z)
\end{aligned} \tag{2.1.21}$$

Using (2.1.19) and (2.1.21) in (2.1.16), we obtain

$$\left\langle \mathcal{O}\big(x(t+\Delta t)+iy(t+\Delta t)\big)\right\rangle_\eta = \sum_{n\ 0}^{\infty} \frac{1}{n!}(\Delta t)^n \int dxdy \left(: \tilde{L}^n : \mathcal{O}(z)\right) P(x,y;t). \quad (2.1.22)$$

If (2.1.22) is valid, we can neglect higher order terms for sufficiently small Δt as

$$\begin{aligned} &\left\langle \mathcal{O}\big(x(t+\Delta t)+iy(t+\Delta t)\big)\right\rangle_\eta \\ &= \left\langle \mathcal{O}\big(x(t)+iy(t)\big)\right\rangle_\eta + \Delta t \int dxdy \left(\tilde{L}\mathcal{O}(z)\right) P(x,y;t) + O\left((\Delta t)^2\right). \end{aligned} \quad (2.1.23)$$

We consider the condition for the validity of the expansion (2.1.22) to have a finite convergence radius. Here we consider the magnitude of the drift term defined as

$$u(z) = \max_i |v_i(z)| \quad (2.1.24)$$

which has the largest contribution to the radius. The integral in (2.1.22) involves

$$\int dxdyu(z)^n P(x,y;t) = \int_0^\infty duu^n p(u,t), \quad (2.1.25)$$

where the probability distribution of the magnitude of the drift term is defined as

$$p(u,t) = \int dxdy\delta(u(z)-u)P(x,y;t). \quad (2.1.26)$$

If the $p(u,t)$ is suppressed faster than exponential, the expansion (2.1.22) has a finite convergence radius. Therefore, it is needed for the correct convergence that $p(u,t)$ falls off faster than exponential in the CLM.

It is better to set $\sqrt{c_{\rm I}} = 0$, because the fluctuation for the imaginary direction sometimes causes a large excursion from real-value, that is one of the reasons for the wrong convergence [3, 4, 65]. Therefore, the rest of this thesis, we set $c_{\rm R} = 1$ and $c_{\rm I} = 0$.

2.2 Some techniques in the complex Langevin method

There are two main reasons for the failure of the CLM. One is that when the variables have a large excursion in the imaginary direction, the CLM sometimes fails. This problem is called the excursion problem. The other is that when the drift term has singularities if the complexifyed variables approach the singularities frequently the CLM fails. This problem is called the singular drift problem.

There are some techniques to avoid these problems. Here we explain the adaptive step size algorithm, the gauge cooling technique, and the deformation technique.

2.2.1 Adaptive step size

The large drift term is a trigger for that the variables to go away from the real value. If the large drift terms appear frequently the CLM fails. Choosing a small Langevin step size is one of the ways to avoid the excursion problem, however, this small Langevin step makes the simulation inefficiency. The adaptive step size algorithm [66] is a method to avoid the excursion problem efficiently.

In the adaptive step size algorithm, the step size is decreased when the large drift term appears. Therefore, we choose the step size as

$$\Delta t = \begin{cases} \Delta t_0 & \text{for } u < v_0 \ , \\ \dfrac{v_0}{u}\Delta t_0 & \text{otherwise} \ , \end{cases} \tag{2.2.1}$$

where Δt_0 is the default stepsize, u is the magnitude of drift term, and v_0 is the threshold for the magnitude of drift term.

2.2.2 Gauge cooling

Instead of the real variable x, here we consider a dynamical variable U which belongs to a gauge group G, namely $U \in G$. In the CLM, we "complexify" the variable $U \in G$ to $\mathcal{U} \in H$ because the drift term belongs to H when the system has the sign problem. For example, if G is SU(3) then H becomes $\mathrm{SL}(3, \mathbb{C})$. When $\mathcal{U}$ has a large excursion from the original group G large drift term may appear frequently, as the result, the CLM fails.

The idea of gauge cooling [45] is to reduce the deviation of the complexifyed variables from the original gauge group as much as possible by making gauge transformations corresponding to the complexified group H after each Langevin step. The details of the technique are shown in 3.2.2 and 4.2.1.

It is proofed that this procedure does not affect the holomorphic observables. Moreover, this procedure can be added without affecting the argument for justifying the CLM as demonstrated explicitly in Refs. [5, 6]. Recently, the mechanism of the gauge cooling for stabilizing the complex Langevin simulation has been investigated [67].

2.2.3 Deformation

When the theory has fermion $\mathrm{Tr}\,\log M$ is included in the effective action which is obtained after the path integration for fermionic variables. In the Langevin simulation, we need to evaluate the drift term for $\mathrm{Tr}\,\log M$ which is $\mathrm{Tr}\,(M^{-1}\frac{\partial M}{\partial x})$ where x is a dynamical variable. Therefore, if the Dirac operator M has near-zero eigenvalues the drift term becomes large. If such drift terms appear frequently the CLM fails, that problem is called the singular drift problem.

In order to avoid the near-zero eigenvalues, we introduce the additional term like a fictitious mass term to the action of the system. This additional term is called the defor-

mation term. Since this term modifies the theory, extrapolation for vanishing deformation term. The details of the algorithm are shown in 6.3.2.

Chapter 3

2D U(1) lattice gauge theory with a θ term

3.1 Lattice formulation of the 2D U(1) gauge theory with a θ term

In this section, we review pure 2D U(1) gauge theory with a θ term and discuss how to define it on a lattice.

In the continuum 2D U(1) gauge theory on a Euclidean space, the action for the gauge field $A_\mu(x)$ ($\mu = 1, 2$) is given by

$$S_g = \frac{1}{4g^2} \int d^2x \, (F_{\mu\nu})^2 \ , \tag{3.1.1}$$

where g is the gauge coupling constant and $F_{\mu\nu}$ is the field strength defined as

$$F_{\mu\nu} = \partial_\mu A_\nu(x) - \partial_\nu A_\mu(x) \ . \tag{3.1.2}$$

We add a θ term

$$S_\theta = -i\theta Q \tag{3.1.3}$$

in the action, where Q is the topological charge defined by

$$Q = \frac{1}{4\pi} \int d^2x \, \epsilon_{\mu\nu} F_{\mu\nu} \ , \tag{3.1.4}$$

which takes integer values if the space is compact.

We put this theory on a 2D torus, which is discretized into an $L \times L$ periodic lattice with the lattice spacing a. On the lattice, we define the link variables $U_{n,\mu} \in \mathrm{U}(1)$, where $n = (n_1, n_2)$ labels the lattice site as $x_\mu = a n_\mu$. We also define the plaquette

$$P_n = U_{n,\hat{1}} U_{n+\hat{1},2} U^{-1}_{n+\hat{2},1} U^{-1}_{n,2} \ , \tag{3.1.5}$$

where $\hat{\mu}$ is a unit vector in the μ direction. This plaquette is invariant under the gauge transformation:

$$U_{n,\hat{\mu}} \mapsto g_n \, U_{n,\hat{\mu}} \, g_{n+\hat{\mu}}^{-1}. \tag{3.1.6}$$

Here we write $U_{n,\mu}^{-1}$ instead of $U_{n,\mu}^{\dagger}$, which will be important later in applying the CLM, where we complexify the dynamical variables respecting holomorphicity.

The lattice counterpart of the field strength (3.1.2) can be defined as

$$F_{n,12} = \frac{1}{ia^2} \log P_n \ , \tag{3.1.7}$$

where we take the principal value for the complex log; namely $\log z = \log|z| + i \arg z$ with $-\pi < \arg z \leq \pi$. Since the plaquette can then be written in terms of $F_{n,\mu\nu}$ as

$$P_n = e^{ia^2 F_{n,12}} \ , \tag{3.1.8}$$

the lattice counterpart of the gauge action (3.1.1) can be defined as

$$S_g = -\frac{\beta}{2} \sum_n \left(P_n + P_n^{-1} \right) = -\beta \sum_n \cos\left(a^2 F_{n,12} \right) \ , \tag{3.1.9}$$

which approaches

$$S_g \simeq \frac{1}{4g^2} \sum_n a^2 (F_{n,\mu\nu})^2 \ , \tag{3.1.10}$$

in the continuum limit up to an irrelevant constant with the identification

$$\beta = \frac{1}{(ga)^2} \ . \tag{3.1.11}$$

In the present 2D U(1) theory, the topological charge can be defined as

$$\begin{aligned} Q_{\log} &= \frac{1}{4\pi} \sum_n a^2 \epsilon^{\mu\nu} F_{n,\mu\nu} \\ &= \frac{1}{2\pi} \sum_n a^2 F_{n,12} \\ &= -\frac{i}{2\pi} \sum_n \log P_n \ , \end{aligned} \tag{3.1.12}$$

which gives an integer value even at finite a. This can be proved easily by noting that $\prod_n P_n = 1$ since each link variable appears twice in this product with opposite directions. We call this definition (3.1.12) the "log definition". As an alternative definition, we consider

$$Q_{\sin} = -\frac{i}{4\pi} \sum_n \left(P_n - P_n^{-1} \right) = \frac{1}{2\pi} \sum_n \sin\left(a^2 F_{n,12} \right) \ , \tag{3.1.13}$$

which approaches (3.1.4) in the continuum limit recalling (3.1.8). Note, however, that the topological charge defined on the lattice in this way can take non-integer values in general

before taking the continuum limit. We call this definition (3.1.13) the "sine definition". Thus the lattice theory is given by

$$S = S_g + S_\theta \ , \tag{3.1.14}$$

where S_g is given by (3.1.9) and S_θ is given by (3.1.3) with Q defined either by (3.1.12) or by (3.1.13).

Since this theory is superrenormalizable, we can take the continuum limit $a \to 0$ with fixed g, which is set to unity throughout this work without loss of generality. In this unit, the physical volume of the 2D torus is given by

$$V_{\text{phys}} = (La)^2 = \frac{L^2}{\beta} \ , \tag{3.1.15}$$

where we have used (3.1.11).

3.2 Applying the CLM to the 2D U(1) gauge theory

3.2.1 The complex Langevin equation for the 2D U(1)

The first step of the CLM is to complexify the dynamical variables. In the present case of U(1) gauge theory, we extend the link variables $U_{n,\mu} \in \mathrm{U}(1)$ to $\mathcal{U}_{n,\mu} \in \mathbb{C} \setminus \{0\}$, which corresponds to extending the gauge field $A_\mu(x) \in \mathbb{R}$ to $\mathcal{A}_\mu(x) \in \mathbb{C}$ in the continuum theory. Then we consider a fictitious time evolution $\mathcal{U}_{n,\mu}(t)$ of the link variables governed by the complex Langevin equation

$$\mathcal{U}_{n,\mu}(t+\Delta t) = \mathcal{U}_{n,\mu}(t) \exp\left[i \Big\{ -\Delta t \, D_{n,\mu} S + \sqrt{\Delta t}\, \eta_{n,\mu}(t) \Big\} \right] \ , \tag{3.2.1}$$

where $\eta_{n,\mu}(t)$ is a real Gaussian noise normalized by $\langle \eta_{n,\mu}(s) \eta_{k,\nu}(t) \rangle = 2\delta_{n,k}\delta_{\mu,\nu}\delta_{s,t}$. The term $D_{n,\mu}S$ is the drift term defined by

$$D_{n,\mu} S = \lim_{\epsilon \to 0} \frac{S(e^{i\epsilon} U_{n,\mu}) - S(U_{n,\mu})}{\epsilon} \ , \tag{3.2.2}$$

first for the unitary link variables $U_{n,\mu}(t)$, and then it is defined for the complexified link variables $\mathcal{U}_{n,\mu}(t)$ by analytic continuation in order to respect holomorphicity. Using the action (3.1.14), we obtain $D_{n,\mu}S = D_{n,\mu}S_g + D_{n,\mu}S_\theta$, where the first term is given as

$$\begin{aligned} D_{n,1} S_g &= -i\frac{\beta}{2}(P_n - P_n^{-1} - P_{n-\hat{2}} + P_{n-\hat{2}}^{-1}) \ , \\ D_{n,2} S_g &= -i\frac{\beta}{2}(-P_n + P_n^{-1} + P_{n-\hat{1}} - P_{n-\hat{1}}^{-1}) \ . \end{aligned} \tag{3.2.3}$$

The second term $D_{n,\mu}S_\theta$ depends on the definition of the topological charge. If one uses the log definition (3.1.12), Eq. (3.2.2) for the θ term becomes a δ-function, which vanishes identically except for configurations with $P_n = -1$ for some n, reflecting the topological

nature of the definition. Such configurations are precisely the ones that appear when the topology change occurs within the configuration space of $U_{n,\mu}$. It is not straightforward to extend such a term to a holomorphic function of $\mathcal{U}_{n,\mu}$.

On the other hand, if one uses the sine definition (3.1.13), the drift term becomes

$$\begin{aligned} D_{n,1}S_\theta =& -i\frac{\theta}{4\pi}(P_n + P_n^{-1} - P_{n-\hat{2}} - P_{n-\hat{2}}^{-1}) \ , \\ D_{n,2}S_\theta =& -i\frac{\theta}{4\pi}(-P_n - P_n^{-1} + P_{n-\hat{1}} + P_{n-\hat{1}}^{-1}) \ , \end{aligned} \tag{3.2.4}$$

which may be viewed as an approximation of the δ-function mentioned above. Moreover, it can be readily extended to a holomorphic function of $\mathcal{U}_{n,\mu}$. For this reason, we use the sine definition for the non-punctured model.

The criterion [6] for the validity of the CLM states that the histogram of the drift term should fall off exponentially or faster. There are two cases in which this criterion cannot be met. The first case occurs when the configuration comes close to the poles of the drift terms (3.2.3), (3.2.4), which correspond to configurations with $P_n = 0$ for some n. If this happens during the Langevin process, there is a possibility of violating the criterion. This problem is called the singular-drift problem [68, 69], which was found first in simple models [70, 71]. In the present model, the same problem is caused also by approaching configurations with $|P_n| = \infty$ for some n, which are related to the poles by the parity transformation.

The second case occurs when the dynamical variables make large excursions in the imaginary directions [3]. This problem is called the excursion problem. In the present model, this corresponds to the situation in which the link variables have absolute values $|\mathcal{U}_{n,\mu}|$ far from unity.

Both the singular-drift problem and the excursion problem can occur because the link variables $\mathcal{U}_{n,\mu}$ are not restricted to be unitary in the CLM. In order to avoid these problems, it is important to perform the gauge cooling, which we explain in the next section.

3.2.2 Gauge cooling for the 2D U(1)

The idea of gauge cooling [45] is to reduce the non-unitarity of link variables as much as possible by making gauge transformations corresponding to the complexified Lie group after each step (3.2.1) of the Langevin process.

The deviation of the link variables from U(1) can be defined by the unitarity norm

$$\mathcal{N} = \frac{1}{2L^2}\sum_{n,\mu}\left\{\mathcal{U}_{n,\mu}^*\mathcal{U}_{n,\mu} + (\mathcal{U}_{n,\mu}^*\mathcal{U}_{n,\mu})^{-1} - 2\right\} \ . \tag{3.2.5}$$

The gauge cooling reduces this quantity by a complexified gauge transformation, which is determined as follows.

First we consider an infinitesimal gauge transformation

$$\delta \mathcal{U}_{n,\mu} = (\epsilon_n - \epsilon_{n+\hat{\mu}})\, \mathcal{U}_{n,\mu} \ , \tag{3.2.6}$$

where $\epsilon_n \in \mathbb{R}$. The change of the unitarity norm due to the transformation is given by

$$\begin{aligned} \delta \mathcal{N} &= \frac{1}{2L^2} \sum_{n,\mu} \left\{ 2(\epsilon_n - \epsilon_{n+\hat{\mu}}) \mathcal{U}^*_{n,\mu} \mathcal{U}_{n,\mu} - 2(\epsilon_n - \epsilon_{n+\hat{\mu}}) (\mathcal{U}^*_{n,\mu} \mathcal{U}_{n,\mu})^{-1} \right\} \\ &= \frac{1}{2L^2} \sum_{n} 2\epsilon_n G_n \ , \end{aligned} \tag{3.2.7}$$

where G_n is defined as

$$G_n = \sum_{\mu} \left\{ \mathcal{U}^*_{n,\mu} \mathcal{U}_{n,\mu} - \mathcal{U}^*_{n-\hat{\mu},\mu} \mathcal{U}_{n-\hat{\mu},\mu} - (\mathcal{U}^*_{n,\mu} \mathcal{U}_{n,\mu})^{-1} + (\mathcal{U}^*_{n-\hat{\mu},\mu} \mathcal{U}_{n-\hat{\mu},\mu})^{-1} \right\} . \tag{3.2.8}$$

Therefore, we find that the unitarity norm is reduced most efficiently by choosing $\epsilon_n \propto -G_n$.

Using this result, we consider a finite gauge transformation

$$\mathcal{U}_{n,\mu} \mapsto g_n \, \mathcal{U}_{n,\mu} \, g^{-1}_{n+\hat{\mu}} \ ; \qquad g_n = e^{-\alpha G_n} \ , \tag{3.2.9}$$

which makes the unitarity norm

$$\mathcal{N}(\alpha) = \frac{1}{2L^2} \sum_{n,\mu} \left\{ \mathcal{U}^*_{n,\mu} \mathcal{U}_{n,\mu} e^{-2\alpha(G_n - G_{n+\hat{\mu}})} + (\mathcal{U}^*_{n,\mu} \mathcal{U}_{n,\mu})^{-1} e^{2\alpha(G_n - G_{n+\hat{\mu}})} - 2 \right\} , \tag{3.2.10}$$

depending on α in (3.2.9). We search for an optimal α that minimizes (3.2.10). Note here that it is typically a small number since the gauge cooling is performed after each step of the Langevin process. We therefore expand Eq. (3.2.10) with respect to α up to the second order and obtain the value of α that minimizes it as

$$\alpha = \frac{1}{2} \frac{\sum_n G_n^2}{\sum_{n,\mu} [(G_n - G_{n+\hat{\mu}})^2 \{ \mathcal{U}^*_{n,\mu} \mathcal{U}_{n,\mu} + (\mathcal{U}^*_{n,\mu} \mathcal{U}_{n,\mu})^{-1} \}]} \ . \tag{3.2.11}$$

We repeat this procedure until the unitarity norm changes by a fraction less than 10^{-5}.

3.2.3 Adaptive stepsize

When we solve the complex Langevin equation in its discretized version (3.2.1), it occasionally happens that the drift term becomes extremely large, in particular during the thermalization process. This causes a large discretization error, which either makes the thermalization slow or destabilizes the simulation. We can avoid this problem by using a small stepsize Δt, but the computational cost for a fixed Langevin time increases proportionally to $(\Delta t)^{-1}$ and the calculation becomes easily unfeasible. The adaptive stepsize [66] is a useful technique, which amounts to reducing the stepsize only when the drift term becomes large.

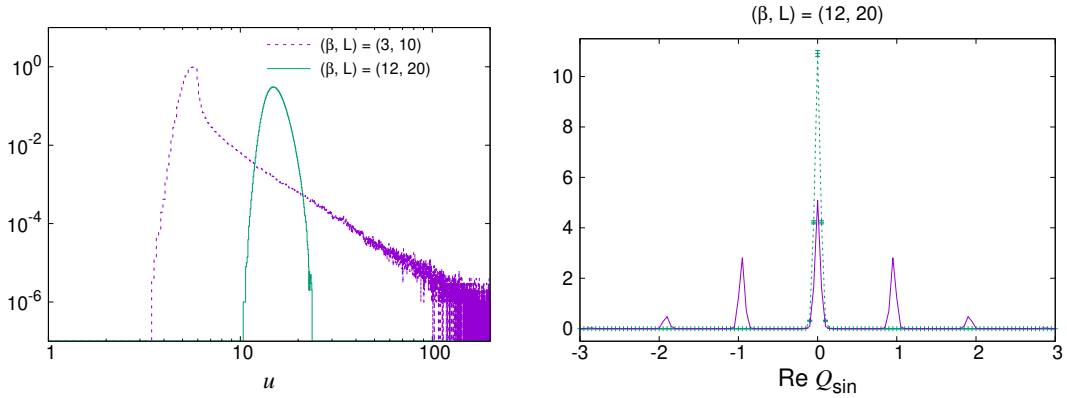

Figure 3.1: The results obtained by the CLM for the non-punctured model using the sine definition $Q_{\sin}$ of the topological charge. (Left) The histogram of the magnitude u of the drift term defined by (3.2.12) is shown for $(\beta, L) = (3, 10),\ (12, 20)$ with $\theta = \pi$. (Right) The histogram of $\mathrm{Re}\, Q_{\sin}$ is shown for $(\beta, L) = (12, 20)$ with $\theta = \pi$. The exact result obtained for $(\beta, L) = (12, 20)$ with $\theta = 0$ is shown by the solid line for comparison.

In our simulation, we measure the magnitude of the drift term defined as

$$u = \max_{n,\mu} |D_{n,\mu} S| \tag{3.2.12}$$

at each step, and choose the Langevin stepsize Δt in (3.2.1) as

$$\Delta t = \begin{cases} \Delta t_0 & \text{for } u < v_0 \ , \\ \dfrac{v_0}{u} \Delta t_0 & \text{otherwise} \ , \end{cases} \tag{3.2.13}$$

where Δt_0 is the default stepsize, and v_0 is the threshold for the magnitude of drift term. In the present work, the default stepsize is set to $\Delta t_0 = 10^{-5}$, and the threshold is set to $v_0 = 2\beta$, considering a bound $u \leq 2\beta$ for $\theta = 0$, where the CLM reduces to the real Langevin method. The measurement of the observables should be made with the same interval in terms of the Langevin time but not in terms of the number of steps.

3.2.4 Results with the naive implementation

In this section, we present our results obtained by the CLM, which is implemented naively using the non-punctured model explained above as opposed to the punctured model, which we use later. As for the definition of the topological charge, we adopt the sine definition (3.1.13) for the reason given in Section 3.2.1.

We have performed simulations at various θ for $(\beta, L) = (3, 10),\ (12, 20)$ corresponding to a fixed physical volume $V_{\mathrm{phys}} \equiv L^2/\beta = 10^2/3$. Below we show our results only for $\theta = \pi$, where the sign problem becomes severest, but the situation is the same for all values of θ.

In Fig. 3.1(Left), we show the histogram of the magnitude u of the drift term. The distribution falls off rapidly for $(\beta, L) = (12, 20)$, but it decays slowly with a power law for $(\beta, L) = (3, 10)$. Thus the criterion for correct convergence is satisfied for $(\beta, L) = (12, 20)$ but not for $(\beta, L) = (3, 10)$ due to the large drifts.

In Fig. 3.1(Right), we plot the histogram of $\mathrm{Re}\, Q_{\mathrm{sin}}$ obtained by the CLM for $(\beta, L) = (12, 20)$ with $\theta = \pi$, which has a sharp peak at $\mathrm{Re}\, Q_{\mathrm{sin}} \sim 0$. In the same figure, we also plot the exact result for $(\beta, L) = (12, 20)$ with $\theta = 0$ for comparison, which exhibits a few sharp peaks at integer values within the range $-2 \lesssim \mathrm{Re}\, Q_{\mathrm{sin}} \lesssim 2$. From these two plots, we conclude that the transitions between different topological sectors are highly suppressed in the simulation, which causes a problem with the ergodicity.

This occurs also at $\theta = 0$ for large β, and it is called the "topology freezing problem" in the literature. In fact, the results one obtains by simulations suffering from this problem correspond to the expectation values restricted to the topological sector specified by the initial configuration. This is true for both $\theta = 0$ and $\theta \neq 0$. In this case, however, the effect of the θ term cancels between the numerator and the denominator of the expectation values, and the calculation essentially reduces to that of the real Langevin method at $\theta = 0$.

For $(\beta, L) = (3, 10)$ with $\theta = \pi$, on the other hand, the histogram of $\mathrm{Re}\, Q_{\mathrm{sin}}$ obtained by the CLM has broad peaks that overlap with each other, which looks similar to the exact result for $(\beta, L) = (3, 10)$ with $\theta = 0$. This implies that the topology freezing problem does not occur for $(\beta, L) = (3, 10)$. See also Fig. 3.3.

Below we define the observables we investigate. First, we define the average plaquette by

$$w = \frac{1}{V} \frac{\partial}{\partial \beta} \log Z \ . \tag{3.2.14}$$

Hereafter, V denotes the number of plaquettes in the action, which is $V = L^2$ for the non-punctured model and $V = L^2 - 1$ for the punctured model we define in Section 3.3.1. The topological charge density is defined by

$$\frac{1}{V} \langle Q \rangle = -i \frac{1}{V} \frac{\partial}{\partial \theta} \log Z \ , \tag{3.2.15}$$

which is zero at $\theta = 0$ and purely imaginary for $\theta \neq 0$. Finally, the topological susceptibility is defined by

$$\chi = \frac{1}{V} \left(\langle Q^2 \rangle - \langle Q \rangle^2 \right) = -\frac{1}{V} \frac{\partial^2}{\partial \theta^2} \log Z \ , \tag{3.2.16}$$

which is real for all θ. In fact, the topological susceptibility χ is related to the topological charge density (3.2.15) through

$$\chi = -i \frac{1}{V} \frac{\partial}{\partial \theta} \langle Q \rangle \ . \tag{3.2.17}$$

Note, however, that this relation can be violated if the CLM fails to calculate the expectation values correctly.

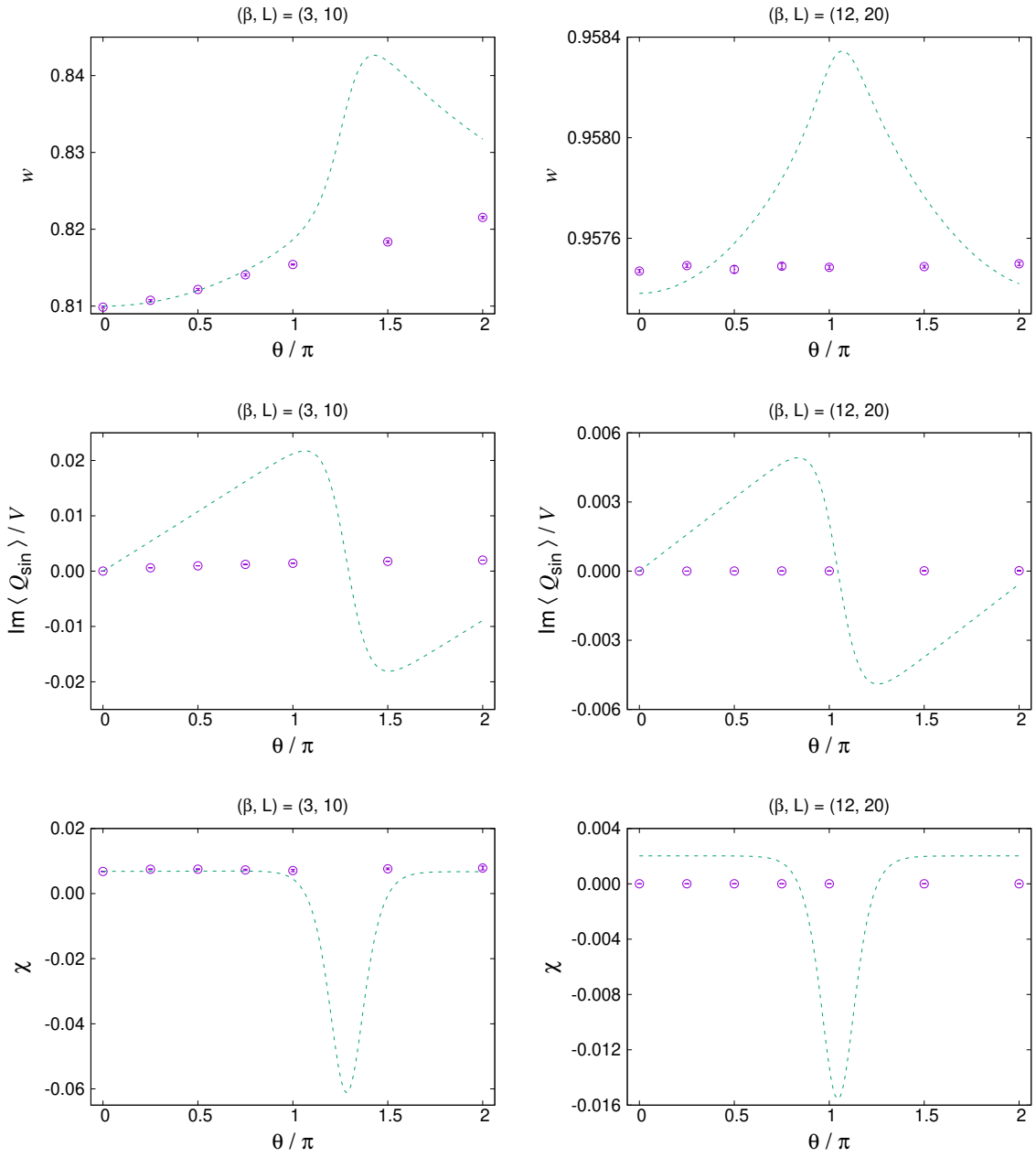

Figure 3.2: The results for various observables obtained by the CLM for the non-punctured model with the sine definition $Q_{\sin}$. The average plaquette (Top), the imaginary part of the topological charge density (Middle), the topological susceptibility (Bottom) are plotted against θ for $(\beta, L) = (3, 10)$ (Left) and $(12, 20)$ (Right). The exact results for the same (β, L) are shown by the dashed lines for comparison.

In Fig. 3.2, we show the results obtained by the CLM for the non-punctured model. We also plot the exact results for comparison, which are derived in Appendix A.4. In the left column, we present our results for $(\beta, L) = (3, 10)$, which suffer from the incorrect convergence, whereas in the right column, we present our results for $(\beta, L) = (12, 20)$, which suffer from the topology freezing problem. In either case, our results do not reproduce the exact results as anticipated. Note that our results at $\theta = 0$ agree with the exact results for $(\beta, L) = (3, 10)$ but not for $(\beta, L) = (12, 20)$. This is because the topology freezing problem occurs for large β even at $\theta = 0$, where the sign problem is absent.

Thus we find that the CLM with the naive implementation fails for both $(\beta, L) = (3, 10)$ and $(\beta, L) = (12, 20)$ for different reasons. For $(\beta, L) = (3, 10)$, the topology change occurs but the criterion for correct convergence is not satisfied due to the large drifts. For $(\beta, L) = (12, 20)$, the criterion for correct convergence is satisfied, but the ergodicity is violated due to the topology freezing problem. We have searched for a parameter region in which neither of the problems occur, but we could not find one. In fact, we will see in the next section that these problems are related to each other at least in the present model.

3.2.5 The appearance of large drifts and the topology change

In this section, we provide more in-depth discussions on the relationship between the appearance of large drifts and the topology change in the non-punctured model. Let us first recall that the drift terms are given by (3.2.3) and (3.2.4), which depend on P_n. When β is large, the gauge action S_g favors configurations with $P_n \sim 1$ for all n, which implies that the drift terms are small.

On the other hand, the notion of topological sectors can be defined by the real part of (3.1.12), which takes integer values, even for complexified configurations that are generated in the CLM. In order for a transition between different topological sectors to occur, one of the plaquettes has to cross the branch cut; namely the phase of the plaquette has to jump from $-\pi$ to π or vice versa. When this occurs, large drift terms can appear as can be seen from Fig. 3.3, where we plot the histories of $\mathrm{Re}\, Q_{\log}$ and the magnitude of the drift term (3.2.12). We observe clear correlation between the large drift term and the topology change. We have also confirmed that the large drift term appears for the link variables composing the plaquette that crosses the branch cut.

In order to understand this observation better, we focus on a particular link variable $\mathcal{U}_{k,1}$, and consider the corresponding drift term, which depends on the plaquettes P_k and $P_{k-\hat{2}}$ sharing the link. For simplicity, we set $P_{k-\hat{2}} = 1$ and consider the drift term v as a function of P_k

$$v = \beta \sin\phi - i\frac{\theta}{2\pi}\left(\cos\phi - 1\right) \ , \tag{3.2.18}$$

where we have defined a complex parameter ϕ by $\phi = -i \log P_k$. A large drift appears

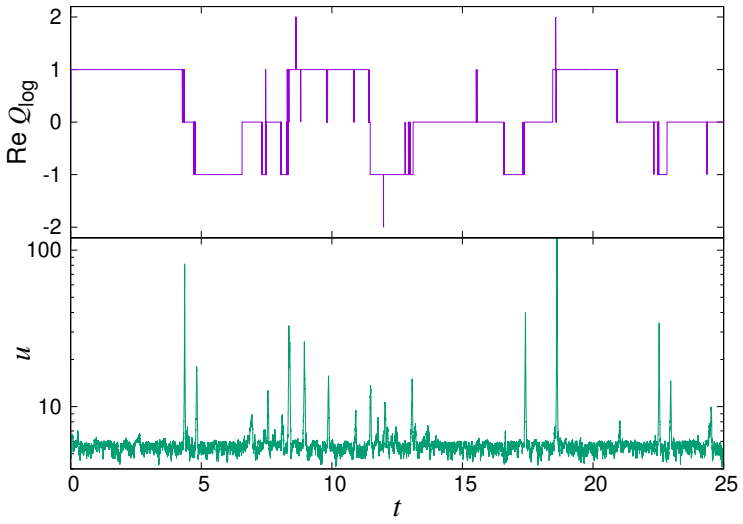

Figure 3.3: The results obtained by the CLM for the non-punctured model with the sine definition $Q_{\sin}$ for $(\beta, L) = (3, 10)$ with $\theta = \pi$. The upper plot shows the history of the topological charge $Q_{\log}$ with the log definition, whereas the lower plot shows the history of the magnitude u of the drift term in the log scale.

when $|\mathrm{Im}\,\phi| \to \infty$. In Fig. 3.4(Left), we plot the drift term as a flow diagram for $\beta = \theta = 1$. Considering that the contribution of the drift term v to the change of ϕ at a Langevin step is given by $\Delta\phi = -v\Delta t$, we actually plot $(-v)$ in the complex ϕ plane.

In what follows we assume that $\beta > \theta/2\pi$. Then we find from Eq. (3.2.18) that there are two fixed points corresponding to $v = 0$. One is $\phi = 0$ and the other is $\phi = i\log[(\theta/2\pi + \beta)/(\theta/2\pi - \beta)]$, which is close to $\pm\pi$ for $\beta \gg \theta/2\pi$. As one can see from Fig. 3.4(Left), the fixed point $\phi = 0$ is attractive, which confirms that P_k tends to become unity when β is large. The other fixed point $\phi \sim \pm\pi$ is repulsive, and the magnitude $|v|$ grows exponentially as one flows away in the imaginary direction; See Fig.3.4(Right). As we mentioned above, when the transition between topological sectors occurs, one of the plaquettes crosses the branch cut, which corresponds to $\mathrm{Re}\,\phi = \pm\pi$ in the flow diagram. When this happens, the configuration can flow in the imaginary direction, which causes a large drift.

3.3 Introducing a puncture on the 2D torus

Since the problem we encounter in the previous section occurs due to the topological nature of the θ term, a simple remedy would be to change the topology of the base manifold to a noncompact one. Here we consider introducing a puncture on the 2D torus. Once we introduce a puncture, the drift term $D_{n,\mu}S_\theta$ with the log definition of the topological charge has nonzero contributions for the link variables surrounding the puncture, which enable us to include the effect of the θ term correctly in the CLM as

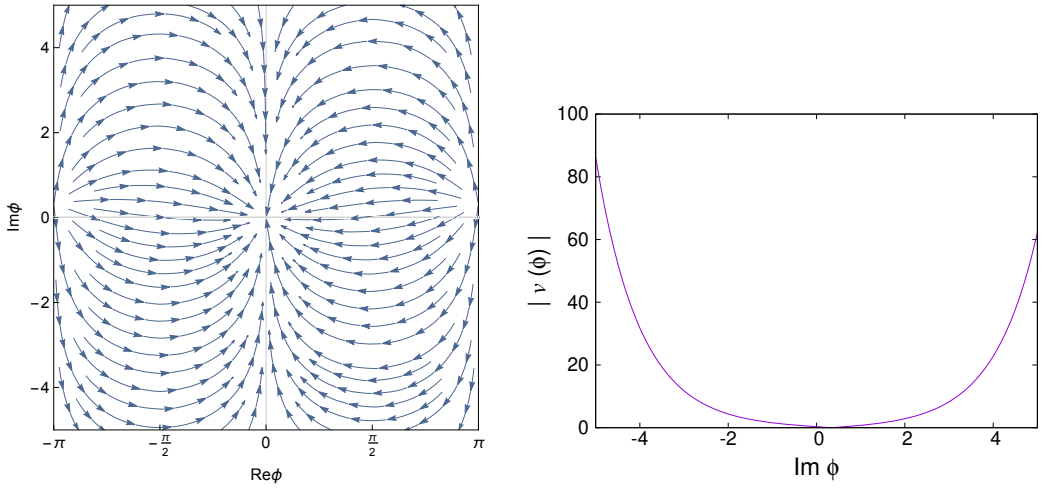

Figure 3.4: (Left) A flow diagram representing $-v$ defined by (3.2.18) is shown as a function of ϕ for $\beta = \theta = 1$. (Right) The absolute value $|v(\phi)|$ is plotted against $\mathrm{Im}\,\phi$ for $\mathrm{Re}\,\phi = \pi$.

we will see in Section 3.4. Therefore, for the rest of this study, we basically use the log definition to simplify our discussions. Unlike the non-punctured model, the topological charge is no more restricted to integer values, and it can be changed freely.

Since the puncture affects the theory only locally, its effect is expected to die out in the infinite volume limit for $|\theta| < \pi$ as we demonstrate explicitly in this section using the exact results. Thus unless we are interested in a theory with a finite volume, the punctured model is as good as the original model, the difference simply being a different choice of "boundary conditions". In fact, we will see that the non-punctured model has slow convergence to the infinite volume limit for $\theta \sim \pi$, which is not the case in the punctured model.

3.3.1 Defining the punctured model on the lattice

There are various ways to introduce a puncture on the periodic lattice. Here we consider removing a plaquette as a simple choice. More precisely, we define the punctured model by removing one plaquette, let say P_K, from the sum appearing in the gauge action (3.1.9) and the topological charge (3.1.12) when we define the action (3.1.14).

As an alternative method, we have also tried introducing a slit at a particular link, which amounts to duplicating the corresponding link variable and including each of them in the plaquettes that share the link. The results turn out to be qualitatively the same as the ones obtained by removing a plaquette. There are, of course, many others, but in any case, one can obtain exact results for a finite lattice as we explain in Appendix A, and using them, one can demonstrate explicitly that the punctured model is equivalent to the original non-punctured model in the infinite volume limit for $|\theta| < \pi$.

3.3.2 Equivalence in the infinite volume limit

In this section, we show the equivalence of the non-punctured model and the punctured model in the infinite volume limit. Here we use the log definition of the topological charge, but a similar statement holds as far as the same definition is used for the two models.[1]

The partition function for the non-punctured model is given by (See Appendix A.2 for derivation.)

$$Z_{\text{nonpunc}} = \sum_{n=-\infty}^{+\infty} \left[\mathcal{I}(n,\theta,\beta)\right]^V \tag{3.3.1}$$

for finite $V = L^2$, where the function $\mathcal{I}(n,\theta,\beta)$ is defined by

$$\mathcal{I}(n,\theta,\beta) = \frac{1}{2\pi}\int_{-\pi}^{\pi} d\phi\, e^{\beta\cos\phi + i\left(\frac{\theta}{2\pi}-n\right)\phi} \ . \tag{3.3.2}$$

Let us take the infinite volume limit $V \to \infty$, in which the sum over n in (3.3.1) is dominated by the term that gives the largest absolute value $|\mathcal{I}(n,\theta,\beta)|$. This corresponds to the n that minimizes $|\frac{\theta}{2\pi} - n|$. Thus in the infinite volume limit, the free energy is obtained as

$$\lim_{V\to\infty} \frac{1}{V}\log Z_{\text{nonpunc}} = \log \mathcal{I}(0,\tilde{\theta},\beta) \ , \tag{3.3.3}$$

where $\tilde{\theta}$ is defined by $\tilde{\theta} = \theta - 2\pi k$ with the integer k chosen so that $-\pi < \tilde{\theta} \le \pi$.

On the other hand, the partition function for the punctured model is given by (See Appendix A.3 for derivation.)

$$Z_{\text{punc}} = \left[\mathcal{I}\left(0,\theta,\beta\right)\right]^V \tag{3.3.4}$$

for finite $V = L^2 - 1$, which implies that the free energy

$$\frac{1}{V}\log Z_{\text{punc}} = \log\left[\mathcal{I}\left(0,\theta,\beta\right)\right] \tag{3.3.5}$$

is actually V independent. Hence all the observables that can be derived from it has no finite size effects. Note also that this model does not have the 2π periodicity in θ. By comparing (3.3.3) and (3.3.5), one can see that the two models are equivalent in the infinite volume limit for $|\theta| < \pi$.

The observables defined in Section 3.2.4 can be calculated for the two models using (3.3.1) and (3.3.4) by numerical integration (See Appendix A.4 for the details.). In Fig. 3.5, we plot the average plaquette (Top) defined by (3.2.14), the imaginary part of the topological charge density (Middle) defined by (3.2.15) and the topological susceptibility (Bottom) defined by (3.2.16) for $L = 10$ (Left) and $L = 20$ (Right), respectively, with the same $\beta = 12$. The results for the two models tend to agree as L increases for $|\theta| < \pi$.

[1] In the case of the sine definition, the equivalence of the two models in the infinite volume limit holds for $|\theta| < \theta_{\text{c}}(\beta)$, where $\theta_{\text{c}}(\beta) \sim \pi\{1 + 1/(2\beta)\}$ for large β.

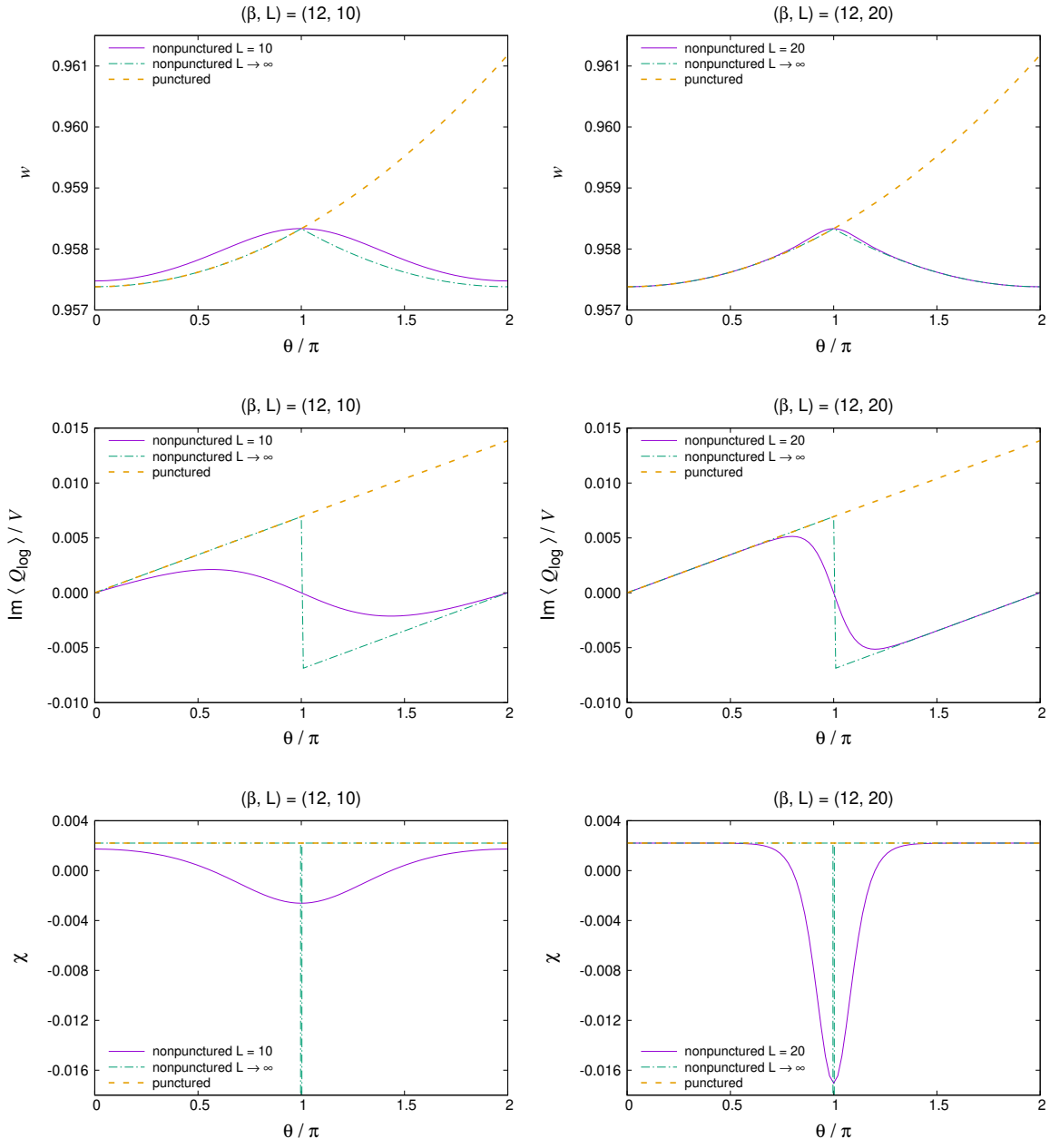

Figure 3.5: The exact results for various observables obtained by using the log definition $Q_{\log}$ of the topological charge. The average plaquette (Top), the imaginary part of the topological charge density (Middle), the topological susceptibility (Bottom) obtained for the non-punctured (solid line) and punctured (dashed line) models are plotted against θ for $L = 10$ (Left) and $L = 20$ (Right) with the same $\beta = 12$. Note that the results for the punctured model are actually independent of L. For the non-punctured model, we also plot the results in the infinite volume limit $L \to \infty$ with $\beta = 12$ by the dash-dotted lines for comparison.

We can evaluate the free energy (3.3.5) for the punctured model more explicitly for large β, which is relevant in the continuum limit. By integrating over ϕ in Eq. (3.3.2) as

$$\mathcal{I}(n,\theta,\beta) \simeq \frac{1}{\sqrt{2\pi\beta}} e^{\beta - \frac{1}{2\beta}\left(\frac{\theta}{2\pi} - n\right)^2} , \tag{3.3.6}$$

we get

$$\frac{1}{V}\log Z_{\text{punc}} \simeq \beta - \frac{1}{2}\log 2\pi\beta - \frac{\theta^2}{8\pi^2\beta} . \tag{3.3.7}$$

From this, we can obtain various observables for the punctured model as

$$w \simeq 1 - \frac{1}{2\beta} + \frac{\theta^2}{8\pi^2\beta^2} , \tag{3.3.8}$$

$$\frac{\langle Q \rangle}{V} \simeq \frac{i\theta}{4\pi^2\beta} , \tag{3.3.9}$$

$$\chi \simeq \frac{1}{4\pi^2\beta} \tag{3.3.10}$$

for finite V, which explains the θ dependence observed in Fig. 3.5.

From Fig. 3.5, we also find that the results for the non-punctured model have sizable finite volume effects, in particular around $\theta \sim \pi$, which is absent in the punctured model. While the volume independence of the punctured model may well be peculiar to the present 2D gauge theory case, the advantage of the punctured model compared with the non-punctured model from the viewpoint of finite volume effects may hold more generally.

3.4 Application of the CLM to the punctured model

In this section, we apply the CLM to the punctured model using the log definition $Q_{\log}$ of the topological charge. Our results reproduce the exact results discussed in the previous section as long as we are close enough to the continuum limit. We also show that the topology freezing problem is circumvented without causing large drifts thanks to the puncture.

3.4.1 The drift terms for the punctured model

We have discussed the drift terms in the non-punctured model in Section 3.2.1. For the punctured model, we only have to modify the drift terms for the four link variables surrounding the puncture; i.e., $\mathcal{U}_{K,1}$, $\mathcal{U}_{K+\hat{2},1}$, $\mathcal{U}_{K,2}$ and $\mathcal{U}_{K+\hat{1},2}$. Thus we obtain

$$D_{n,1}S = \begin{cases} -i\frac{\beta}{2}(P_n - P_n^{-1} - P_{n-\hat{2}} + P_{n-\hat{2}}^{-1}) & \text{for } n \neq K,\ K+\hat{2} , \\ -i\frac{\beta}{2}(-P_{K-\hat{2}} + P_{K-\hat{2}}^{-1}) + i\frac{\theta}{2\pi} & \text{for } n = K , \\ -i\frac{\beta}{2}(P_{K+\hat{2}} - P_{K+\hat{2}}^{-1}) - i\frac{\theta}{2\pi} & \text{for } n = K+\hat{2} , \end{cases} \tag{3.4.1}$$

$$D_{n,2}S = \begin{cases} -i\frac{\beta}{2}(-P_n + P_n^{-1} + P_{n-\hat{1}} - P_{n-\hat{1}}^{-1}) & \text{for } n \neq K,\ K+\hat{1} , \\ -i\frac{\beta}{2}(P_{K-\hat{1}} - P_{K-\hat{1}}^{-1}) - i\frac{\theta}{2\pi} & \text{for } n = K , \\ -i\frac{\beta}{2}(-P_{K+\hat{1}} + P_{K+\hat{1}}^{-1}) + i\frac{\theta}{2\pi} & \text{for } n = K+\hat{1} , \end{cases} \tag{3.4.2}$$

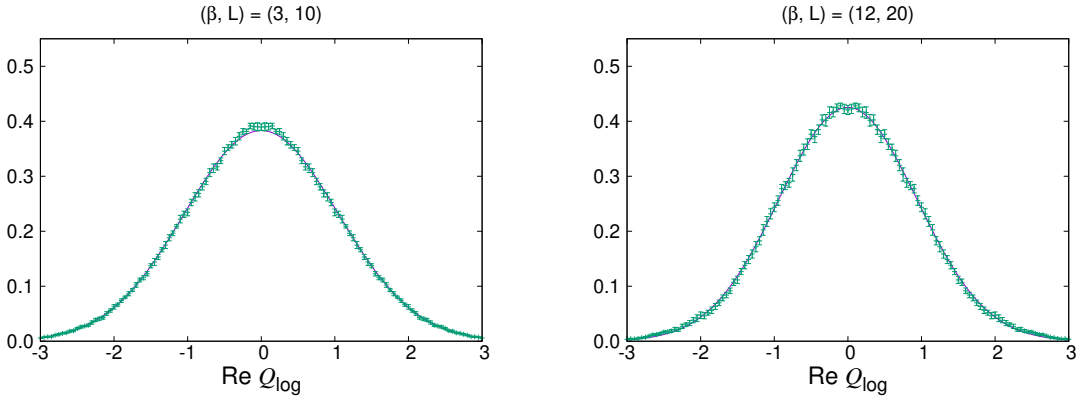

Figure 3.6: The topological charge distribution for $\theta = 0$ obtained by the CLM for the punctured model using the log definition $Q_{\log}$ is plotted for $(\beta, L) = (3, 10)$ (Left) and $(\beta, L) = (12, 20)$ (Right). The solid lines represent the exact results obtained by evaluating (3.4.4) using the partition function (3.3.4).

where we have ignored the issue of δ-function discussed in Section 3.2.1. This is justified if all the plaquettes in the action never cross the branch cut; i.e., $|\mathrm{Im} \log P_n| \leq \pi - \epsilon$ for $\forall n \neq K$ with a strictly positive ϵ during the Langevin simulation. We will see that this assumption is justified at sufficiently large β in Section 3.4.3.

Note that the drift term from the θ term appears only for the link variables surrounding the puncture, and it is actually a constant independent of the configuration. While these properties are peculiar to the log definition $Q_{\log}$, similar properties hold also for the sine definition $Q_{\sin}$ at large β, where all the plaquettes P_n approach unity except for P_K, which corresponds to the puncture. We discuss the case with the sine definition in Appendix B, where we see that the obtained results are qualitatively the same as those obtained with the log definition.

3.4.2 The θ dependence of the partition function

As we have seen in Section 3.3.2, the punctured model is equivalent to the non-punctured model in the infinite volume limit for $|\theta| < \pi$, beyond which the equivalence ceases to hold. In particular, the punctured model does not have the 2π periodicity in θ, which exists in the non-punctured model.

In order to understand this point better, we discuss the θ dependence of the partition function in this section. Let us first note that the partition function for arbitrary θ is related to the topological charge distribution $\rho(q)$ for $\theta = 0$ through Fourier transformation

as

$$\begin{aligned} Z(\theta) &= \int dU e^{-S_g[U]+i\theta Q[U]} \\ &= \int dU e^{-S_g[U]} \int dq\, e^{i\theta q} \delta(Q[U]-q) \\ &= Z(0) \int dq\, e^{i\theta q} \rho(q) \ . \end{aligned} \tag{3.4.3}$$

Therefore, the absence of the 2π periodicity in θ in the punctured model is directly related to its property that the topological charge can take non-integer values even if we use the log definition $Q_{\log}$. Going beyond the fundamental region $-\pi < \theta \leq \pi$ simply amounts to probing the fine structure of the topological charge distribution $\rho(q)$, which is irrelevant in the infinite volume limit.

By making an inverse Fourier transform, we can obtain the topological charge distribution $\rho(q)$ for $\theta = 0$ as

$$\rho(q) = \frac{1}{Z(0)} \int_{-\infty}^{\infty} \frac{d\theta}{2\pi} Z(\theta)\, e^{-i\theta q} \ . \tag{3.4.4}$$

We calculate this quantity for the punctured model by the CLM for $\theta = 0$. In Fig. 3.6, we show the results for $(\beta, L) = (3, 10)$ (Left) and $(\beta, L) = (12, 20)$ (Right), which agree well with the exact results obtained by evaluating (3.4.4) using the partition function (3.3.4). Note that the calculation actually reduces to that of the real Langevin method due to the absence of the sign problem for $\theta = 0$. We therefore have no concerns about the criterion for correct convergence here.

While the sign problem is absent for $\theta = 0$, the topology freezing problem can still be an issue for large β. The agreement we see for $(\beta, L) = (12, 20)$ confirms that this problem is resolved in the punctured model at least for $\theta = 0$.

3.4.3 Validity of the CLM

In this section, we discuss the validity of the CLM for the punctured model. Fig. 3.7(Left) shows the histogram of the drift term for $(\beta, L) = (3, 10)$ and $(\beta, L) = (12, 20)$ with $\theta = \pi$, which are the parameters used in Section 3.2.4 for the non-punctured model. We find that the criterion is satisfied for $(\beta, L) = (12, 20)$ but not for $(\beta, L) = (3, 10)$, similarly to the situation in the non-punctured model. The difference from the non-punctured model is seen, however, in Fig. 3.7(Right), where we show the histogram of $\mathrm{Re}\, Q_{\log}$ obtained by the CLM for $(\beta, L) = (12, 20)$ with $\theta = \pi$. (The result for $(\beta, L) = (3, 10)$ looks quite similar to this plot.) It is widely distributed within the range $-3 \lesssim \mathrm{Re}\, Q_{\log} \lesssim 3$, which is in sharp contrast to the plot in Fig. 3.1(Right) for the same $(\beta, L) = (12, 20)$ in the case of the non-punctured model. In fact, it turns out to be close[2] to the exact result obtained

[2]Note, however, that precise agreement is not expected here since the histogram of $\mathrm{Re}\, Q_{\log}$ is a non-holomorphic quantity, for which the CLM does not allow a clear interpretation.

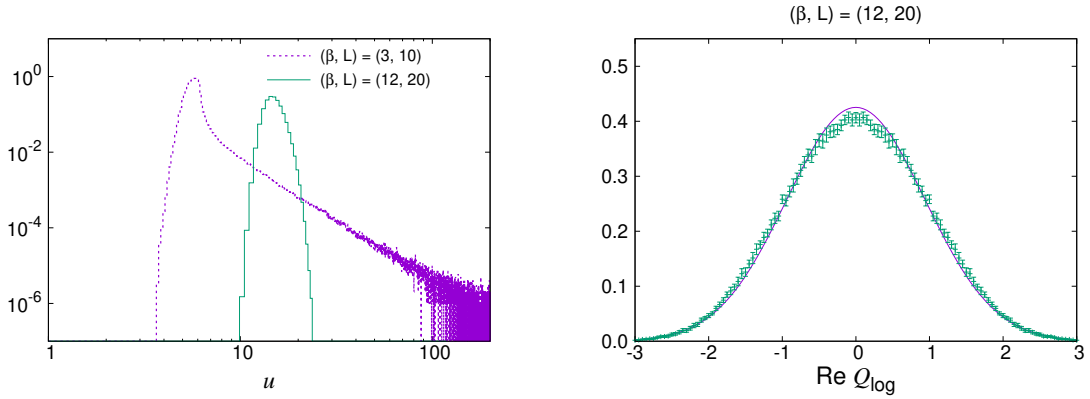

Figure 3.7: The results obtained by the CLM for the punctured model using the log definition $Q_{\log}$ of the topological charge. (Left) The histogram of the magnitude u of the drift term defined by (3.2.12) is shown for $(\beta, L) = (3, 10)$ and $(12, 20)$ with $\theta = \pi$. (Right) The histogram of $\mathrm{Re}\, Q_{\log}$ is shown for $(\beta, L) = (12, 20)$ with $\theta = \pi$. The exact result obtained for $(\beta, L) = (12, 20)$ with $\theta = 0$ is shown by the solid line for comparison.

for the same $(\beta, L) = (12, 20)$ with $\theta = 0$, which is plotted in the same figure. Thus we find that the topology freezing problem at large β is circumvented in the punctured model and yet the CLM remains valid.

Next we discuss the reason why the punctured model can avoid the topology freezing problem without causing large drifts. The difference from the non-punctured model is that one of the plaquettes, P_K, is removed from the action. Note that the topological charge $Q_{\log}$ for the punctured model is given by

$$Q_{\log} = -\frac{i}{2\pi} \sum_n \log P_n + \frac{i}{2\pi} \log P_K \ , \tag{3.4.5}$$

where the first term is nothing but the topological charge defined for the non-punctured model, whose real part takes integer values. The second term has a real part which lies within the interval $[-\frac{1}{2}, \frac{1}{2})$. Therefore it makes sense to define the "topology change" in the punctured model as the situation in which the real part of the first term changes by ± 1. As we discussed in Section 3.2.5 for the non-punctured model, one of the plaquettes should inevitably cross the branch cut in order for the topology change to occur in the above sense. When β is large, this process is highly suppressed for all the plaquettes that are included in the action. In the non-punctured model, the topology freezing problem occurs precisely for this reason. However, in the punctured model, the particular plaquette P_K is removed from the action, and therefore it can change freely even for large β.

This is demonstrated in Fig. 3.8, where we plot the probability distribution of the phase of the plaquette P_K as well as that of the other plaquettes P_n $(n \neq K)$ for $(\beta, L) = (3, 10)$ (Left) and $(\beta, L) = (12, 20)$ (Right). We find that the phase of the removed plaquette P_K is almost uniformly distributed for both (β, L). On the other hand, the distribution

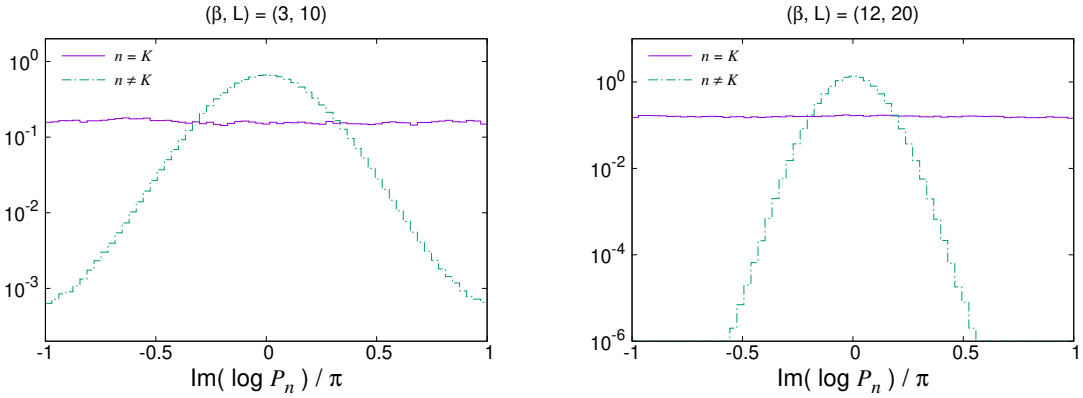

Figure 3.8: The distribution of the phase of the plaquettes is plotted for the punctured model with the log definition (3.1.12) of the topological charge for $(\beta, L) = (3, 10)$ (Left) and $(\beta, L) = (12, 20)$ (Right) with $\theta = \pi$. We show the results for the plaquette $(n = K)$ removed from the action and those for all the other plaquettes $(n \neq K)$ separately.

of the phase of the other plaquettes depends on (β, L). It has a compact support for $(\beta, L) = (12, 20)$ but not for $(\beta, L) = (3, 10)$. In the former case, there is no distribution at the branch cut, which implies that the branch cut crossing of the plaquettes P_n $(n \neq K)$ does not occur at all. In the latter case, there is a small but finite distribution at the branch cut, which means that the value of β is not large enough to suppress the branch cut crossing of the plaquettes P_n $(n \neq K)$ completely.

This is consistent with the fact that the histogram of the drift term has fast fall-off for $(\beta, L) = (12, 20)$ but not for $(\beta, L) = (3, 10)$ considering the discussion given in Section 3.2.5. While the flow diagram in Fig. 3.4(Left) is obtained for the sine definition of the topological charge, it looks similar for the log definition, which simply corresponds to setting $\theta = 0$ in (3.2.18). Therefore, large drifts can appear when one of the plaquettes P_n $(n \neq K)$ crosses the branch cut, which indeed occurs for $(\beta, L) = (3, 10)$ also for the punctured model. For $(\beta, L) = (12, 20)$, on the other hand, the topology change is made possible by allowing the removed plaquette P_K to cross the branch cut freely, but all the plaquettes that are included in the action are forced to stay close to unity because of large β. This justifies our assumption that the issue of δ-function can be neglected in deriving the drift terms (3.4.1) and (3.4.2). Since the plaquette P_K does not appear in the drift terms, it does not cause large drifts even if it crosses the branch cut. This makes it possible for the punctured model to avoid the topology freezing problem without causing large drifts.

Let us next discuss how the unitarity norm (3.2.5) behaves in our complex Langevin simulations. As we can see from (3.4.1) and (3.4.2), the link variables surrounding the puncture have a drift term in the imaginary direction coming from the θ term. At each Langevin step, two of the link variables are multiplied by $e^{\theta\Delta t/2\pi}$ and the other two are multiplied by $e^{-\theta\Delta t/2\pi}$ so that the removed plaquette is multiplied by $e^{2\theta\Delta t/\pi}$ due

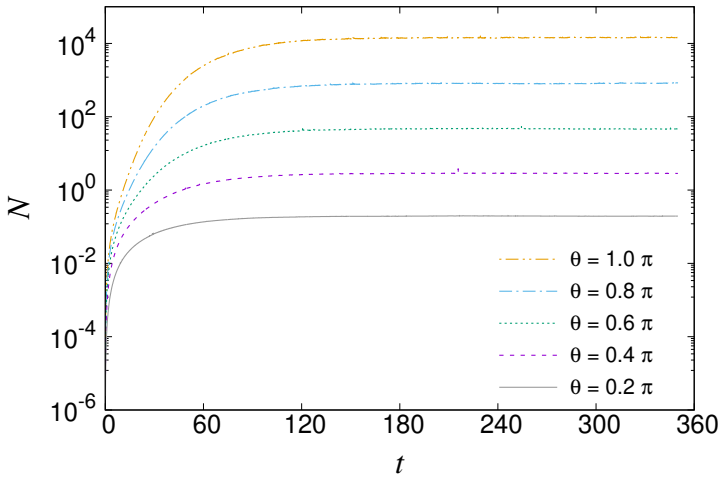

Figure 3.9: The history of the unitarity norm $\mathcal{N}$ is plotted for the punctured model with the log definition (3.1.12) of the topological charge for various θ with $(\beta, L) = (5, 16)$.

to this drift term. Therefore, there is a danger that the magnitude of these four link variables increases or decreases exponentially and hence the unitarity norm (3.2.5) grows exponentially with the Langevin time.

In Fig. 3.9, we plot the history of the unitarity norm (3.2.5) for various θ with $(\beta, L) = (5, 16)$. Similar results are obtained for other (β, L). (Here and for the rest of this subsection, we restrict ourselves to the parameter sets, for which the histogram of the drift term has fast fall-off.) Indeed we observe an exponential growth at early stage, but the unitarity norm actually saturates to a constant depending on θ at sufficiently long Langevin time. This saturation occurs since the non-unitarity of the four link variables surrounding the puncture propagates to all the other link variables on the lattice due to the interaction caused by the gauge action S_g, which tries to make each plaquette except the removed one close to unity. We find that thermalization of various observables can be achieved only after the saturation of the unitarity norm.

In fact, we find that the unitarity norm is not distributed uniformly on the lattice due to the existence of the puncture, as is also expected from the above discussion. In order to see this, we define the "local unitarity norm" by

$$\mathcal{N}(n) = \frac{1}{4} \sum_{(k,\mu)\in P_n} \left\{ \mathcal{U}^*_{k,\mu}\mathcal{U}_{k,\mu} + (\mathcal{U}^*_{k,\mu}\mathcal{U}_{k,\mu})^{-1} - 2 \right\} , \tag{3.4.6}$$

which is an average of the unitarity norm for the four link variables surrounding each plaquette P_n. The unitarity norm defined by (3.2.5) is simply an average of $\mathcal{N}(n)$ over all the plaquettes including the removed one; namely $\mathcal{N} = \frac{1}{L^2}\sum_n \mathcal{N}(n)$. In Fig. 3.10(Left), we plot this quantity $\mathcal{N}(n)$ against $n = (n_1, n_2)$ for $(\beta, L) = (12, 20)$ with $\theta = \pi$, where the puncture is located at $n = K = (10, 10)$. We observe a sharp peak at the puncture,

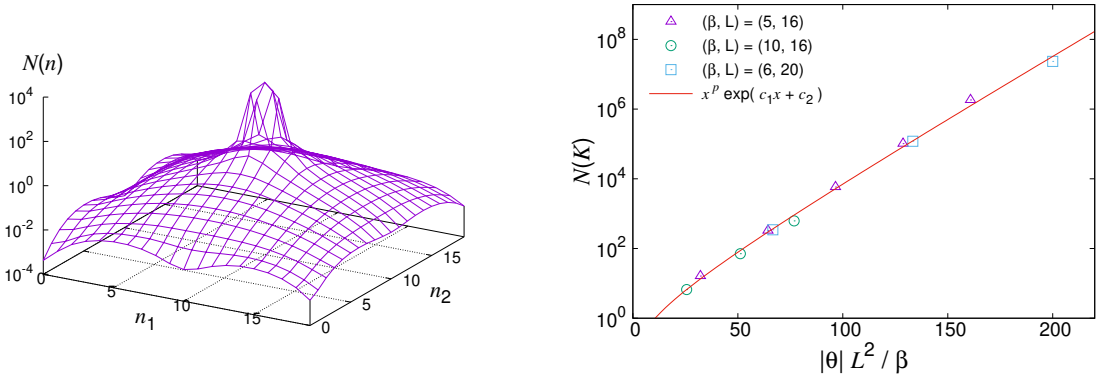

Figure 3.10: (Left) The local unitarity norm $\mathcal{N}(n)$ for each plaquette P_n defined by (3.4.6) is plotted against $n = (n_1, n_2)$ for the punctured model with the log definition (3.1.12) of the topological charge for $(\beta, L) = (12, 20)$ with $\theta = \pi$. The removed plaquette corresponds to $n = K = (10, 10)$ in this figure. (Right) The local unitarity norm $\mathcal{N}(K)$ for the removed plaquette P_K obtained for various β, L and θ is plotted against $x = |\theta|L^2/\beta$. The solid line represents a fit to $x^p \exp(c_1 x + c_2)$ with $c_1 = 0.079(5)$, $c_2 = -3(1)$ and $p = 0.8(4)$.

which goes up to $\mathcal{N}(K) \sim 6 \times 10^3$. The plaquettes adjacent to the puncture have a local unitarity norm $\sim 1.5 \times 10^3$. This implies that the unitarity norm is mostly dominated by the four link variables surrounding the puncture.

The local unitarity norm $\mathcal{N}(K)$ at the puncture depends not only on θ but also on β and L. In Fig. 3.10(Right), we plot this value against $x = |\theta|V_{\text{phys}} = |\theta|L^2/\beta$ for various θ, β and L. All the data can be fitted to a single curve $\mathcal{N}(K) = x^p \exp(c_1 x + c_2)$, which reveals an exponential behavior at large x.

What actually matters for the validity of the CLM is not so much the local unitarity norm $\mathcal{N}(n)$ as the absolute value of each plaquette P_n, which we plot in Fig. 3.11 against $n = (n_1, n_2)$ for the same parameters as in Fig. 3.10(Left). The absolute value of P_K corresponding to the removed plaquette is close to $(\sqrt{\mathcal{N}(K)})^4 \sim 3.6 \times 10^7$, which implies that $|\mathcal{U}_{K,1}|$, $|\mathcal{U}_{K+\hat{1},2}|$, $|\mathcal{U}^{-1}_{K+\hat{2},1}|$ and $|\mathcal{U}^{-1}_{K,2}|$ are close to $\sqrt{\mathcal{N}(K)}$. Except for this removed plaquette, the absolute value of the plaquette deviates only slightly from unity due to large β.

In fact, this deviation of $|P_n|$ from unity for $n \neq K$ has a physical meaning since $\text{Im}\,\langle Q_{\log}\rangle = -\frac{1}{2\pi}\sum_{n\neq K}\langle \log|P_n|\rangle$ as one can see from (3.4.5). From the exact result (3.3.9) obtained at large β, we find that $|P_n| \sim e^{-\theta/(2\pi\beta)}$ for $n \neq K$, which is ~ 0.96 for $\theta = \pi$ and $\beta = 12$ in agreement with the value observed in Fig. 3.11. If we flip the sign of θ, which corresponds to the parity transformation, we find that $|P_n| \mapsto |P_n|^{-1}$ for all n.

Note also that P_K does not appear in the drift term, which implies that its absolute value can become large without causing large drifts. We have confirmed that the criterion for correct convergence is satisfied for sufficiently large β, and indeed the exact results

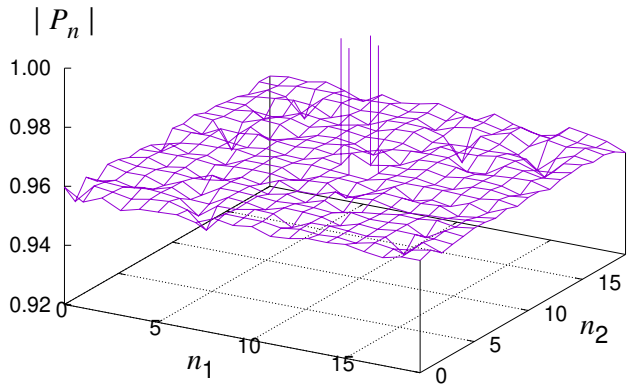

Figure 3.11: The absolute value of the plaquette P_n is plotted against $n = (n_1, n_2)$ for the punctured model with the log definition (3.1.12) of the topological charge for $(\beta, L) = (12, 20)$ with $\theta = \pi$. The removed plaquette corresponds to $n = K = (10, 10)$ in this figure.

for various observables can be reproduced correctly as we will see in the next section. This remains to be the case even for large θ and/or large $V_{\rm phys}$, where the unitarity norm becomes large.[3] Thus the present model provides a counterexample to the common wisdom that the CLM fails when the unitarity norm becomes large.

3.4.4 Results for the observables

In this section, we calculate the observables for the punctured model by the CLM and compare our results with the exact results derived in Appendix A.4. Let us recall that, in the definitions (3.2.14), (3.2.15) and (3.2.16), V denotes the number of plaquettes in the action, which is $V = L^2 - 1$ for the punctured model. In contrast, we define the physical volume $V_{\rm phys}$ by Eq. (3.1.15) not only for the non-punctured model but also for the punctured model, which simplifies the relationship between β and L for fixed $V_{\rm phys}$.

In Fig. 3.12, we show our results for the average plaquette w (Top), the topological charge (Middle) and the topological susceptibility χ (Bottom) against θ for $(\beta, L) = (3, 10)$ and $(12, 20)$ in the left and right columns, respectively, which correspond to a fixed physical volume $V_{\rm phys} \equiv L^2/\beta = 10^2/3$. The exact results obtained for the same model with the same parameter sets are also shown for comparison. We find from our results for the average plaquette that the exact results are reproduced for $(\beta, L) = (12, 20)$, but there

[3] We find, however, that the fluctuation of the local unitarity norm is small even for the one $\mathcal{N}(K)$ at the puncture, which implies that the distribution of each link variable has fast fall-off. Therefore, it is suggested that the problem due to the boundary terms discussed in Refs. [3, 4, 72, 73] does not occur.

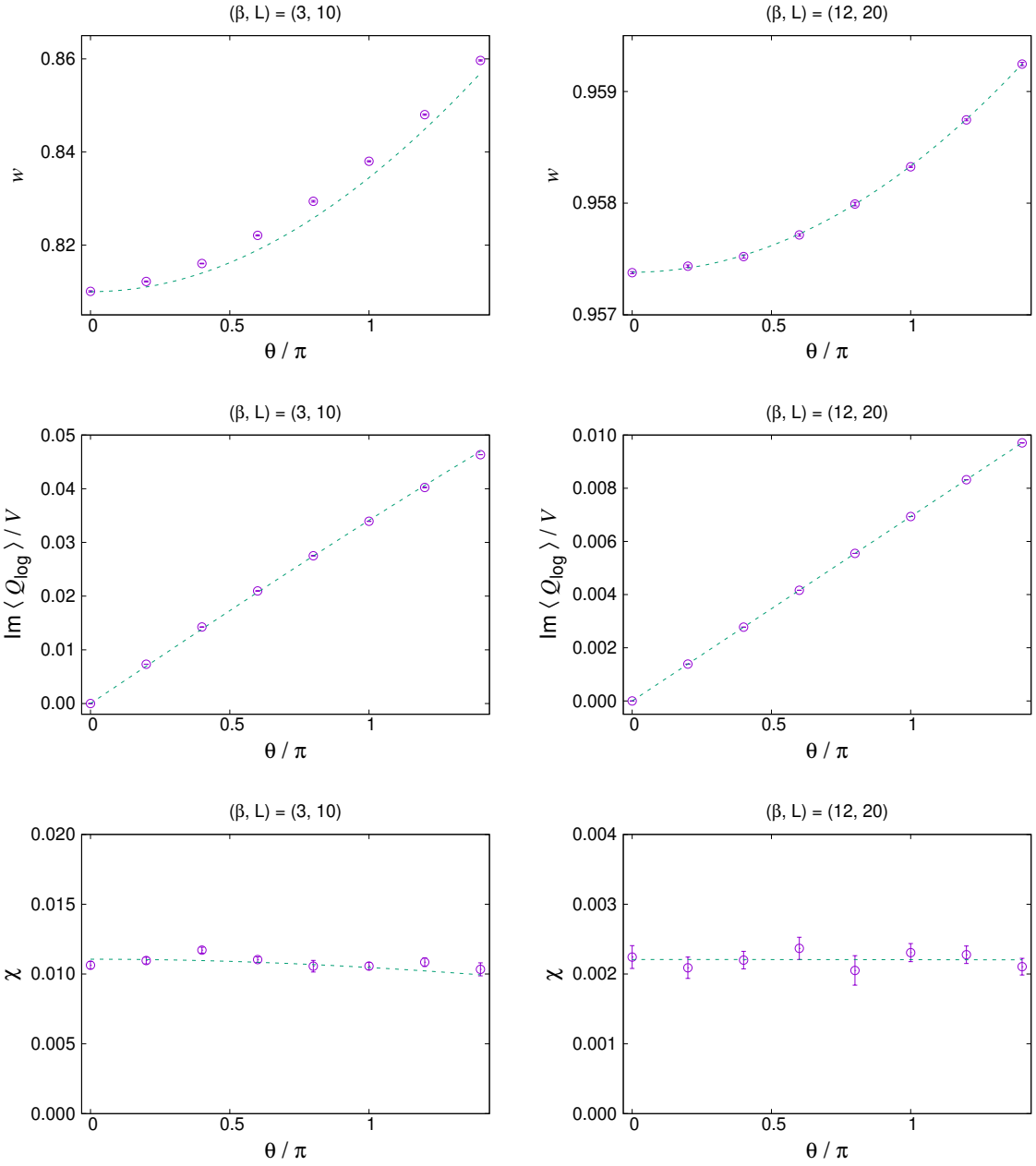

Figure 3.12: The results for various observables obtained by the CLM for the punctured model with the log definition $Q_{\log}$. The average plaquette (Top), the imaginary part of the topological charge density (Middle), the topological susceptibility (Bottom) are plotted against θ for $(\beta, L) = (3, 10)$ (Left) and $(12, 20)$ (Right). The exact results for the same (β, L) are shown by the dashed lines for comparison.

is slight deviation for $(\beta, L) = (3, 10)$. This is consistent with our observation in Section 3.4.3 that the condition for correct convergence is met for $(\beta, L) = (12, 20)$ but not for $(\beta, L) = (3, 10)$.

For the topological charge, we find that our results reproduce the exact results not only for $(\beta, L) = (12, 20)$ but also for $(\beta, L) = (3, 10)$. The same holds for the topological susceptibility. We consider that the agreement observed here for $(\beta, L) = (3, 10)$ is accidental, though, since the condition for correct convergence is not satisfied. The fact that the results of the CLM for the punctured model with $(\beta, L) = (3, 10)$ is not as bad as those for the non-punctured model with the same (β, L) shown in Fig. 3.2(Left) can be understood by considering that the effect of the θ term is included correctly by the drift terms for the link variables composing the removed plaquette, but it is only the infrequent branch cut crossing of the other plaquettes that spoils the validity of the CLM.

Chapter 4

4D SU(2) gauge theory with a θ term

There are some predictions about the phase structure around $\theta = \pi$ by using the 't Hooft anomaly matching condition. The aim of this work is to investigate the phase structure around $\theta = \pi$ by using the CLM.

4.1 Lattice formulation of the 4D SU(2) gauge theory

In this section, we review 4D SU(2) gauge theory with a θ term and discuss how to define it on a lattice.

In the continuum 4D SU(N) gauge theory, the kinetic term for gauge field $A_\mu = A_\mu^a t^a$ is given by

$$S_{\rm g} = \frac{1}{2g^2}\int d^4x \,{\rm Tr}\,[F_{\mu\nu}F_{\mu\nu}] = \frac{1}{4g^2}\int d^4x F^a_{\mu\nu}F^a_{\mu\nu}, \tag{4.1.1}$$

where μ, ν run from 1 to 4, an index a labels the generators of SU(N), g is the gauge coupling constant, and $F_{\mu\nu}$ is the field strength defined by

$$F_{\mu\nu} = \partial_\mu A_\nu - \partial_\nu A_\mu + i\,[A_\mu, A_\nu] = F^a_{\mu\nu}t^a. \tag{4.1.2}$$

We use the Hermitian generators t^a which satisfy the following relations:

$$(t^a)^\dagger = t^a, \tag{4.1.3}$$

$${\rm Tr}\, t^a = 0, \tag{4.1.4}$$

$$[t^a, t^b] = if^{abc}t^c, \tag{4.1.5}$$

$${\rm Tr}\, t^a t^b = \tfrac{1}{2}\delta^{ab}. \tag{4.1.6}$$

In 4D gauge theories, the topological charge is defined by

$$Q = \frac{1}{32\pi^2}\int d^4x \epsilon_{\mu\nu\rho\sigma}\,{\rm Tr}\,[F_{\mu\nu}F_{\rho\sigma}] = \frac{1}{64\pi^2}\int d^4x \epsilon_{\mu\nu\rho\sigma}F^a_{\mu\nu}F^a_{\rho\sigma}, \tag{4.1.7}$$

which becomes some integer when the base manifold is compact. Therefore, the total action is composed by the kinetic term and the θ term as

$$S = S_{\rm g} + S_\theta, \tag{4.1.8}$$

$$S_\theta = -i\theta Q, \tag{4.1.9}$$

where $S_{\rm g}$ is given by (4.1.1).

We put this theory on the $L_1 \times L_2 \times L_3 \times L_4$ lattice. In the rest of this section, we set $L_1 = L_2 = L_3 = L_{\rm s}$ and $L_4 = L_{\rm t}$. For the lattice formulation of gauge theories, we introduce link variables $U_{n,\mu}$ which are related to gauge fields $A_{n,\mu}$ as

$$U_{n,\mu} = e^{iaA_{n,\mu}}, \tag{4.1.10}$$

where $n = (n_1, n_2, n_3, n_4)$ represents the position on the lattice, and a is a lattice spacing.

The simplest gauge action is the plaquette action which is sometimes called as the Wilson action. The action is defined as

$$\begin{aligned} S_{\rm g}^{\rm lat} &= \frac{\beta}{2N} \sum_n \sum_{\mu \neq \nu} {\rm Tr}\,(I - P_n^{\mu\nu}) \\ &= 6\beta V - \frac{\beta}{2N} \sum_n \sum_{\mu < \nu} {\rm Tr}\,[P_n^{\mu\nu} + (P_n^{\mu\nu})^{-1}], \end{aligned} \tag{4.1.11}$$

where $V = L_{\rm s}^3 \times L_{\rm t}$ is the lattice volume, β is related to the gauge coupling as

$$\beta = \frac{2N}{g^2}, \tag{4.1.12}$$

and $P_n^{\mu\nu}$ is a plaquette which is defined by

$$P_n^{\mu\nu} = U_{n,\mu} U_{n+\hat{\mu},\nu} U_{n+\hat{\nu},\mu}^{-1} U_{n,\nu}^{-1}. \tag{4.1.13}$$

Next, we consider the lattice formulation of the topological charge. There are some definitions of the topological charge on the lattice. Comparisons between different definitions have been discussed in [74, 75].

In this work, we use the most commonly used definition, namely the cloverleaf definition which is introduced in [76]. The cloverleaf definition of the topological charge is given by

$$Q_{\rm L} := -\frac{1}{32\pi^2} \sum_n \frac{1}{2^4} \sum_{\mu,\nu,\rho,\sigma=\pm 1}^{\pm 4} \tilde{\epsilon}_{\mu\nu\rho\sigma}\, {\rm Tr}\,[P_n^{\mu\nu} P_n^{\rho\sigma}]\,, \tag{4.1.14}$$

where $\tilde{\epsilon}_{\mu\nu\rho\sigma}$ is defined as

$$\tilde{\epsilon}_{\mu\nu\rho\sigma} = {\rm sgn}(\mu\nu\rho\sigma) \epsilon_{|\mu||\nu||\rho||\sigma|}, \tag{4.1.15}$$

where $\epsilon_{\mu\nu\rho\sigma}$ is the Levi-Civita symbol. The plaquettes for the negative directions are defined as

$$\begin{aligned} P_n^{-\mu\nu} &= U_{n-\hat{\mu},\mu}^{-1} U_{n-\hat{\mu},\nu} U_{n-\hat{\mu}+\hat{\nu},\mu} U_{n,\nu}^{-1}, \\ P_n^{\mu-\nu} &= U_{n,\mu} U_{n+\hat{\mu}-\hat{\nu},\nu}^{-1} U_{n-\hat{\nu},\mu}^{-1} U_{n-\hat{\nu},\nu}, \\ P_n^{-\mu-\nu} &= U_{n-\hat{\mu},\mu}^{-1} U_{n-\hat{\mu}-\hat{\nu},\nu}^{-1} U_{n-\hat{\mu}-\hat{\nu},\mu} U_{n-\hat{\nu},\nu}. \end{aligned} \tag{4.1.16}$$

By introducing the cloverleaf $\bar{P}_n^{\mu\nu}$ whose definition is

$$\bar{P}_n^{\mu\nu} = P_n^{\mu\nu} - P_n^{-\mu\nu} - P_n^{\mu-\nu} + P_n^{-\mu-\nu}, \tag{4.1.17}$$

then the definition (4.1.14) can be rewritten as

$$Q_{\mathrm{L}} = -\frac{1}{32\pi^2}\sum_n \frac{1}{2^4}\sum_{\mu,\nu,\rho,\sigma=1}^{4} \epsilon_{\mu\nu\rho\sigma}\,\mathrm{Tr}\left[\bar{P}_n^{\mu\nu}\bar{P}_n^{\rho\sigma}\right]. \tag{4.1.18}$$

Moreover, the lattice definition of topological charge (4.1.18) can be rewritten in a simpler form as

$$Q_{\mathrm{L}} = -\frac{1}{256\pi^2}\sum_n \mathrm{Tr}\left[R_n^{12}R_n^{34} + R_n^{13}R_n^{42} + R_n^{23}R_n^{14}\right], \tag{4.1.19}$$

where $R_n^{\mu\nu}$ is defined as

$$R_n^{\mu\nu} := \bar{P}_n^{\mu\nu} - \bar{P}_n^{\nu\mu}. \tag{4.1.20}$$

$R_n^{\mu\nu}$ is anti-symmetric under a swapping of indices μ and ν as $R_n^{\mu\nu} = -R_n^{\nu\mu}$.

This topological charge is not an integer when the lattice spacing a is finite. In the continuum limit, the lattice topological charge becomes some integer.

4.2 Application of the CLM to the 4D SU(2) lattice gauge theory

We apply the CLM to the 4D SU(2) lattice gauge theory with a θ term. The link variables are extended from $U_{n,\mu} \in \mathrm{SU}(2)$ to $\mathcal{U}_{n,\mu} \in \mathrm{SL}(2,\mathbb{C})$. Then we consider a fictitious time evolution of the link variables $\mathcal{U}_{n,\mu}(t)$ governed by the complex Langevin equation

$$\mathcal{U}_{n,\mu}(t+\Delta t) = \mathcal{U}_{n,\mu}(t)\exp\left[i\Big\{-\Delta t\, D^a_{n,\mu}S\; t^a + \sqrt{\Delta t}\,\eta_{n,\mu}(t)\Big\}\right], \tag{4.2.1}$$

where t is the fictitious time, Δt is a step size, and $\eta_{n,\mu}(t)$ is the Gaussian noise. The drift term $D^a_{n,\mu}S$ is defined by

$$D^a_{n,\mu}S = \lim_{\epsilon\to 0}\frac{S(e^{i\epsilon t^a}U_{n,\mu}) - S(U_{n,\mu})}{\epsilon}, \tag{4.2.2}$$

first for the unitary link variables $U_{n,\mu}(t)$, and then it is defined for the complexified link variables $\mathcal{U}_{n,\mu}(t)$ by analytic continuation in order to respect holomorphicity.

The drift term $D^a_{n,\mu}S$ is consist of two part

$$D^a_{n,\mu}S = D^a_{n,\mu}S_{\mathrm{g}} + D^a_{n,\mu}S_\theta, \tag{4.2.3}$$

where the first term is defined as

$$D^a_{n,\mu}S_{\mathrm{g}} = -i\beta\mathrm{Tr}\left[t^a\sum_{\nu\neq\mu}(P_n^{\mu\nu} + P_n^{\mu-\nu} - P_n^{-\nu\mu} - P_n^{\nu\mu})\right], \tag{4.2.4}$$

and the second term is defined as

$$
\begin{aligned}
D^a_{n,\mu} S_\theta &= \frac{i\theta}{256\pi^2} D^a_{n,\mu} \sum_n \mathrm{Tr}\,[R^{12}_n R^{34}_n - R^{13}_n R^{24}_n + R^{14}_n R^{23}] \\
&= -\frac{\theta}{256\pi^2} \mathrm{Tr}\,[t^a \{ \delta_{\mu 1}(K^{34}_{n,12} - K^{24}_{n,13} + K^{23}_{n,14}) \\
&\qquad + \delta_{\mu 2}(-K^{34}_{n,21} - K^{13}_{n,24} + K^{23}_{n,14}) \\
&\qquad + \delta_{\mu 3}(K^{12}_{n,34} + K^{24}_{n,31} - K^{23}_{n,14}) \\
&\qquad + \delta_{\mu 4}(-K^{12}_{n,43} + K^{13}_{n,24} - K^{23}_{n,41}) \}] \\
&=: -\frac{\theta}{256\pi^2} \mathrm{Tr}\,[t^a J^{(\theta)}_{n,\mu}],
\end{aligned}
\tag{4.2.5}
$$

$$
K^{\rho\sigma}_{n,\mu\nu} := U_{n,\mu} f^{\rho\sigma}_{n,\mu\nu}(U) + g^{\rho\sigma}_{n,\mu\nu}(U) U^{-1}_{n,\mu}, \tag{4.2.6}
$$

$$
\begin{aligned}
f^{\rho\sigma}_{n,\mu\nu}(U) :&= U_{n+\hat{\mu},\nu} U^{-1}_{n+\hat{\nu},\mu} U^{-1}_{n,\nu} R^{\rho\sigma}_n - U^{-1}_{n+\hat{\mu}-\hat{\nu},\nu} U^{-1}_{n-\hat{\nu},\mu} R^{\rho\sigma}_{n-\hat{\nu}} U_{n-\hat{\nu},\nu} \\
&+ U_{n+\hat{\mu},\nu} U^{-1}_{n+\hat{\nu},\mu} R^{\rho\sigma}_{n+\hat{\nu}} U^{-1}_{n,\nu} - U^{-1}_{n+\hat{\mu}-\hat{\nu},\nu} R^{\rho\sigma}_{n+\hat{\mu}-\hat{\nu}} U^{-1}_{n-\hat{\nu},\mu} U_{n-\hat{\nu},\nu} \\
&+ R^{\rho\sigma}_{n+\hat{\nu}} U_{n+\hat{\mu},\nu} U^{-1}_{n+\hat{\nu},\mu} U^{-1}_{n,\nu} - U^{-1}_{n+\hat{\mu}-\hat{\nu},\nu} U^{-1}_{n-\hat{\nu},\mu} U_{n-\hat{\nu},\nu} R^{\rho\sigma}_n \\
&+ U_{n+\hat{\mu},\nu} R^{\rho\sigma}_{n+\hat{\mu}+\hat{\nu}} U^{-1}_{n+\hat{\nu},\mu} U^{-1}_{n,\nu} - R^{\rho\sigma}_{n+\hat{\mu}} U^{-1}_{n-\hat{\mu}+\hat{\nu},\nu} U^{-1}_{n-\hat{\nu},\mu} U_{n-\hat{\nu},\nu} \ ,
\end{aligned}
\tag{4.2.7}
$$

$$
\begin{aligned}
g^{\rho\sigma}_{n,\mu\nu}(U) :&= R^{\rho\sigma}_n U_{n,\nu} U_{n+\hat{\nu},\mu} U^{-1}_{n+\hat{\nu},\nu} - U^{-1}_{n-\hat{\nu},\nu} R^{\rho\sigma}_{n-\hat{\nu}} U_{n-\hat{\nu},\mu} U_{n+\hat{\mu}-\hat{\nu},\nu} \\
&+ U_{n,\nu} U_{n+\hat{\nu},\mu} U^{-1}_{n+\hat{\mu},\nu} R^{\rho\sigma}_{n+\hat{\mu}} - R^{\rho\sigma}_n U^{-1}_{n-\hat{\nu},\nu} U_{n-\hat{\nu},\mu} U_{n+\hat{\mu}-\hat{\nu},\nu} \\
&+ U_{n,\nu} R^{\rho\sigma}_{n+\hat{\mu}} U_{n+\hat{\nu},\mu} U^{-1}_{n+\hat{\mu},\nu} - U^{-1}_{n-\hat{\nu},\nu} U_{n-\hat{\nu},\mu} R^{\rho\sigma}_{n+\hat{\mu}-\hat{\nu}} U_{n+\hat{\mu}-\hat{\nu},\nu} \\
&+ U_{n,\nu} U_{n+\hat{\nu},\mu} R_{n+\hat{\mu}+\hat{\nu}} U^{-1}_{n+\hat{\mu},\nu} - U^{-1}_{n-\hat{\mu},\nu} U_{n-\hat{\mu},\mu} U_{n+\hat{\mu}-\hat{\nu},\nu} R^{\rho\sigma}_{n+\hat{\mu}} \ .
\end{aligned}
\tag{4.2.8}
$$

Therefore, the total drift term is

$$
D^a_{n,\mu}(S_\mathrm{g} + S_\theta) = i\mathrm{Tr}\,[J_{n,\mu} t^a], \tag{4.2.9}
$$

$$
J_{n,\mu} := -\beta J^{(g)}_{n,\mu} + \frac{i\theta}{256\pi^2} J^{(\theta)}_{n,\mu}. \tag{4.2.10}
$$

In this work, we use the second-order Runge-Kutta algorithm [77, 78] to reduce the finite step size effects. When we evolve the gauge configuration by (4.2.1), the probability for a gauge configuration $P(U)$ which is realized after the thermalization is given by

$$
P(U) \propto \exp\,(-\tilde{S}), \tag{4.2.11}
$$

where $\tilde{S}$ is

$$
\tilde{S} = \left(1 + \frac{\Delta t\ C_\mathrm{A}}{12}\right) S + \frac{\Delta t}{4} \sum_{n,\mu} \left\{ 2(D^a_{n,\mu})^2 S - (D^a_{n,\mu} S)^2 \right\} + \mathcal{O}\Big((\Delta t)^2\Big), \tag{4.2.12}
$$

and C_A is the Casimir invariant for the adjoint representation. Note that, in the SU(N) case, $C_\mathrm{A} = N$. In other words, when we evolve the gauge configuration by (4.2.1) the observables have $\mathcal{O}(\Delta t)$ systematic errors.

In the second-order Runge-Kutta algorithm, the Langevin evolution is described by the following equations:

$$\begin{aligned} U_{n,\mu}(t+\Delta t) &= U_{n,\mu}(t)\exp\left[i\Big\{-\frac{\Delta t}{2}\left(1+\frac{\Delta t\ C_{\rm A}}{6}\right)v^a_{n\mu}\ t^a+\sqrt{\Delta t}\,\eta_{n,\mu}(t)\Big\}\right]\ , \\ v^a_{n\mu} &= \Big(D^a_{n,\mu}S\big(U(t)\big)+D^a_{n,\mu}S\big(U(t')\big)\Big), \end{aligned} \tag{4.2.13}$$

where a gauge configuration $U(t')$ is obtained by a tentative update as

$$U_{n,\mu}(t') = U_{n,\mu}(t)\exp\left[i\Big\{-\Delta t\,D^a_{n,\mu}S\big(U(t)\big)\ t^a+\sqrt{\Delta t}\,\eta_{n,\mu}(t)\Big\}\right]\ . \tag{4.2.14}$$

By this algorithm, the first order of Δt in (4.2.12) is removed, therefore the probability for a gauge configuration becomes

$$P(U)\propto\exp\Big(-S+\mathcal{O}\big((\Delta t)^2\big)\Big). \tag{4.2.15}$$

Thus, the systematic errors are reduced from $\mathcal{O}(\Delta t)$ to $\mathcal{O}((\Delta t)^2)$. As a result, we can use a larger Δt, which means that the simulations are more efficient.

4.2.1 Gauge cooling

We define a semi-positive definite norm so called the unitarity norm as

$$\mathcal{N}=\frac{1}{4NV}\sum_{n,\mu}\mathrm{Tr}\,[\mathcal{U}^\dagger_{n,\mu}\mathcal{U}_{n,\mu}-I]. \tag{4.2.16}$$

This norm describes how the link variables are far from being unitary. If and only if all link variables are unitary $\mathcal{U}_{n,\mu}\in\mathrm{SU}(2)$, their Hermite conjugates are equivalent to their inverse matrices $\mathcal{U}^\dagger_{n,\mu}=\mathcal{U}^{-1}_{n,\mu}$, therefore the norm is equal to zero. We reduce the norm by a gauge transformation for the extended gauge group as

$$\mathcal{U}_{n,\mu}\longrightarrow g_n\mathcal{U}_{n,\mu}g^{-1}_{n+\mu}\qquad g_n\in\mathrm{SL}(2,\mathbb{C}). \tag{4.2.17}$$

This procedure is called the gauge cooling. The gauge cooling does not affect the expectation values for holomorphic quantities [3].

Next we consider how to choose the gauge transformation. Here we consider the $\mathrm{SL}(2,\mathbb{C})$ gauge transformation for an infinitesimal parameter $\Delta^a_n\in\mathbb{R}$ such as

$$\begin{aligned} g_n &= e^{\Delta^a_n t^a}\sim\mathbb{1}+\Delta^a_n t^a, \\ g_n\mathcal{U}_{n,\mu}g^{-1}_{n+\mu} &= \mathcal{U}_{n,\mu}+\Delta^a_n\mathcal{U}_{n,\mu}-\Delta^a_{n+\hat\mu}\mathcal{U}_{n,\mu}t^a, \\ g^{-1}_{n+\hat\mu}\mathcal{U}^\dagger_{n,\mu}g_n &= \mathcal{U}^\dagger_{n,\mu}-\Delta^a_{n+\hat\mu}\mathcal{U}^\dagger_{n,\mu}+\Delta^a_n\mathcal{U}^\dagger_{n,\mu}t^a. \end{aligned} \tag{4.2.18}$$

The change of the unitarity norm is given by

$$\Delta\mathcal{N}=\frac{1}{2NV}\sum_n\mathrm{Tr}\,[\Delta^a_n\hat G_n t^a], \tag{4.2.19}$$

where $\hat{G}_n$ is defined as

$$\hat{G_n} := \sum_{\mu} (\mathcal{U}_{n,\mu}\mathcal{U}^{\dagger}_{n,\mu} - \mathcal{U}^{\dagger}_{n-\hat{\mu},\mu}\mathcal{U}_{n-\hat{\mu},\mu}), \tag{4.2.20}$$

which satisfies $\hat{G_n} = \hat{G_n}^{\dagger}$. Therefore, we find that the unitarity norm is reduced most efficiently by choosing $\Delta^a_n \propto -\hat{G_n} t^a$.

Using this result, we consider following gauge transformation

$$\mathcal{U}_{n,\mu} \longrightarrow g_n \mathcal{U}_{n,\mu} g^{-1}_{n+\mu}; \qquad g_n = e^{-\alpha G_n}, \tag{4.2.21}$$

where G_n is defined as

$$G_n := \mathrm{Tr}\,[\hat{G}_n t^a] t^a. \tag{4.2.22}$$

After this gauge transformation, the unitarity norm becomes

$$\mathcal{N}'(\alpha) := \frac{1}{4NV} \mathrm{Tr}\,[\mathcal{U}^{\dagger}_{n,\mu} e^{-2\alpha G_n} \mathcal{U}_{n,\mu} e^{2\alpha G_{n+\hat{\mu}}} - \mathbb{1}]. \tag{4.2.23}$$

We search for an optimal value for α that minimize $\mathcal{N}'(\alpha)$. Since we perform the gauge cooling after each Langevin step, the α is typically a small number. Therefore, we expand Eq. (4.2.23) with respect to α up to first order, and we estimate optimal value for α. The optimal value is given by

$$\alpha = \frac{\sum_n ||G_n||^2}{\sum_{n,\mu} ||G_n \mathcal{U}_{n,\mu} - \mathcal{U}_{n,\mu} G_{n+\hat{\mu}}||^2}, \tag{4.2.24}$$

where $||\cdot||$ is the Frobenius norm which is defined as $||A||^2 = \mathrm{Tr}\,(AA^T)$. We repeat this procedure until the change of the unitarity norm becomes less than 10^{-4}.

4.2.2 Adaptive step size

In order to avoid the excursion problem, we also use the adaptive step size algorithm. We measure maximum of the magnitude of the drift term defined as

$$u = \max_{n,\mu} |D^a_{n,\mu} S| \tag{4.2.25}$$

at each Langevin step. When the magnitude of drift term is larger than a threshold u_0, we modify the step size Δt as

$$\Delta t = \begin{cases} \Delta t_0 & \text{for } u < v_0\ , \\ \dfrac{v_0}{u} \Delta t_0 & \text{otherwise}\ , \end{cases} \tag{4.2.26}$$

where Δt_0 is a default step size. In our simulation, we choose the threshold as $u_0 = 3\beta/N_c$ because when $\theta = 0$ the drift term is bounded by this value.

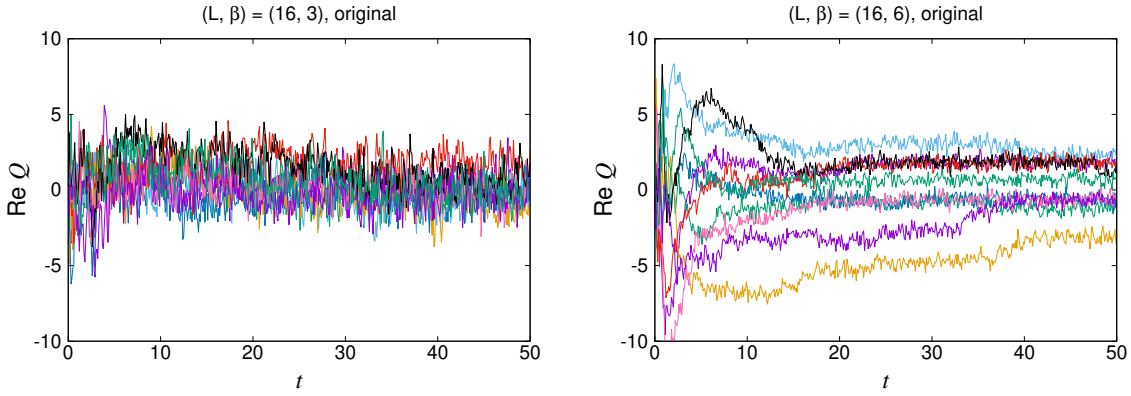

Figure 4.1: We plot the histories of the topological charge for $\theta = 0$. Here we consider $L_{\rm s} = L_{\rm t} = L$ where $L_{\rm s}$ is a number of the lattice point in spatial directions and $L_{\rm t}$ is that in the temporal direction. The simulations start from random SU(2) configurations (hot start). Different lines correspond to different initial configurations. In $(L, \beta) = (16, 3)$ case (Left), the topological charge seems to change frequently. On the other hand, in $(L, \beta) = (16, 6)$ case (Right), the topology does not change during a simulation.

4.3 Result for a naive implementation

First, we impose periodic boundary for all directions.

4.3.1 Autocorrelation of the topological charge

First of all, we study the behaviors of the topological charge at $\theta = 0$ where the CLM turns out to be the real Langevin method. We show the histories of the topological charge in Fig. 4.1. In the small β case, the topological charge seems to change during a simulation. On the other hand, in the large β case, the topology freezing problem occurs. This situation resembles the 2D U(1) case.

We also measure the distributions of the topological charge, and we show them in Fig. 4.2. The width becomes large as the β becomes small. Note that, unlike in the 2D U(1) with the sine definition case, we cannot find the region where the comb-shaped distribution of the charge appears because of the large UV fluctuations.

We can reduce the UV fluctuations by a cooling procedure such as the gradient flow. In the gradient flow technique, the gauge configurations are evolved by the following equation:

$$\begin{aligned} V_{n,\mu}(\tau + \Delta\tau) &= V_{n,\mu}(\tau) \exp\left[i \Big\{ -\Delta\tau \, D^a_{n,\mu} S \; t^a \Big\} \right] , \\ V_{n,\mu}(0) &= U_{n,\mu}, \end{aligned} \tag{4.3.1}$$

where τ is called as the flow time. Eq. (4.3.1) is equivalent to the Langevin evolution (4.2.1) without the noise term. After the gradient flow, the comb-shaped distribution

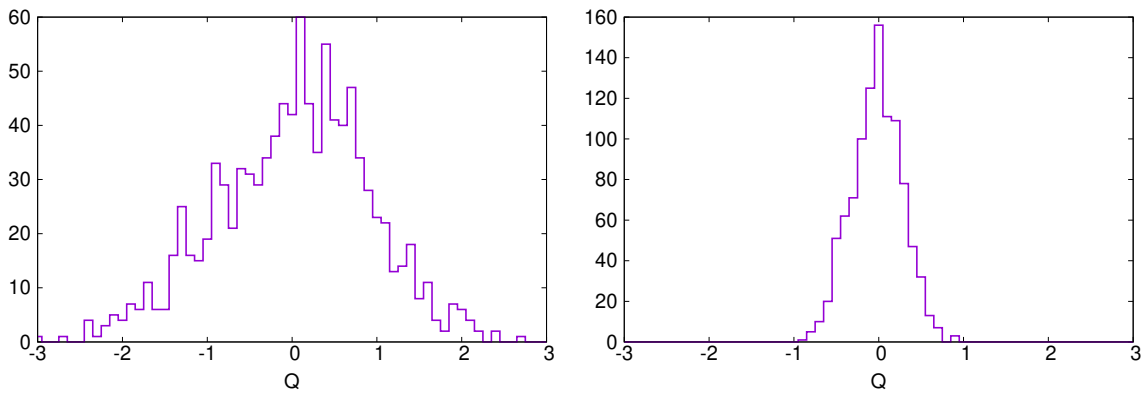

Figure 4.2: We plot the histograms of the topological charge for $\theta = 0$. Here, we set $L_{\rm s} = L_{\rm t} = 16$. In $\beta = 3$ case (Left), the topological charge is distributed in $(-3, 3)$. On the other hands, in $\beta = 6$ case (Right), the topological charge is distributed in $(-1, 1)$.

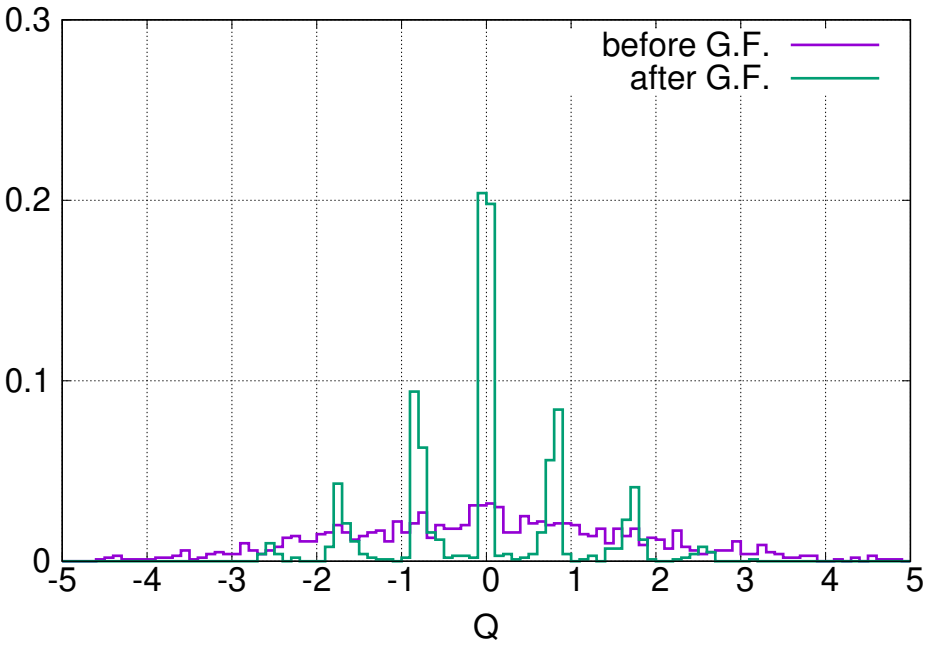

Figure 4.3: The charge distributions before and after the gradient flow. The parameters are $L_{\rm s} = L_{\rm t} = 8$, $\beta = 1.0$ and $\theta = 0$. We use $\Delta t = 10^{-3}$ for generating the configurations by real Langevin method, and we use $\Delta\tau = 10^{-1}$ for the gradient flow. The total flow time is 10.

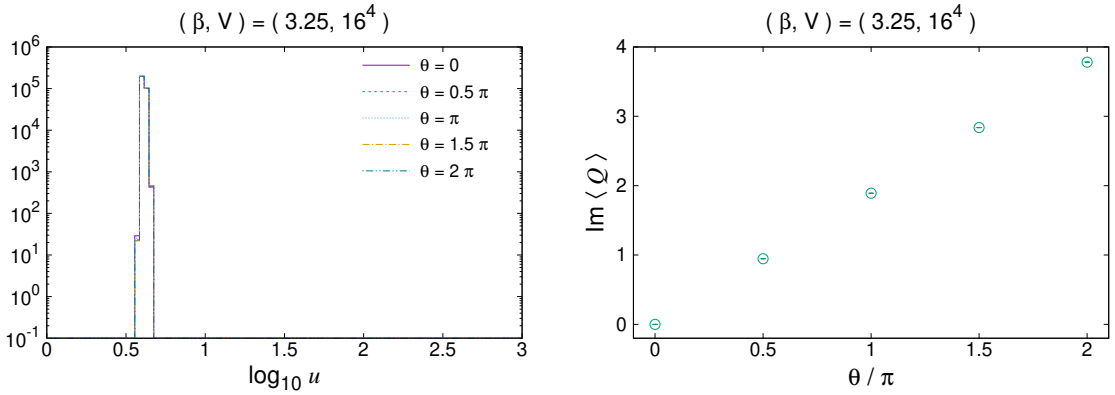

Figure 4.4: The results obtained by the CLM for various θ with $L_{\rm s} = L_{\rm t} = 16$ and $\beta = 3.25$. (Left) The histogram of the magnitude of the drift term defined by (4.2.25). (Right) The imaginary part of the topological charge.

of the topological charge appears (see Fig. 4.3). However, the gradient flow technique cannot be justified in the CLM, therefore we cannot use this technique at $\theta \neq 0$.

4.3.2 Finite θ simulation

We turn on the θ at small β where the topology freezing problem does not occur. In Fig. 4.4 (Left), we plot the histogram of the drift terms for various θ. We find that the criterion for the correct convergence of the CLM is satisfied up to $\theta = 2\pi$. In Fig. 4.4 (Right), the imaginary part of the topological charge whose gradient becomes the topological susceptibility is plotted against the θ. We cannot see the 2π periodicity which the theory has. We consider the reason for this problem is the large UV fluctuations. Since we cannot use the gradient flow in the CLM, a possible way to reduce the UV fluctuations is increasing β, which corresponds to decreasing the lattice spacing a. However, in the large β region, there is the topology freezing problem. Therefore, we need to solve this problem.

4.4 Modifying the boundary condition

4.4.1 Open boundary condition for one spatial direction

Some methods to overcome the topology freezing problem have been studied [79, 80, 81, 82, 83, 84]. In particular, Luscher and Schaefer suggested modifying the boundary condition. In [79], they impose the open boundary condition in the imaginary time direction focusing on the zero temperature case. They found that the topology freezing problem is alleviated by this method. They also found that a drawback of this method is a strong finite volume effect.

In this study, since we want to study the theory at finite temperature, we need to impose the periodic boundary condition for the imaginary time direction. Thus, we impose the open boundary condition in the spatial directions. Since we want to avoid large finite volume effects from the boundaries, first we try to impose the open boundary condition for only one of the spatial directions.

Here we impose the open boundary condition for n_1 direction. In this case the Wilson gauge action is rewritten as

$$S_{\rm g}^{(\text{lat, obc})} = \frac{\beta}{2N} \sum_n \sum_{\mu \neq \nu} w_n^{\mu\nu} \ \mathrm{Tr}\,(I - P_n^{\mu\nu}), \tag{4.4.1}$$

where $w_n^{\mu\nu}$ are weights. Except for at the boundary ($n_1 = 1$ or $n_1 = L_1$), these weights are unity. At the boundary these weights are

$$w_n^{\mu\nu} = \begin{cases} 0 & (n_1, \mu) = (L_1, 1)|_{\nu \neq \mu}, \\ \frac{1}{2} & (n_1, \mu, \nu) = (1,2,3), (1,2,4), (1,3,4), (L_1,2,3), (L_1,2,4), (L_1,3,4), \\ 1 & \text{otherwise}, \end{cases} \tag{4.4.2}$$

where we consider only for $\mu < \nu$ case because these weights are symmetric $w_n^{\mu\nu} = w_n^{\nu\mu}$. In the periodic boundary case, each of the plaquettes belongs to 4 unit hypercubes. On the other hands, in the open boundary for one spatial direction case, at the boundary, half of the hypercubes are absent for some plaquettes. Therefore, some plaquettes at the boundary belong to only 2 unit hypercubes. In this reason we use $w_n^{\mu\nu} = \frac{2}{4} = \frac{1}{2}$ for such plaquettes.

In the open boundary case, we removed the cloverleaves at the boundary from the summation in the definition of the topological charge (4.1.18). In Fig. 4.5, we plot the histories of the topological charge at $\beta = 6$ in the periodic boundary case (Left) and that in the open boundary case (Right). We find that the topology freezing problem seems to be alleviated. However, the autocorrelation time is still long even if we impose the open boundary condition. We expect that the autocorrelation time decreases if we impose the open boundary condition for all spatial directions.

4.4.2 Open boundary condition for all spatial directions

We impose the open boundary conditions for all spatial directions to solve the topology freezing problem. The weights in (4.4.1) are determined by the same way as we explained in the previous subsection.

In Fig. 4.6, we plot the histories of the topological charge in the case of the open boundaries for all spatial directions. We find that the topology freezing is more milder than that for the case of open boundary for one of the spatial directions.

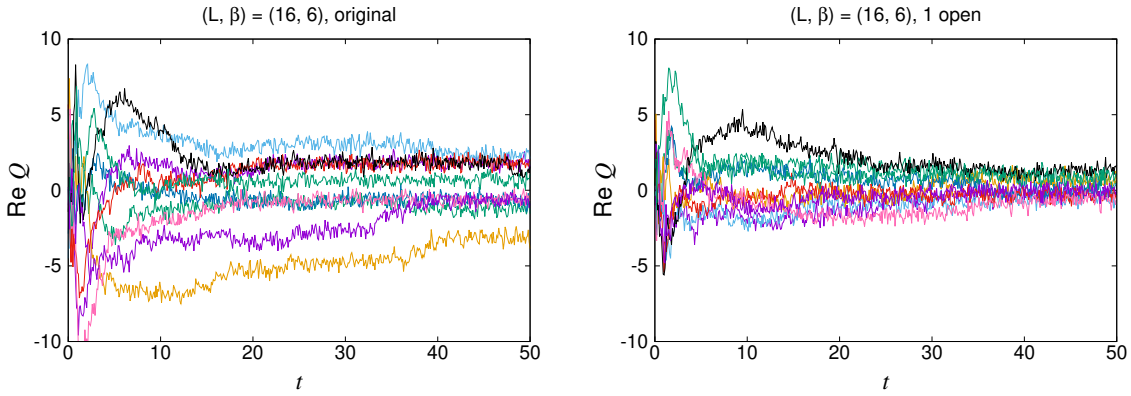

Figure 4.5: We plot the histories of the topological charge for $\theta = 0$ with $(L, \beta) = (16, 6)$. The simulations start from random SU(2) configurations (hot start). Different lines correspond to different initial configurations. We plot the histories in the periodic boundary case in (Left), on the other hand, that in the open boundary for only one spatial direction is plotted in (Right). We cannot see the qualitative difference between them.

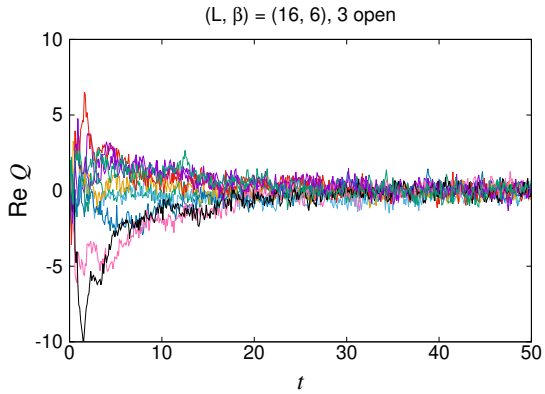

Figure 4.6: We plots the histories of the topological charge for $\theta = 0$ with $(L, \beta) = (16, 6)$. We impose the open boundary condition for all spatial directions. The simulations start from random SU(2) configurations (hot start). Different lines correspond to different initial configurations.

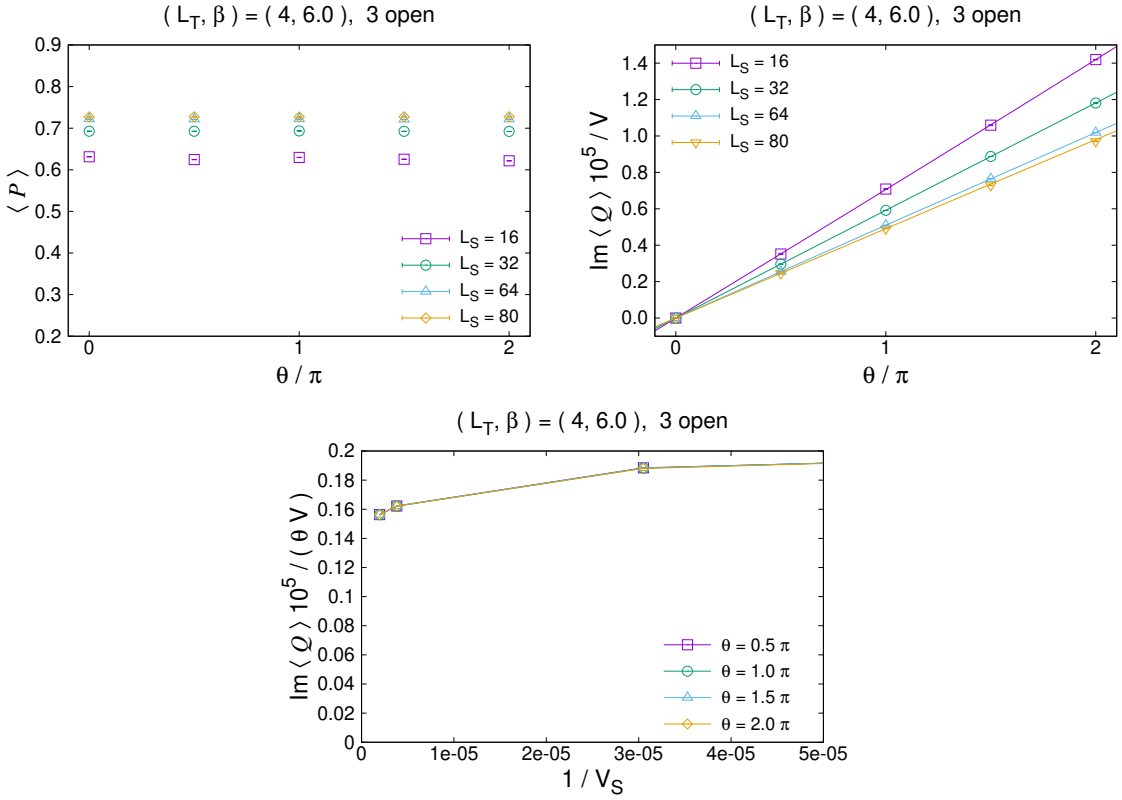

Figure 4.7: We plot the results for $L_t = 4, \beta = 6$ and various L_s at finite θ. Here we impose the open boundary condition for all spatial directions. In all cases, the criterion for the correct convergence of the CLM is satisfied. (Top-Left) The Polyakov loop is plotted against θ for various L_s. (Top-Right) We plot the density of the imaginary part of the topological charge against θ/π. (Bottom) We plot $\mathrm{Im}Q/(\theta V)$ against $1/V_\mathrm{s}$ for $L_\mathrm{s} = 32, 64$ and 80 cases.

In Fig. 4.7 (Top-Left), the Polyakov loop is plotted against θ for various L_s. The Polyakov loop is defined by

$$P = \frac{1}{L_\mathrm{s}^3} \sum_{n_1,n_2,n_3} \prod_{n_4} U_{n,4}, \tag{4.4.3}$$

which is an order parameter to distinguish between the confined and deconfined phases. $\langle P \rangle = 0$ corresponds to the confined phase, while, $\langle P \rangle \neq 0$ corresponds to the deconfined phase. This figure shows that the Polyakov loop has a nonzero value for all cases. This result implies that the theory is in the deconfined phase. In Fig. 4.7 (Top-Right), we plot the density of the imaginary part of Q against θ for various L_s. We find that $\mathrm{Im}(Q)$ linearly increases. We also find that the density of $\mathrm{Im}(Q)$ gradually decreases as L_s increases. In Fig. 4.7 (Bottom), we plot $\mathrm{Im}(Q)/(\theta V)$ against $1/V_\mathrm{s}$, where $V_\mathrm{s} = L_\mathrm{s}^3$ is a spatial lattice volume. We cannot see the finite volume scaling. Therefore, we need to increase V_s more to take $V_\mathrm{s} \to \infty$ extrapolation.

Chapter 5

On the emergence of the space-time structure in the type IIB matrix model

5.1 Brief review of the Lorentzian type IIB matrix model

In this section, we define the Lorentzian type IIB matrix model and its simplified versions, and review some results obtained by Monte Carlo simulations.

5.1.1 Definition of the Lorentzian type IIB matrix model

The action of the type IIB matrix model is given as [47]

$$
\begin{aligned}
S &= S_{\rm b} + S_{\rm f} \ , && (5.1.1)\\
S_{\rm b} &= -\frac{1}{4}{\rm Tr}\Big(\left[A_\mu, A_\nu\right] \left[A^\mu, A^\nu\right] \Big) \ , && (5.1.2)\\
S_{\rm f} &= -\frac{1}{2}{\rm Tr}\Big(\Psi_\alpha \left(\mathcal{C}\Gamma^\mu\right)_{\alpha\beta} \left[A_\mu, \Psi_\beta\right] \Big) \ , && (5.1.3)
\end{aligned}
$$

where A_μ ($\mu = 0, 1, \cdots, 9$) and Ψ_α ($\alpha = 1, \cdots, 16$) are bosonic and fermionic $N \times N$ traceless Hermitian matrices. The indices μ and ν are contracted with the Lorentzian metric $\eta_{\mu\nu} = {\rm diag}(-1, 1, \ldots, 1)$. The 16×16 matrices Γ^μ and $\mathcal{C}$ are the 10-dimensional gamma matrices and the charge conjugation matrix, respectively, obtained after the Weyl projection. The action (5.1.1) has a manifest SO(9,1) Lorentz symmetry, under which A_μ and Ψ_α transform as a Lorentz vector and a Majorana-Weyl spinor, respectively.

This model is invariant under the following transformations

$$
\begin{aligned}
\delta^{(1)} A_\mu &= i\bar{\epsilon_1}\Gamma_\mu \Psi, \\
\delta^{(1)} \Psi &= \frac{i}{2}\Gamma^{\mu\nu}[A_\mu, A_\nu]\epsilon_1,
\end{aligned}
\qquad (5.1.4)
$$

$$\begin{aligned} \delta^{(2)} A_\mu &= 0, \\ \delta^{(2)} \Psi &= \epsilon_2 \mathbb{1}, \end{aligned} \tag{5.1.5}$$

$$\begin{aligned} \delta_{\mathrm{T}} A_\mu &= c_\mu \mathbb{1}, \\ \delta_{\mathrm{T}} \Psi &= 0, \end{aligned} \tag{5.1.6}$$

$$\begin{aligned} \delta_{\mathrm{G}} A_\mu &= i[\lambda, A_\mu], \\ \delta_{\mathrm{G}} \Psi &= i[\lambda, \Psi], \end{aligned} \tag{5.1.7}$$

where ϵ_1 and ϵ_2 are Majorana-Weyl spinors, c_μ is a 10D vector, $\mathbb{1}$ is $N \times N$ unit matrix, and λ is a $N \times N$ Hermitian matrix. The transformation (5.1.7) is the zero volume limit of the 10-dimensional SU(N) gauge transformation.

Here we write the generators of (5.1.4), (5.1.5), and (5.1.6) as $Q^{(1)}$, $Q^{(2)}$, and P_μ respectively. And we define $\tilde{Q}^{(1)}$ and $\tilde{Q}^{(2)}$ as

$$\begin{aligned} \tilde{Q}^{(1)} &= Q^{(1)} + Q^{(2)}, \\ \tilde{Q}^{(2)} &= i(Q^{(1)} - Q^{(2)}). \end{aligned} \tag{5.1.8}$$

These generator satisfies the following relation

$$[\bar{\epsilon}_1 \tilde{Q}^{(i)}, \bar{\epsilon}_2 \tilde{Q}^{(j)}] = -2\delta^{ij} \bar{\epsilon}_1 \Gamma^\mu \epsilon_2 P_\mu, \tag{5.1.9}$$

up to the gauge symmetry (5.1.7) and the equation of motion for fermionic matrices as

$$\Gamma^\mu [A_\mu, \Psi] = 0. \tag{5.1.10}$$

If we identify P_μ as the momentum, the relation corresponds to the algebra of 10 dimensional $\mathcal{N} = 2$ supersymmetry. Therefore (5.1.6) corresponds to translation, which means that we can identify the eigenvalues of the matrices as the space-time coordinates.

There is evidence that the model is considered a promising candidate for the non-perturbative formulation of superstring theory. One is that the action (5.1.1) is recognized as a matrix regularization for the action of the type IIB string theory. Another is that this model can realize the correct interaction between D-branes. Other is that the light-cone string field theory is derived from this model.

The partition function of the Lorentzian type IIB matrix model is defined as [60]

$$Z = \int dA \, d\Psi \, \mathrm{e}^{iS[A,\Psi]} = \int dA \, \mathrm{Pf}\mathcal{M}(A) \, \mathrm{e}^{iS_{\mathrm{b}}} \ , \tag{5.1.11}$$

where the "i" in front of the action is motivated from the fact that the string worldsheet metric has a Lorentzian signature. Note that the bosonic action S_{b} can be written as

$$S_{\mathrm{b}} = \frac{1}{4} \mathrm{Tr} \left(F_{\mu\nu} F^{\mu\nu} \right) = \frac{1}{4} \left\{ -2\mathrm{Tr} \left(F_{0i} \right)^2 + \mathrm{Tr} \left(F_{ij} \right)^2 \right\} \ , \tag{5.1.12}$$

where we have introduced the Hermitian matrices $F_{\mu\nu} = i \left[A_\mu, A_\nu \right]$. Hence S_{b} is not positive semi-definite unlike in the Euclidean case. Note also that, unlike in the Euclidean

version [85, 86], the matrix integral in (5.1.11) is divergent because e^{iS_b} is a pure phase factor and the Pfaffian $\mathrm{Pf}\mathcal{M}(A)$ obtained by integrating out the fermionic matrices is a polynomial in A_μ.

In order to make the partition function (5.1.11) finite, we need to introduce the IR cutoffs both in the temporal and spatial directions, for instance, as

$$\frac{1}{N}\mathrm{Tr}\left\{(A_0)^2\right\}^p \leq \kappa^p \frac{1}{N}\mathrm{Tr}\left\{(A_i)^2\right\}^p \ , \tag{5.1.13}$$

$$\frac{1}{N}\mathrm{Tr}\left\{(A_i)^2\right\}^p \leq L^{2p} \ . \tag{5.1.14}$$

The power p is a parameter, which can be used to test how much the obtained results depend on the way the IR cutoff is introduced [87]. While $p = 1$ would be a natural choice, it was proposed that p should be chosen to be a slightly larger value in order to make the results almost independent of p. Too large values of p lead to pathological behaviors, however.

The Pfaffian $\mathrm{Pf}\mathcal{M}(A)$ in (5.1.11) is real in the Lorentzian version unlike in the Euclidean version, where it becomes complex due to the replacement $A_0 = iA_{10}$. However, the phase factor e^{iS_b} causes the sign problem when one tries to investigate the Lorentzian model by Monte Carlo methods. Here, we avoid this problem[1] following previous work [60, 88, 62] by rewriting the partition function (5.1.11) as

$$Z = \int dA\, \mathrm{Pf}\mathcal{M}(A)\, \delta\Big(\frac{1}{N}\mathrm{Tr}F_{\mu\nu}F^{\mu\nu} - C\Big)\, \delta\Big(\frac{1}{N}\mathrm{Tr}\{(A_i)^2\}^p - 1\Big)\, \theta\Big(\kappa^p - \frac{1}{N}\mathrm{Tr}\{(A_0)^2\}^p\Big) \ , \tag{5.1.15}$$

where $\theta(x)$ is the Heaviside step function. This can be obtained by integrating out the overall scale factor of the bosonic matrices A_μ first and using certain approximation as discussed in section 5.3. The parameter C should be set to zero according to the "derivation", but we generalize the model by choosing $C \neq 0$, which allows us to obtain results for larger matrices in the original $C = 0$ model by using smaller matrices [89, 88]. See Appendix B of ref. [88] for the details of the Monte Carlo simulation of the model (5.1.15).

5.1.2 SSB of rotational SO(9) symmetry

Next we discuss how one can extract the time-evolution from a given matrix configuration generated by Monte Carlo simulation [60]. Since the eigenvalues of the temporal matrix A_0 represents time, we work in an $\mathrm{SU}(N)$ basis which diagonalizes A_0 as

$$A_0 = \mathrm{diag}(\alpha_1, \ldots, \alpha_N) \ , \ \text{where } \alpha_1 < \cdots < \alpha_N \ . \tag{5.1.16}$$

[1] Strictly speaking, the model (5.1.15) is not completely free of sign-problem because the Pfaffian is real but not positive semi-definite. However, configurations with positive Pfaffian dominates the path integral (5.1.15) at large N, and therefore one can safely replace the Pfaffian by its absolute value in the simulation.

In this basis, the spatial matrices A_i turn out to have an approximate band-diagonal structure. By this, we mean that there exists[2] some integer n such that the elements of the spatial matrices $(A_i)_{ab}$ for $|a-b| > n$ are much smaller than those for $|a-b| < n$. Thanks to this structure, we can naturally consider the $n \times n$ submatrices $\bar{A}_i$

$$\left(\bar{A}_i\right)_{IJ}(t) \equiv (A_i)_{\nu+I,\nu+J} \tag{5.1.17}$$

representing the state at time t defined by

$$t \equiv \frac{1}{n}\sum_{I=1}^{n} \alpha_{\nu+I} \ , \tag{5.1.18}$$

where $I, J = 1, \ldots, n$ and $\nu = 0, 1, \ldots, N-n$. For example, we can define the extent of the 9d space at time t using $\bar{A}_i(t)$ as

$$R^2(t) = \left\langle \sum_{i=1}^{9} \frac{1}{n} \mathrm{tr}\left(\bar{A}_i(t)\right)^2 \right\rangle \ , \tag{5.1.19}$$

where the symbol "tr" represents a trace over the $n \times n$ submatrix. We can also define the "moment of inertia tensor"

$$T_{ij}(t) = \frac{1}{n}\mathrm{tr}\left(\bar{A}_i(t)\bar{A}_j(t)\right) \ , \tag{5.1.20}$$

which is a 9×9 real symmetric tensor. The eigenvalues of $T_{ij}(t)$ represent the spatial extent in each of the nine directions at time t, and we denote them by $\lambda_i(t)$ with the ordering

$$\lambda_1(t) > \lambda_2(t) > \cdots > \lambda_9(t) \ . \tag{5.1.21}$$

Note that $R^2(t)$ and $\lambda_i(t)$ are related as

$$R^2(t) = \langle \mathrm{tr}\, T \rangle = \sum_{i=1}^{9} \langle \lambda_i(t) \rangle \ . \tag{5.1.22}$$

The expectation values $\langle \lambda_i(t) \rangle$ can be used as the order parameters for the spontaneous breaking of the rotational SO(9) symmetry of the model. If the nine eigenvalues do not approach a common value in the large-N limit, we conclude that the SO(9) symmetry is spontaneously broken. From the Monte Carlo simulations of the model (5.1.15), it was found [60] that the three eigenvalues $\langle \lambda_i(t) \rangle$ $(i = 1, 2, 3)$ start to grow with t after a critical time t_c, which implies that the SO(9) symmetry is spontaneously broken down to SO(3) for $t > t_c$. (See refs. [88, 62] for a precise definition of the critical time t_c, which we use in this work.)

[2]In practice, the integer n can be determined by observing the scaling behavior for $\sum_i |(A_i)_{ab}|^2$ with $(a+b)/2$ fixed to different values corresponding to different time slices. See section 5 of ref. [62] for the details.

5.1.3 Expanding behaviors in the simplified models

It is interesting to investigate how the 3d space expands with time. For that, one clearly needs to increase the matrix size, which is very time-consuming due to the existence of the Pfaffian in (5.1.15). This led to the proposal of the simplified models, the VDM model [88] and the bosonic model [62], which amounts to replacing the Pfaffian as

$$\mathrm{Pf}\mathcal{M}(A) \Longrightarrow \begin{cases} \Delta(\alpha)^{16} & \text{for the VDM model ,} \\ 1 & \text{for the bosonic model ,} \end{cases} \tag{5.1.23}$$

where $\Delta(\alpha) \equiv \prod_{a>b}^{N}(\alpha_a - \alpha_b)$ is the van der Monde (VDM) determinant. This replacement reduces the computational cost from $O(N^5)$ to $O(N^3)$, which enables simulations with considerably large matrix size. These two models are expected to describe the qualitative behaviors of the original model at early times and at late times, respectively.

In both these models, the spontaneous breaking of the SO(9) rotational symmetry to SO(3) was observed after some critical time as in the original model, and the rate of expansion at late times was investigated. In the VDM model, the extent of space $R(t)$ defined in (5.1.19) exhibits an exponential growth [88]

$$R(t) \sim \mathrm{e}^{\Lambda t} \ , \tag{5.1.24}$$

which is reminiscent of inflation[3] , and this behavior does not seem to change with increasing t. In the bosonic model, on the other hand, the exponential expansion observed at early times changes into a power-law expansion [62]

$$R(t) \sim t^{1/2} \tag{5.1.25}$$

at later times, which is reminiscent of the Friedmann-Robertson-Walker Universe at the radiation dominated era. Based on these results, it has been speculated that the extent of space $R(t)$ in the original model shows an exponential growth at early times and a power-law expansion at later times. If true, it implies that the e-folding or the duration of the cosmic inflation may be determined dynamically in the original model.

5.2 Space-time structure of the matrix configurations

In this section, we investigate the space-time structure of the matrix configurations generated by the Monte Carlo simulation of the model (5.1.15) and the simplified models (5.1.23).

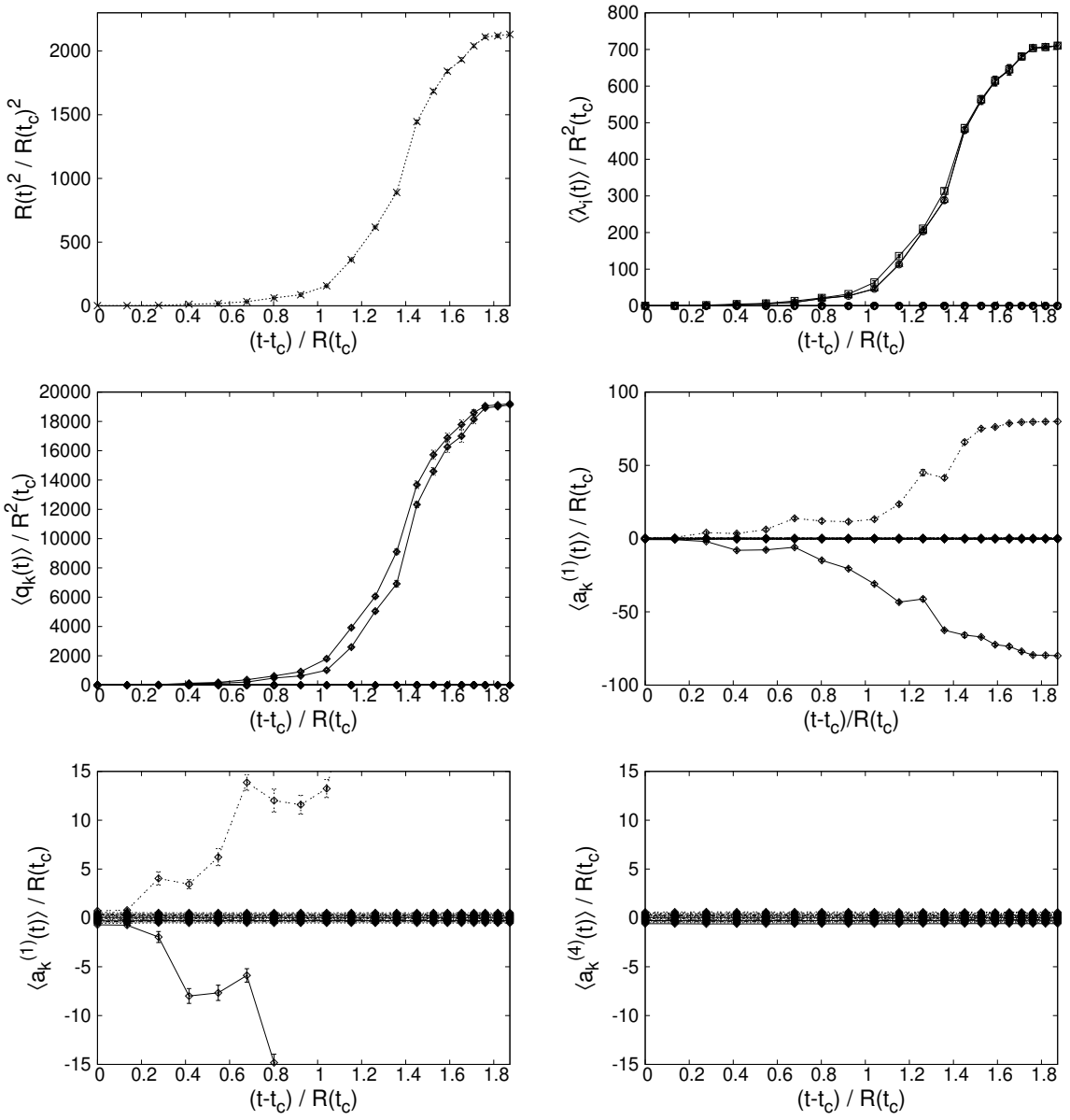

Figure 5.1: The extent of space $R^2(t)/R^2(t_c)$ (Top-Left) and the normalized eigenvalues $\langle\lambda_i(t)\rangle/R^2(t_c)$ of $T_{ij}(t)$ (Top-Right) are plotted against time $(t-t_c)/R(t_c)$ for the bosonic model with $N = 256$, $C = 100$, $\kappa = 1$, $p = 1.5$ and the block size $n = 18$. Similarly, the eigenvalues of $Q(t)/R^2(t_c)$ (Middle-Left), the eigenvalues of $\bar{A}^{(1)}(t)/R(t_c)$ (Middle-Right, Bottom-Left, the latter being the zoom-up version of the former), the eigenvalues of $\bar{A}^{(4)}(t)/R(t_c)$ (Bottom-Right) are plotted against time $(t-t_c)/R(t_c)$.

5.2.1 Results for the bosonic model

In this subsection, we consider the bosonic model, which is a simplified model for the late time behaviors. Let us first look at the basic quantities such as the extent of space $R^2(t)$ and the eigenvalues $\langle \lambda_i(t) \rangle$ of $T_{ij}(t)$. In Fig. 5.1 we plot the extent of space $R^2(t)/R^2(t_c)$ (Top-Left) and the normalized eigenvalues $\langle \lambda_i(t) \rangle / R^2(t_c)$ of $T_{ij}(t)$ (Top-Right) against $(t - t_c)/R(t_c)$ for $N = 256$, $C = 100$, $\kappa = 1.0$ with the block size $n = 18$ in (5.1.19). Here and for all the other plots in Fig. 5.1, we only present the results in the $t < 0$ region since the results are symmetric[4] under the time reflection $t \mapsto -t$. The power p in the IR cutoff (5.1.13) and (5.1.14) is chosen to be $p = 1.5$, which is found to be large enough to make the results almost independent of p (See Appendix C.). Let us recall that $R^2(t)$ is related to $\langle \lambda_i(t) \rangle$ through (5.1.22). While the extent of space $R^2(t)/R^2(t_c)$ grows with t for $t > t_c$, it is only three out of nine eigenvalues of $T_{ij}(t)$ that grow with t, which suggests that the rotational SO(9) symmetry is broken spontaneously to SO(3). These results are analogous to the previous results obtained for $p = 1$ [62].

The simplest way to probe the space-time structure is to define an $n \times n$ matrix

$$Q(t) \equiv \sum_{i=1}^{9} (\bar{A}_i(t))^2, \tag{5.2.1}$$

which is invariant under SO(9) rotations. Let us denote its eigenvalues as $q_k(t)$ ($k = 1, \cdots, n$) with the ordering

$$q_1(t) < \cdots < q_n(t) \ . \tag{5.2.2}$$

These eigenvalues tell us how the space spreads in the radial direction at each time t.

In Fig. 5.1 (Middle-Left), we plot the eigenvalues $q_k(t)/R^2(t_c)$ against $(t - t_c)/R(t_c)$. We find that the two largest eigenvalues grow with t, but not the others. Let us note that the eigenvalues of $Q(t)$ are related to the extent of space $R^2(t)$ as

$$R^2(t) = \left\langle \frac{1}{n} \mathrm{tr}\, Q(t) \right\rangle = \left\langle \frac{1}{n} \sum_{k=1}^{n} q_k(t) \right\rangle \ . \tag{5.2.3}$$

This implies that the time-dependence of $R^2(t)$ seen in the Top-Left panel is caused only by the two largest eigenvalues of $Q(t)$.

Let us next discuss the space-time structure in the three extended directions and the six shrunken directions separately. Since we are dealing with spontaneous symmetry breaking, we need to choose the frame properly in order to distinguish these directions. Suppose $v_j^{(i)}(t)$ ($j = 1, \cdots, 9$) are the normalized eigenvectors of the "moment of inertia

[3]This behavior was observed also in the original model [61] although the matrix size used was not large enough to confirm the long-time behavior.

[4]This does not mean that the Big Crunch occurs in this model because the time difference between the symmetric point $t = 0$ and the critical time $t = t_c$ seems to diverge in physical units in an appropriate large-N limit. See section 5.2.3.

tensor" (5.1.20) corresponding to the eigenvalues $\lambda_i(t)$ with the ordering (5.1.21). Then, we can define the $n \times n$ matrix corresponding to the spatial direction with the extent λ_i as

$$\bar{A}^{(i)}(t) = \sum_{j=1}^{9} v_j^{(i)}(t)\, \bar{A}_j(t) \tag{5.2.4}$$

and its eigenvalues $a_k^{(i)}(t)$ $(k = 1, \cdots, n)$ with the ordering

$$a_1^{(i)}(t) < \cdots < a_n^{(i)}(t) \ . \tag{5.2.5}$$

In Fig. 5.1 (Middle-Right), we plot the eigenvalues $a_k^{(1)}(t)/R(t_c)$ against $(t-t_c)/R(t_c)$. We find that only two eigenvalues $a_1^{(1)}(t)$ and $a_n^{(1)}(t)$ grow in magnitude with time t, and all the others remain close to zero. Similar behaviors are seen also for the eigenvalues $a_k^{(2)}(t)$ and $a_k^{(3)}(t)$ obtained for the other extended directions. In Fig. 5.1 (Bottom-Left), we zoom up the same plot to make visible the eigenvalues close to zero. In Fig. 5.1 (Bottom-Right), we plot the eigenvalues $a_k^{(4)}(t)/R(t_c)$ against $(t - t_c)/R(t_c)$. We find that all the eigenvalues remain close to zero. Similar behaviors are seen also for the eigenvalues $a_k^{(5)}(t), \cdots, a_k^{(9)}(t)$ obtained for the other shrunken directions. Comparing the two plots at the bottom of Fig. 5.1, we notice that the eigenvalue distribution of $\bar{A}^{(i)}$ is almost identical for the extended directions and the shrunken directions except for the two eigenvalues with large magnitude.

Similarly to (5.2.3), the eigenvalues of $\bar{A}^{(i)}(t)$ are related to the extent of space $\lambda_i(t)$ in the ith direction as

$$\lambda_i(t) = \frac{1}{n} \sum_{k=1}^{n} \left(a_k^{(i)}(t) \right)^2 \ . \tag{5.2.6}$$

Our observation implies that the spontaneous symmetry breaking of the SO(9) rotational symmetry seen in the Top-Right panel is caused only by the two eigenvalues of $\bar{A}^{(i)}(t)$ with large magnitude.

5.2.2 Including fermionic contributions

In order to seek for the possibility to obtain a regular space-time, we repeat the analysis in the previous subsection in the case of the original model (5.1.15) including fermionic contributions. Since the cost of Monte Carlo simulations increases from $O(N^3)$ to $O(N^5)$, here we restrict ourselves to a rather small matrix size $N = 16$.

In Fig. 5.2 we plot the same quantities as in Fig. 5.1 for the original model with $N = 16$, $C = 3.91$, $\kappa = 0.38$ and the block size $n = 6$. The power p in the IR cutoff (5.1.13) and (5.1.14) is chosen to be $p = 1.6$, which is found to be large enough to make the results almost independent of p (See Appendix C.). These results are qualitatively the same as those obtained for the bosonic model. While the fermionic matrices are expected to play an important role in the properties of the model such as the expanding behavior, they do not seem to affect the singular space-time structure.

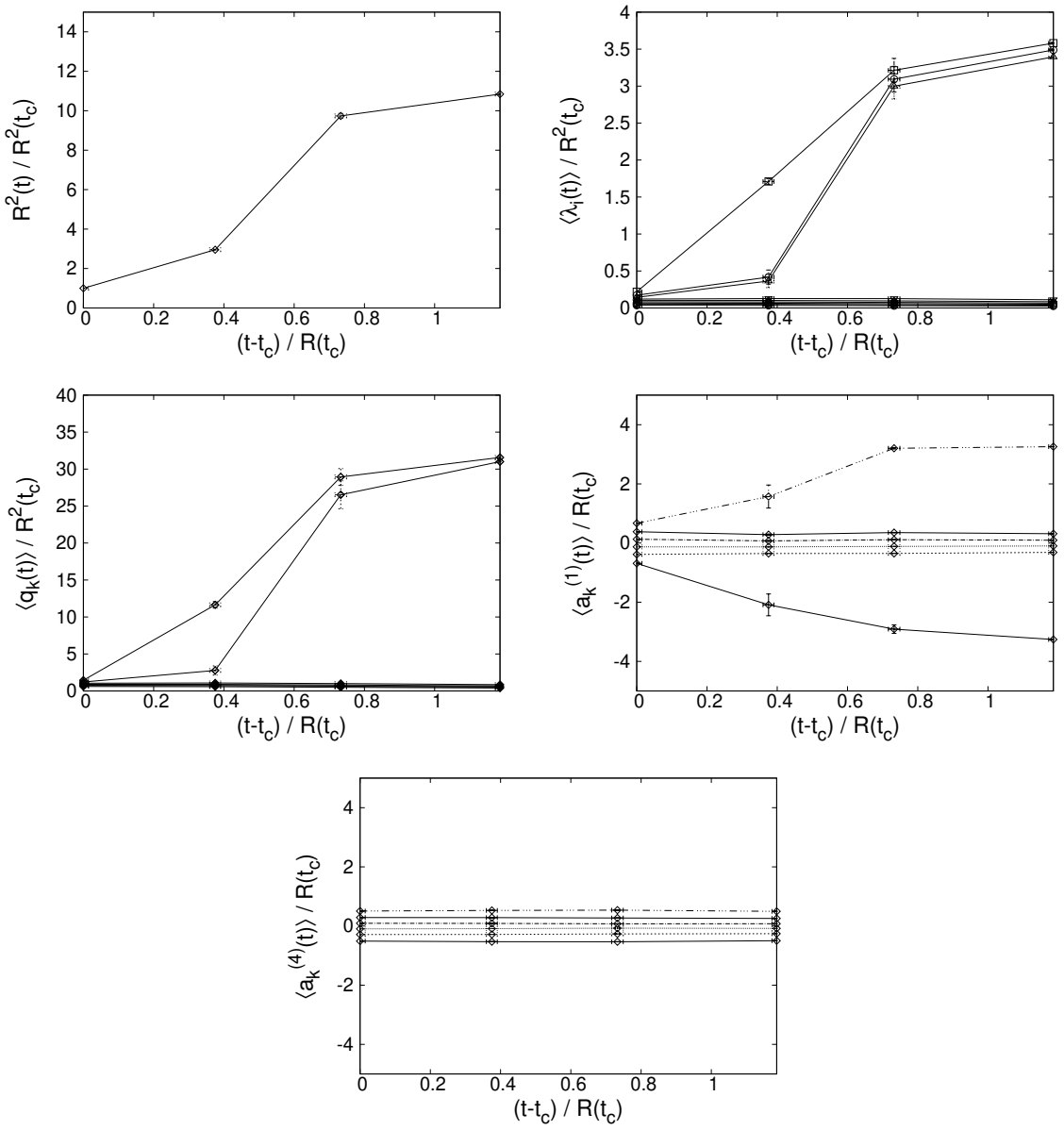

Figure 5.2: The extent of space $R^2(t)/R^2(t_c)$ (Top-Left) and the normalized eigenvalues $\langle\lambda_i(t)\rangle/R^2(t_c)$ of $T_{ij}(t)$ (Top-Right) are plotted against time $(t-t_c)/R(t_c)$ for the original model with $N = 16$, $C = 3.91$, $\kappa = 0.38$, $p = 1.6$ and the block size $n = 6$. Similarly, the eigenvalues of $Q(t)/R^2(t_c)$ (Middle-Left), the eigenvalues of $A^{(1)}(t)/R(t_c)$ (Middle-Right) and the eigenvalues of $A^{(4)}(t)/R(t_c)$ (Bottom) are plotted against time $(t-t_c)/R(t_c)$.

N	C	κ	n	Δ	ϵ
64	8.81	0.14	24	1.0990(16)	0.0550(1)
96	0	2.00	14	1.3811(41)	0.1151(3)
64	0	2.00	10	1.2726(63)	0.1591(8)
64	0	4.00	7	1.3762(87)	0.2752(17)

Table 5.1: The parameter sets (N, C, κ) used for the simulation of the VDM model are listed. We also present the block size n, the "volume" Δ and the "lattice spacing" ϵ determined from the data for each parameter set.

5.2.3 Taking the continuum limit

As yet another possibility to obtain a regular space-time, let us consider taking the continuum limit. Here we use the VDM model, which is a simplified model for the early time behaviors. In Fig. 5.3 (Top-Left), we plot the extent of space $R^2(t)/R^2(t_c)$ against time $(t-t_c)/R(t_c)$ for various N, C and κ with the block size n listed in table 5.1. The power p in the IR cutoff (5.1.13) and (5.1.14) is chosen as $p = 1.4$ following ref. [87]. From this plot, we observe a clear scaling behavior for $(t-t_c)/R(t_c) \lesssim 0.40$.

In Fig. 5.3 (Top-Right), we plot the normalized eigenvalues $\langle \lambda_i(t) \rangle / R^2(t_c)$ of $T_{ij}(t)$ for the VDM model with $N = 96$, $C = 0$ and $\kappa = 2$. Similar behaviors are obtained for the other parameter sets. We find that three out of nine eigenvalues of $T_{ij}(t)$ grow with time, which suggests that the rotational SO(9) symmetry is broken spontaneously to SO(3) for $t > t_c$. These results are similar to those obtained in refs. [88, 87].

In order to discuss the continuum limit, let us define the "volume" and the "lattice spacing" in the temporal direction as [88]

$$\Delta \equiv \frac{t_{\rm peak} - t_c}{R(t_c)} , \qquad \epsilon \equiv \frac{\Delta}{\nu} , \tag{5.2.7}$$

where $t_{\rm peak}$ represents the position of the peak in $R^2(t)$ and ν is the number of data points of $R^2(t)$ contained within $t_c < t \leq t_{\rm peak}$. Roughly speaking, the lattice spacing ϵ represents the average horizontal spacing between the adjacent data points of $R^2(t)/R^2(t_c)$. In table 5.1, we present the volume Δ and the lattice spacing ϵ obtained for each parameter set (N, C, κ) used in Fig. 5.3. The deviation from the scaling behavior for $(t-t_c)/R(t_c) > 0.40$ seen in Fig. 5.3 can be understood either as the finite volume effects or as the finite lattice spacing effects depending on the parameter set.

In what follows, we focus on the point $(t-t_c)/R(t_c) \sim 0.40$, at which the results for $R^2(t)/R^2(t_c)$ with the four parameter sets agree with each other. In Fig. 5.3 (Middle-Left), we plot the normalized eigenvalues $\langle q_k(t) \rangle / R^2(t_c)$ $(k = 1, \cdots, n)$ of $Q(t)$ against their label $(k-1)/(n-1)$ for the four parameter sets. This reveals a clear scaling behavior except for the two largest eigenvalues, which grow as the lattice spacing ϵ decreases. Note that the time dependence of $R^2(t)/R^2(t_c)$ is caused by the two largest eigenvalues of $Q(t)$

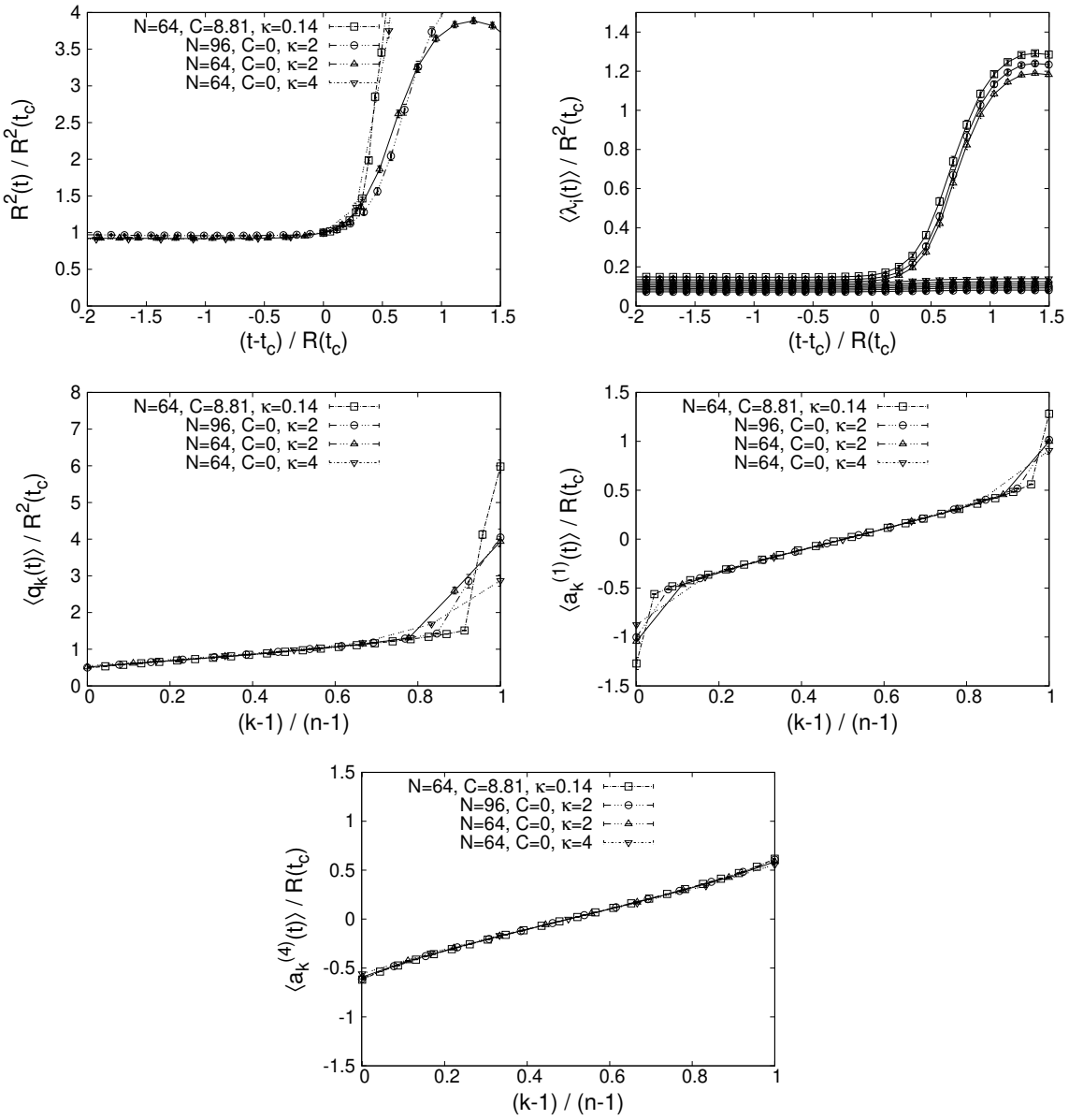

Figure 5.3: (Top-Left) The extent of space $R^2(t)/R^2(t_c)$ is plotted against time $(t - t_c)/R(t_c)$ for the VDM model with the parameter sets (N, C, κ) and the block size n listed in table 5.1. The power p in the IR cutoff (5.1.13) and (5.1.14) is chosen as $p = 1.4$. (Top-Right) The normalized eigenvalues $\langle\lambda_i(t)\rangle/R^2(t_c)$ of $T_{ij}(t)$ are plotted against time $(t-t_c)/R(t_c)$ for $N = 96$, $C = 0$, $\kappa = 2$. The eigenvalues of $Q(t)/R^2(t_c)$ (Middle-Left), the eigenvalues of $\bar{A}^{(1)}(t)/R(t_c)$ (Middle-Right) and the eigenvalues of $\bar{A}^{(4)}(t)/R(t_c)$ (Bottom) obtained at $(t - t_c)/R(t_c) \sim 0.40$ are plotted against their labels $(k - 1)/(n - 1)$ for the four parameter sets listed in table 5.1.

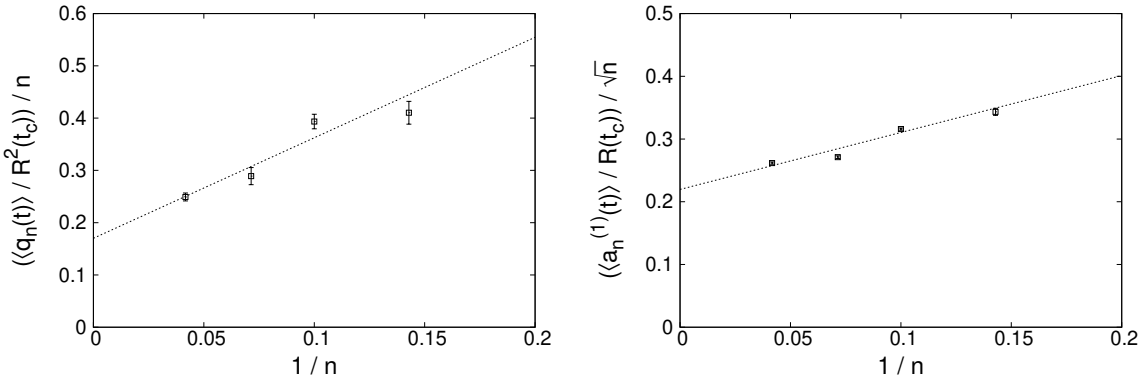

Figure 5.4: (Left) The largest eigenvalue $q_n(t)$ of the matrix $Q(t)$ obtained at $(t - t_c)/R(t_c) \sim 0.40$ and normalized by $R^2(t_c)$ and n is plotted against $1/n$. (Right) The largest eigenvalue $a_n^{(1)}(t)$ of the matrix $\bar{A}^{(1)}(t)$ obtained at $(t - t_c)/R(t_c) \sim 0.40$ and normalized by $R(t_c)$ and $\sqrt{n}$ is plotted against $1/n$.

as we have seen in the previous subsections. Therefore, the scaling of $R^2(t)/R^2(t_c)$ implies that the two largest eigenvalues of $Q(t)$ should grow linearly in n in the continuum limit. This is confirmed numerically in Fig. 5.4 (Left) assuming the presence of $1/n$ corrections.

Let us next consider the space-time structure in the extended directions and the shrunken directions separately. In Fig. 5.3 (Middle-Right), we plot the eigenvalues of $\bar{A}^{(1)}(t)/R(t_c)$ obtained at $(t - t_c)/R(t_c) \approx 0.40$ against the label $(k-1)/(n-1)$. Here again we observe a clear scaling behavior except for the ones at both ends of the spectrum. Similar behaviors are obtained for the other extended directions. According to the same argument as in the previous paragraph, we can deduce that the normalized eigenvalues at both ends of the spectrum grow in magnitude as $\mathrm{O}(\sqrt{n})$ in the continuum limit, which is confirmed in Fig. 5.4 (Right) assuming the presence of $1/n$ corrections.

In Fig. 5.3 (Bottom), we plot the eigenvalues of $\bar{A}^{(4)}(t)/R(t_c)$ obtained at $(t-t_c)/R(t_c) \approx 0.40$ against the label $(k-1)/(n-1)$. We observe a clear scaling behavior here as well. In fact, the eigenvalues are almost the same as those for the extended directions except for the ones at both ends. Similar behaviors are obtained for the other shrunken directions.

Thus we find in the VDM model that the singular space-time structure becomes even more pronounced in the continuum limit instead of getting milder. It is surprising that the two eigenvalues of $\bar{A}^{(i)}(t)/R(t_c)$ $(i = 1, 2, 3)$ actually diverges in the continuum limit although the extent of space defined by $R^2(t)/R^2(t_c)$ remains finite. It is these two eigenvalues that cause the spontaneous breaking of the SO(9) rotational symmetry and the expansion of space. All the other eigenvalues of $\bar{A}^{(i)}(t)/R(t_c)$ remain finite and contribute only to the time-independent SO(9) symmetric part of the "moment of inertia tensor" $T_{ij}(t)$.

5.2.4 The Pauli-matrix structure

In this subsection, we provide deeper understanding of the singular space-time structure observed in the previous subsections. Let us work in the SU(n) basis which diagonalizes $Q(t)$ at each time t with the ordering (5.2.2), and consider the 2×2 submatrix $X_i(t)$ in the bottom-right corner of

$$\bar{A}^{(i)}(t) = \begin{pmatrix} * & * \\ * & X_i(t) \end{pmatrix} \tag{5.2.8}$$

for the extended directions $i = 1, 2, 3$. Here we use the VDM model with the parameter sets given in table 5.1 and take the continuum limit focusing on the time $(t - t_c)/R(t_c) \approx 0.40$ as we did in section 5.2.3.

We show below that the three matrices X_i in (5.2.8) tend to satisfy the SU(2) Lie algebra

$$[X_i, X_j] = ic\epsilon_{ijk}X_k \tag{5.2.9}$$

for some real constant c in the continuum limit. In order to determine the optimal value of c, we consider a quantity

$$S(c) \equiv \mathrm{tr}(i\epsilon_{ijk}[X_i, X_j] + 2cX_k)^2 \ , \tag{5.2.10}$$

which represents the violation of the relation (5.2.9). The value of c that minimizes $S(c)$ can be readily obtained as

$$\tilde{c} = -\frac{i\epsilon_{ijk}\mathrm{tr}(X_k[X_i, X_j])}{2\mathrm{tr}(X_l^2)} \ . \tag{5.2.11}$$

Using $c = \tilde{c}$ as the optimal value for each configuration, we investigate to what extent the relation (5.2.9) is satisfied.

In Fig. 5.5, we show a scatter plot for the real part (Left) and the imaginary part (Right) of each side of (5.2.9). The quantities on both sides are normalized by $\mathrm{tr}(X_l^2)$ so that they become invariant under the scale transformation $X_i \mapsto \mathrm{const.}X_i$. We observe that the data points tend to converge to the line $y = x$ as one goes from the top to the bottom corresponding to decreasing the lattice spacing ϵ (See table 5.1.). This shows that the 2×2 matrices X_i $(i = 1, 2, 3)$ tend to satisfy (5.2.9) in the continuum limit.

Thus we conclude that the singular space-time structure observed for the matrix configurations generated by simulations is essentially associated with the Pauli matrices. The Pauli matrices may be regarded as the simplest matrix configuration that has SO(3) symmetry in the sense that their SO(3) rotation can be absorbed by an appropriate SU(N) transformation. Given the situation characterized by the two large eigenvalues of $Q(t)$, the appearance of the Pauli-matrix structure may not be that surprising.

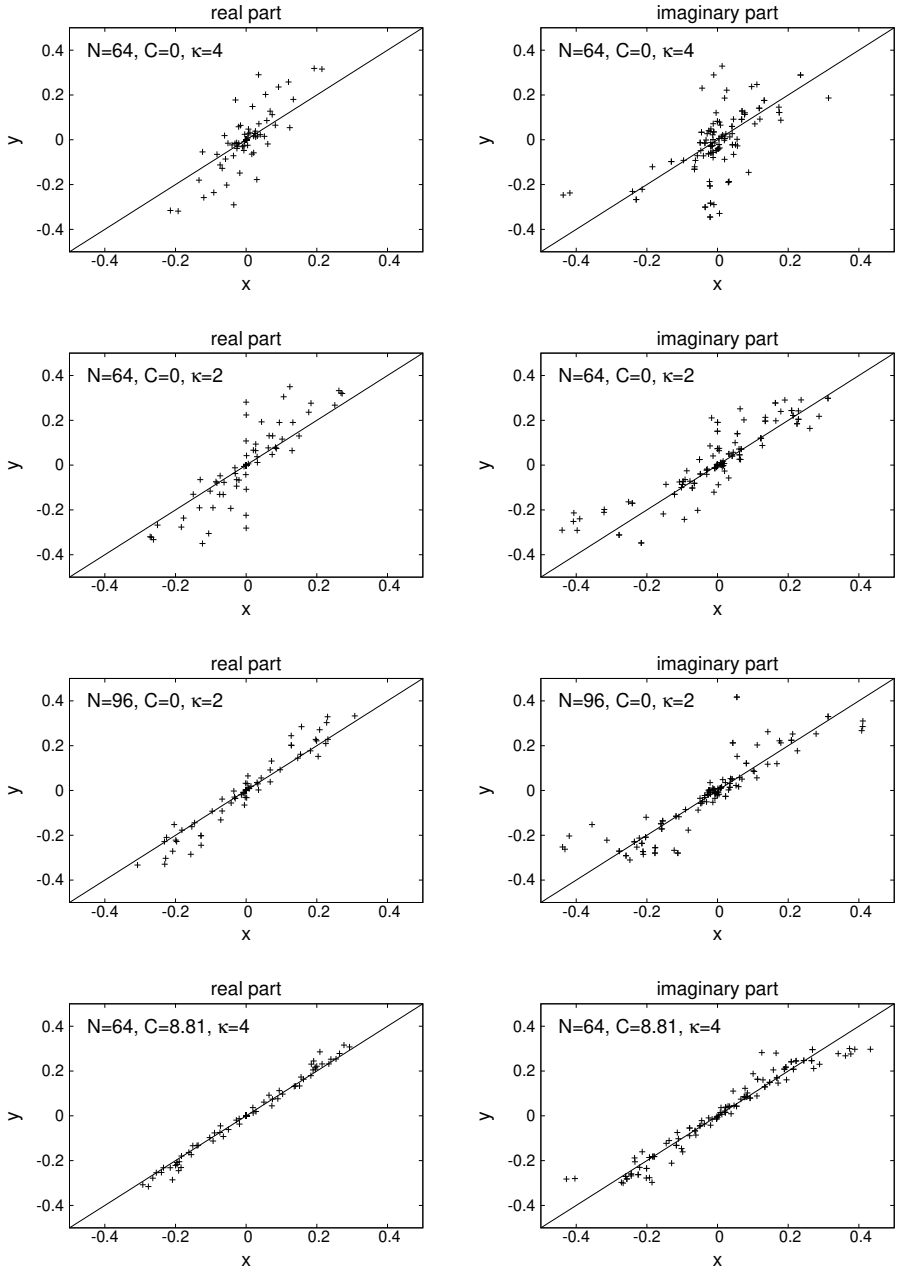

Figure 5.5: (Left) A scatter plot for the real part $x = \mathrm{Re}(i\tilde{c}\epsilon_{ijk}(X_k)_{ab})/\mathrm{tr}(X_l^2)$ and $y = \mathrm{Re}([X_i, X_j]_{ab})/\mathrm{tr}(X_l^2)$ of each side of (5.2.9) with (5.2.11) is shown for $(i, j) = (1, 2), (2, 3), (3, 1)$ and $(a, b) = (1, 1), (1, 2), (2, 2)$ using 10 configurations obtained by simulating the VDM model with the parameter sets given in table 5.1. The solid line represents $y = x$. (Right) A scatter plot for the imaginary part $x = \mathrm{Im}(i\tilde{c}\epsilon_{ijk}(X_k)_{ab})/\mathrm{tr}(X_l^2)$ and $y = \mathrm{Im}([X_i, X_j]_{ab})/\mathrm{tr}(X_l^2)$ of each side of (5.2.9) with (5.2.11) is shown in the same way.

5.3 The new interpretation of the simulation

In this section, we attribute the observed Pauli-matrix structure to the approximation involved in deriving the partition function (5.1.15), which was used in Monte Carlo simulation. We point out a subtlety in the approximation, and argue that the approximation amounts to replacing $\mathrm{e}^{iS_\mathrm{b}}$ by $\mathrm{e}^{\beta S_\mathrm{b}}$ in the original partition function (5.1.11). This new interpretation of the simulation provides us with a natural understanding of the (3+1)d expanding behavior with the Pauli-matrix structure discussed in section 5.2. We also speculate on a possible scenario for the original model with the correct $\mathrm{e}^{iS_\mathrm{b}}$ factor.

5.3.1 The "derivation" of the partition function (5.1.15)

Let us first review how one can obtain the partition function (5.1.15) used in Monte Carlo simulation from the original partition function (5.1.11). (This was done in Appendix A of ref. [88] for $p = 1$, but here we generalize it to arbitrary p.)

Note that the integrand of the partition function (5.1.11) involves a phase factor $\mathrm{e}^{iS_\mathrm{b}}$. As is commonly done in integrating oscillating functions, we introduce the convergence factor $\mathrm{e}^{-\epsilon|S_\mathrm{b}|}$ and take the $\epsilon \to 0$ limit after the integration.

The partition function can then be rewritten as

$$Z = \int dA \int_0^{L^{2p}} d(r^p)\, \delta\left(\frac{1}{N}\mathrm{Tr}\left\{(A_i)^2\right\}^p - r^p\right) \theta\left(\kappa^p r^p - \frac{1}{N}\mathrm{Tr}\,(A_0)^{2p}\right) \mathrm{e}^{iS_\mathrm{b} - \epsilon|S_\mathrm{b}|}\, \mathrm{Pf}\mathcal{M}\ , \tag{5.3.1}$$

where κ and L are the cutoff parameters introduced in (5.1.13) and (5.1.14), respectively. Rescaling the variables $A_\mu \mapsto r^{1/2} A_\mu$ in the integrand, we get

$$Z = \int dA\, \mathrm{Pf}\mathcal{M}(A)\, f(S_\mathrm{b})\, \delta\left(\frac{1}{N}\mathrm{Tr}\left\{(A_i)^2\right\}^p - 1\right) \theta\left(\kappa^p - \frac{1}{N}\mathrm{Tr}\,(A_0)^{2p}\right)\ . \tag{5.3.2}$$

Here we have defined the function $f(S_\mathrm{b})$ by

$$f(S_\mathrm{b}) \equiv \int_0^{L^{2p}} d(r^p)\, r^{9(N^2-1)-1} \mathrm{e}^{r^2(iS_\mathrm{b} - \epsilon|S_\mathrm{b}|)}\ , \tag{5.3.3}$$

which is a complex-valued function with the property $f(-S_\mathrm{b}) = f(S_\mathrm{b})^*$.

For $|S_\mathrm{b}| \ll \frac{1}{L^4}$, the function can be well approximated by

$$f(S_\mathrm{b}) \approx \frac{p}{9(N^2-1)+p-1}(L^2)^{9(N^2-1)+p-1}\ . \tag{5.3.4}$$

For $|S_\mathrm{b}| \gtrsim \frac{1}{L^4}$, on the other hand, the phase of the integrand in (5.3.3) starts to oscillate violently in the region $r \gtrsim 1/\sqrt{|S_\mathrm{b}|}$, and hence the integral decreases rapidly in magnitude for increasing $|S_\mathrm{b}|$. In particular, the asymptotic behavior of $f(S_\mathrm{b})$ for $S_\mathrm{b} \gg \frac{1}{L^4}$ can be estimated as

$$\frac{|f(S_\mathrm{b})|}{f(0)} = \Gamma\left(\frac{9(N^2-1)+p+1}{2}\right)\left(\frac{1}{L^4|S_\mathrm{b}|}\right)^{\frac{9(N^2-1)+p-1}{2}} + O(\mathrm{e}^{-\epsilon L^4|S_\mathrm{b}|}) \tag{5.3.5}$$

by deforming the integration contour in (5.3.3).

Recalling eq. (5.1.12), the condition $|S_{\rm b}| \ll \frac{1}{L^4}$ for (5.3.4) can be rewritten as

$$\left| \frac{1}{N} \mathrm{Tr} \left(F_{\mu\nu} F^{\mu\nu} \right) \right| \ll \frac{4}{NL^4} \ . \tag{5.3.6}$$

Therefore, assuming that the right-hand side $\frac{4}{NL^4}$ of (5.3.6) becomes small at large N, we may make a replacement

$$f(S_{\rm b}) \Longrightarrow \delta \left(\frac{1}{N} \mathrm{Tr} \left(F_{\mu\nu} F^{\mu\nu} \right) \right) \tag{5.3.7}$$

up to a normalization constant. For the bosonic model and the VDM model, one simply has to replace the Pfaffian in (5.3.1) and (5.3.2) as (5.1.23).

5.3.2 Subtlety in the derivation and the new interpretation

The only step in the derivation that may go wrong is the replacement (5.3.7). The subtlety in this replacement can be seen as follows. Note that the phase factor $\mathrm{e}^{iS_{\rm b}}$ in the partition function (5.1.11) favors configurations at which the bosonic action $S_{\rm b}$ is stationary. On the other hand, the above approximation essentially replaces the phase factor $\mathrm{e}^{iS_{\rm b}}$ by the delta function $\delta(S_{\rm b})$, which amounts to picking up configurations at which $S_{\rm b}$ is stationary only under rescaling $A_\mu \mapsto \mathrm{const.} A_\mu$. While it is true that $|f(S_{\rm b})|$ is sharply peaked at $S_{\rm b} = 0$, the function $f(S_{\rm b})$ is actually a complex-valued function, whose phase rotates violently around $S_{\rm b} = 0$. This effect of the phase should be responsible for favoring the configurations at which $S_{\rm b}$ is stationary. The approximation ignores this effect completely, and hence it cannot be justified.

If the model (5.1.15) is not equivalent to the original model (5.1.11), what kind of model does it actually correspond to? Here we point out that the constraint on $S_{\rm b}$ that appears in (5.1.15) may be regarded as the constraint one uses in defining a microcanonical ensemble. From this viewpoint, we consider that the model (5.1.15) is actually equivalent to the corresponding canonical ensemble with the Boltzmann weight $\mathrm{e}^{\beta S_{\rm b}}$. The real parameter β depends on the parameter C in the constraint[5]. As we will see below, we consider that the model (5.1.15) corresponds essentially to replacing $\mathrm{e}^{iS_{\rm b}}$ by $\mathrm{e}^{\beta S_{\rm b}}$ with $\beta > 0$.

For $\beta > 0$, the first term in (5.1.12) that appears in $\mathrm{e}^{\beta S_{\rm b}}$ favors configurations in which A_0 and A_i commute. This means that the spatial matrices A_i tend to become diagonal in the SU(N) basis which diagonalizes A_0. On the other hand, the second term in (5.1.12) favors configurations in which the noncommutativity among the spatial matrices A_i is large. The band-diagonal structure, which plays a crucial role in extracting the real-time

[5]This connection also provides clear justification of the renormalization-group-like method [88, 89], which amounts to tuning the parameter C in order to obtain the late-time behaviors with smaller matrix size.

evolution as in section 5.1.2, can be understood as a consequence of the balance of these two effects.

We can also understand the reason for the (3+1)d expanding behavior with the Pauli-matrix structure. Here we assume that the first term in (5.1.12) is not important except in realizing the band-diagonal structure and focus on the effect of the second term in (5.1.12), which favors large $\mathrm{Tr}\,(F_{ij})^2$, where $F_{ij} = i\,[A_i, A_j]$. We also have to take into account the constraint $\frac{1}{N}\mathrm{Tr}\left\{(A_i)^2\right\}^p = 1$, where we set $p = 1$ in what follows.

Simplifying the band-diagonal structure of the spatial matrices A_i $(i = 1, \cdots, 9)$, we consider the block-diagonal structure given as

$$A_i = \begin{pmatrix} \bar{A}_i^{(1)} & & & \\ & \bar{A}_i^{(2)} & & \\ & & \ddots & \\ & & & \bar{A}_i^{(B)} \end{pmatrix} , \tag{5.3.8}$$

where n is the common block size and B is the number of blocks satisfying $N = nB$. Within this ansatz, we would like to maximize $\mathrm{Tr}\,(F_{ij})^2$ under the constraint $\frac{1}{N}\mathrm{Tr}\,(A_i)^2 = 1$. Note that we have

$$\frac{1}{N}\mathrm{Tr}\,(A_i)^2 = \frac{1}{B}\sum_{b=1}^{B}\frac{1}{n}\mathrm{Tr}\,(\bar{A}_i^{(b)})^2 , \tag{5.3.9}$$

$$\frac{1}{N}\mathrm{Tr}\,(F_{ij})^2 = \frac{1}{B}\sum_{b=1}^{B}\frac{1}{n}\mathrm{Tr}\,(\bar{F}_{ij}^{(b)})^2 , \tag{5.3.10}$$

where we have defined $\bar{F}_{ij}^{(b)} = i[\bar{A}_i^{(b)}, \bar{A}_j^{(b)}]$ for each block b.

Let us solve the maximization problem in two steps. First we fix

$$\frac{1}{n}\mathrm{Tr}\,(\bar{A}_i^{(b)})^2 = (r_b)^2 , \tag{5.3.11}$$

$$\frac{1}{B}\sum_{b=1}^{B}(r_b)^2 = 1 , \tag{5.3.12}$$

and maximize $\mathrm{Tr}\,(F_{ij})^2$ under this constraint. Following the discussion given in ref. [60], the solution to this first maximization problem can be written in terms of the Pauli matrices σ_i as

$$\bar{A}_i^{(b)} = \frac{1}{\sqrt{6}} r_b(\sigma_i \oplus \mathbf{0}_{n-2}) , \tag{5.3.13}$$

for $i = 1, 2, 3$ and $\bar{A}_i^{(b)} = 0$ otherwise, up to the symmetries of the problem such as the SO(9) rotational symmetry and the SU(n) symmetry within each block. The value of $\mathrm{Tr}\,(F_{ij})^2$ for (5.3.13) is given as

$$\mathrm{Tr}\,(F_{ij})^2 = \frac{2}{3}\sum_{b=1}^{B}(r_b)^4 . \tag{5.3.14}$$

As the second step of the maximization, we maximize (5.3.14) under the constraint (5.3.12). The maximum is given when all but one of the r_b's are zero.

In reality, one should also take into account the entropic factor due to quantum fluctuations, which is expected to favor certain distribution of r_b. Due to the time-reversal symmetry $A_0 \mapsto -A_0$ of the model, the most natural distribution would be that r_b is large around $t = 0$ and decreases with $|t|$. Thus we can understand the appearance of the (3+1)d expanding behavior with the Pauli-matrix structure.

Chapter 6

Complex Langevin simulation of the Lorentzian type IIB matrix model

We use the CLM to overcome the sign problem instead of the approximation which was used so far. Since the sign problem is severe for the Lorentzian model, we generalize the model by introducing two parameters which are related to the Wick rotation on the world sheet and that in the target space. We apply the CLM to the generalized model.

6.1 Generalization of the model

The partition function of the generalized model is given by

$$Z = \int dAd\psi e^{-\tilde{S}} \ \delta\left(\frac{1}{N}\mathrm{Tr}\,(A_0)^2 - \kappa\right) \ \delta\left(\frac{1}{N}\mathrm{Tr}\,(A_i)^2 - 1\right), \tag{6.1.1}$$

$$\tilde{S} = \tilde{S}_{\mathrm{b}} + \tilde{S}_{\mathrm{f}}, \tag{6.1.2}$$

where $\beta = 1/(g^2 N)$. $\tilde{S}_{\mathrm{b}}$ and $\tilde{S}_{\mathrm{f}}$ are the bosonic and fermionic part of the action respectively. The bosonic part and the fermionic part are defined as

$$\begin{aligned} \tilde{S}_{\mathrm{b}} &= -iN\beta e^{is\pi/2}\left(-\frac{1}{2}e^{-ik\pi}\mathrm{Tr}\,(F_{0i})^2 + \frac{1}{4}\mathrm{Tr}\,(F_{ij})^2\right), \\ \tilde{S}_{\mathrm{f}} &= -iN\beta e^{is\pi/2}\left(-\frac{1}{2}e^{-ik\pi/2}\bar{\psi}\Gamma^0[A_0,\psi] + \frac{1}{2}\bar{\psi}\Gamma^i[A_i,\psi]\right), \end{aligned} \tag{6.1.3}$$

where $F_{\mu\nu} = i[A_\mu, A_\nu]$, $e^{is\pi/2}$ comes from the Wick rotation on the world sheet, and $e^{-ik\pi/2}$ comes from the Wick rotation in the target space as $A_0 \to e^{-ik\pi/2}A_0$.

After the path integration for the fermionic matrices, the partition function is rewritten as

$$\begin{aligned} Z &= \int dAd\psi e^{-\tilde{S}_{\mathrm{eff}}} \ \delta\left(\frac{1}{N}\mathrm{Tr}\,(A_0)^2 - \kappa\right) \ \delta\left(\frac{1}{N}\mathrm{Tr}\,(A_i)^2 - 1\right), \\ \tilde{S}_{\mathrm{eff}} &= -iN\beta e^{is\pi/2}\tilde{S}_{\mathrm{b}} - \log \mathrm{Pf}\mathcal{M}(e^{-ik\pi/2}A_0, A_i), \end{aligned} \tag{6.1.4}$$

where $\mathcal{M}(e^{-ik\pi/2}A_0, A_i)$ is the Dirac operator which acts on the fermionic matrices ψ. The Pfaffian Pf$\mathcal{M}$ is complex in general.

The Lorentzian model corresponds to setting $(s,k) = (0,0)$, whereas the Euclidean model corresponds to setting $(s,k) = (1,1)$. Note that the approximation (5.3.7) corresponds to setting $(s,k) = (-1,0)$ where the sign problem is absent.

6.2 Complex Langevin simulation of the model

In the CLM, since it is difficult to impose the cutoffs by using the usual way, we choose an alternative way to impose the cutoffs which are explained in 6.2.1. In our simulations, we choose an SU(N) basis as (5.1.16) which diagonalizes the temporal matrix. Therefore, in 6.2.2, we explain how to realize the order of diagonal elements of the temporal matrix in the simulations. At the end of this section 6.2.3, we explain the application of CLM to the generalized model.

6.2.1 Treatment of the cutoffs

In the previous works, quadratic functions are used to impose two cutoffs as

$$\begin{aligned} \delta\left(\frac{1}{N}\mathrm{Tr}\,(A_0)^2 - \kappa\right)\,\delta\left(\frac{1}{N}\mathrm{Tr}\,(A_i)^2 - 1\right) &\to e^{-S_{\mathrm{pot}}}, \\ S_{\mathrm{pot}} = \frac{1}{2}c_{\mathrm{s}}(\frac{1}{N}\mathrm{Tr}\,(A_0)^2 - \kappa)^2 &+ \frac{1}{2}c_{\mathrm{t}}(\frac{1}{N}\mathrm{Tr}\,(A_i)^2 - 1)^2, \end{aligned} \tag{6.2.1}$$

where c_{s} and c_{t} are the some constants. In order to impose the cutoffs correctly, we need to use very large coefficients for the quadratic functions. However, these very large coefficients sometimes cause very large drift terms. If these large drifts appear frequently in the complex Langevin simulations, the criterion for the correct convergence is not satisfied. Therefore, we treat the cutoffs by using another way.

Actually, by the change of variables, we can impose the cutoffs correctly. First, we introduce two auxiliary variables u and v, and rewrite the partition function as

$$\begin{aligned} Z = \int_0^\infty dudv \int dAd\psi u^p v^q e^{-f(u)-g(v)} e^{-\tilde{S}_{\mathrm{eff}}(A_0,A_i)} \\ \times \delta\left(\frac{1}{N}\mathrm{Tr}\,(A_0)^2 - \kappa\right)\,\delta\left(\frac{1}{N}\mathrm{Tr}\,(A_i)^2 - 1\right), \end{aligned} \tag{6.2.2}$$

where p and q are some positive constants, and $f(u)$ and $g(v)$ should be chosen so that the integrations for u and v converge.

Next, we make a change the variables as

$$X_0 = \sqrt{\frac{u}{\kappa}}A_0, \quad X_i = \sqrt{v}A_i. \tag{6.2.3}$$

The measure becomes

$$dX = \left(\frac{u}{\kappa}\right)^{\frac{1}{2}N^2} v^{\frac{1}{2}(D-1)N^2} dA, \tag{6.2.4}$$

and the constraints become

$$\begin{aligned} \delta\left(\frac{1}{N}\mathrm{Tr}\,(A_0)^2 - \kappa\right) &= \frac{u}{\kappa}\ \delta\left(\frac{1}{N}\mathrm{Tr}\,(X_0)^2 - u\right), \\ \delta\left(\frac{1}{N}\mathrm{Tr}\,(A_i)^2 - 1\right) &= v\ \delta\left(\frac{1}{N}\mathrm{Tr}\,(X_i)^2 - v\right). \end{aligned} \tag{6.2.5}$$

When we choose $p = \frac{1}{2}N^2 - 1$ and $q = \frac{1}{2}(D-1)N^2 - 1$ the exponents of u and v vanish. Therefore the partition function becomes

$$\begin{aligned} Z = \int_0^\infty du dv \int dX d\psi \kappa^{\frac{1}{2}N^2-1} e^{-f(u)-g(v)} e^{-\tilde{S}_{\mathrm{eff}}(\sqrt{\kappa/u}X_0, \sqrt{1/v}X_i)} \\ \times \delta\left(\frac{1}{N}\mathrm{Tr}\,(X_0)^2 - u\right)\ \delta\left(\frac{1}{N}\mathrm{Tr}\,(X_i)^2 - v\right). \end{aligned} \tag{6.2.6}$$

After Integrations of u and v, we obtain

$$\begin{aligned} Z &= \int dX d\psi e^{-S}, \\ S &= \tilde{S}\left(\frac{\sqrt{\kappa}X_0}{\sqrt{\frac{1}{N}\mathrm{Tr}\,(X_0)^2}}, \frac{X_i}{\sqrt{\frac{1}{N}\mathrm{Tr}\,(X_i)^2}}\right) + f\left(\frac{1}{N}\mathrm{Tr}\,(X_0)^2\right) + g\left(\frac{1}{N}\mathrm{Tr}\,(X_i)^2\right) \end{aligned} \tag{6.2.7}$$

where we neglect an irrelevant overall factor. In this work, we choose $f(x) = g(x) = \frac{1}{2}N^2 x$ because we can obtain the analytic results for this choice. We will show the analytic results later.

6.2.2 A way to realize the order of diagonal elements of the temporal matrix.

We use SU(N) symmetry to diagonalize the temporal matrix X_0 as

$$X_0 = \mathrm{diag}(x_1, x_2, ..., x_N), \text{ where } x_1 < x_2 < \cdots < x_N. \tag{6.2.8}$$

By using "the gauge fixing", we can rewrite the partition function as

$$\begin{aligned} Z &= \int \prod_{a=1}^{N} dx_a \Delta(x)^2 \int dA_i e^{-S}, \\ \Delta(x) &= \prod_{a>b}^{N} (x_a - x_b), \end{aligned} \tag{6.2.9}$$

where $\Delta(x)$ is the van der Monde determinant.

In order to to realize the order (6.2.8), we use a method which is proposed in [90]. We perform the change of variable by introducing new variables τ_a as

$$x_1 = 0,\ x_2 = e^{\tau_1},\ x_3 = e^{\tau_1} + e^{\tau_2},\ ...,\ x_N = \sum_{a=1}^{N-1} e^{\tau_a}, \tag{6.2.10}$$

where we use the shift symmetry[1] to setting $x_1 = 0$. By treating the τ_a as dynamical variables, the order of the diagonal elements of X_0 is automatically realized. The effective action becomes

$$\begin{aligned} S_{\text{eff}} = N\beta e^{-i\frac{\pi}{2}(1-s)} &\left\{ \frac{1}{2} e^{-ik\pi} \frac{\kappa \operatorname{Tr}\left[X_0, X_i\right]^2}{\frac{1}{N}\operatorname{Tr}\left(\tilde{X}_0\right)^2 \frac{1}{N}\operatorname{Tr}\left(X_i\right)^2} - \frac{1}{4} \frac{\operatorname{Tr}\left[X_i, X_j\right]^2}{\left(\frac{1}{N}\operatorname{Tr}\left(X_i\right)^2\right)^2} \right\} \\ &+ \frac{1}{2} N \operatorname{Tr}\left(\tilde{X}_0\right)^2 + \frac{1}{2} N \operatorname{Tr}\left(X_i\right)^2 - 2\log\Delta(x) - \sum_{a=1}^{N-1} \tau_a, \end{aligned} \tag{6.2.11}$$

where the last term comes from the change of the variables (6.2.10), and $\tilde{X}_0 = X_0 - \frac{1}{N}\operatorname{Tr}\left(X_0\right)$. We can obtain the exact results for X_0 and X_i as

$$\begin{aligned} \left\langle \frac{1}{N} \operatorname{Tr}\left(\tilde{X}_0\right)^2 \right\rangle &= 1 - \frac{1}{N^2}, \\ \left\langle \frac{1}{N} \operatorname{Tr}\left(X_i\right)^2 \right\rangle &= D - 1. \end{aligned} \tag{6.2.12}$$

These analytic results can be used as a validity check for complex Langevin simulations.

When we calculate observables, we should use A_μ which are obtained from X_μ by rescaling as

$$A_0 = \frac{\sqrt{\kappa}\tilde{X}_0}{\sqrt{\frac{1}{N}\operatorname{Tr}\left(\tilde{X}_0\right)^2}}, \qquad A_i = \frac{X_i}{\sqrt{\frac{1}{N}\operatorname{Tr}\left(X_i\right)^2}}. \tag{6.2.13}$$

6.2.3 Application of the CLM

First of all we extend the degrees of freedom of the dynamical variables which correspond to $X_i \in \mathrm{SU}(N) \to \mathcal{X}_i \in \mathrm{SL}(N, \mathbb{C})$ and $\tau_a \in \mathbb{R} \to \tau_a \in \mathbb{C}$. These variables are updated by the following complex Langevin equations:

$$\begin{aligned} \frac{d\tau_a}{dt_{\mathrm{L}}} &= -\frac{\partial S_{\text{eff}}}{\partial \tau_a} + \eta_a(t_{\mathrm{L}}), \\ \frac{d(X_i)_{ab}}{dt_{\mathrm{L}}} &= -\frac{\partial S_{\text{eff}}}{\partial (X_i)_{ba}} + (\eta_i)_{ab}(t_{\mathrm{L}}), \end{aligned} \tag{6.2.14}$$

where t_{L} is a fictitious time for the Langevin simulations, and η are Gaussian noises. The drift terms $\frac{\partial S_{\text{eff}}}{\partial \tau_a}$ and $\frac{\partial S_{\text{eff}}}{\partial (X_i)_{ba}}$ are defined first for the real variables τ_a and the Hermitian

[1]The action (6.1.2) is invariant under the shift of A_0: $A_0 \to A_0 + c\mathbb{1}$, where $c \in \mathbb{R}$ is some constant.

matrices X_i, and then it is defined for the complexified variables τ_a and $\mathcal{X}_i$ by analytic continuation in order to respect holomorphicity.

The drift terms are given explicitly as

$$\begin{aligned}
\frac{\partial S_{\text{eff}}}{\partial \tau_a} =& \beta e^{-i\frac{\pi}{2}(1-s)} e^{-ik\pi} \frac{\kappa}{L} e^{\tau_a} \\
& \left\{ -\frac{2N}{K} \sum_{b=a+1}^{N} \sum_{c \neq b} (x_b - x_c) (X_i)_{bc} (X_i)_{cb} \right. \\
& \left. + \frac{1}{K^2} \sum_{b=a+1}^{N} \left(x_b - \frac{1}{N} \sum_c x_c \right) \sum_{de} (x_d - x_e)^2 (X_i)_{de} (X_i)_{ed} \right\} \\
& - e^{\tau_a} \sum_{b=a+1}^{N} \sum_{c \neq b} \frac{2}{x_b - x_c} - 1 + N e^{\tau_a} \sum_{b=a+1}^{N} \left(x_b - \frac{1}{N} \sum_c x_c \right),
\end{aligned} \tag{6.2.15}$$

$$\begin{aligned}
\frac{\partial S_{\text{eff}}}{\partial (X_i)_{ba}} =& - \beta e^{-i\frac{\pi}{2}(1-s)} e^{-ik\pi} \frac{\kappa}{K} \\
& \left\{ \frac{N}{L} [X_0, [X_0, X_i]]_{ab} + \frac{\text{Tr}\,[X_0, X_j]^2}{L^2} (X_i)_{ab} \right\} \\
& + \beta e^{-i\frac{\pi}{2}(1-s)} \left\{ \frac{N [X_j, [X_j, X_i]]_{ab}}{L^2} + \frac{\text{Tr}\,[X_j, X_k]^2}{L^3} (X_i)_{ab} \right\} \\
& + N (X_i)_{ab},
\end{aligned} \tag{6.2.16}$$

where we define

$$K = \frac{1}{N} \text{Tr}\,(\tilde{X}_0)^2 = \frac{1}{N} \sum_{a=1}^{N} (x_a)^2 - \left(\frac{1}{N} \sum_{a=1}^{N} x_a \right)^2, \tag{6.2.17}$$

$$L = \frac{1}{N} \text{Tr}\,(X_i)^2. \tag{6.2.18}$$

6.2.4 Hermiticity of the extended matrices

In the simulations, we calculate a quantity that measures how the extended matrices $\mathcal{X}_i$ are far from Hermitian matrices as an indication for the excursion problem. Here, we define the Hermiticity norm as

$$H = \frac{-\text{Tr}\,(\mathcal{X}_i - \mathcal{X}_i^\dagger)^2}{4\text{Tr}\,(\mathcal{X}_i^\dagger \mathcal{X}_i)}, \tag{6.2.19}$$

whose lower bound is 0 and the upper bound is 1. This quantity becomes 0 for Hermitian matrices and 1 for anti-Hermitian matrices. Note that, in our simulation, since we fix the gauge to diagonalize X_0, we cannot use the gauge cooling technique.

6.2.5 Adaptive step size

In order to avoid the excursion problem, we use the adaptive step size algorithm in the simulations. We modify the Langevin step size depending on the magnitude for drift terms as

$$\Delta t = \begin{cases} \Delta t_0 & \text{for } u < v_0 \ , \\ \dfrac{v_0}{u}\Delta t_0 & \text{otherwise} \ , \end{cases} \tag{6.2.20}$$

where Δt_0 is a default step size, v_0 is a threshold for the algorithm, and u is defined as

$$\begin{aligned} u &= \max\left(u_\tau, u_{\rm s}\right), \\ u_\tau &= \sqrt{\frac{1}{N^3}\sum_{a=1}^{N-1}\left|\frac{\partial S_{\rm eff}}{\partial \tau_a}\right|^2}, \\ u_{\rm s} &= \sqrt{\frac{1}{N^3(D-1)}\sum_{i=1}^{D-1}\sum_{a=1}^{N}\sum_{b=1}^{N}\left|\frac{\partial S_{\rm eff}}{\partial (\mathcal{X}_i)_{ab}}\right|^2}. \end{aligned} \tag{6.2.21}$$

In this work, we set $v_0 = 10$ because we found that the typical value is $\mathcal{O}(1)$.

6.3 Results

In this section, we will show the results for a simplified model and the original model. Note that the observables which we will show later are snapshots obtained by the final configuration for each simulation.

6.3.1 Results for the 10D bosonic model

Here, we study the bosonic model, which is a simplified model obtained by omitting the fermionic part $\tilde{S}_{\rm f}$ from the action (6.1.2). In the simulations for the bosonic model, we use the 2nd-order RK algorithm to reduce the finite step size effects.

First we set $k = 0$ which means that the signature in the target space is the Lorentzian. We find that the complex Langevin simulations starting from the Pauli-matrix configurations which are obtained at $s = -1$ seem to be unstable at $s \neq -1$. In Fig. 6.1, we plot the results for $N = 32$ case. The Hermiticity norm gradually increases and finally reaches 0.5. In this case, the drift histogram has a long tail, which means that the criterion for the correct convergence of the CLM is not satisfied. In Fig. 6.2, we plot the results for $N = 256$ case. Although the Hermiticity norm has not reached 0.5 so far, the norm is gradually increasing. Moreover, there is no tendency for the norm to be stable at some small value which is less than 0.5. It is possible that if one continues the simulation for a long time, the norm finally reaches 0.5. Therefore, we expect that this simulation is unstable.

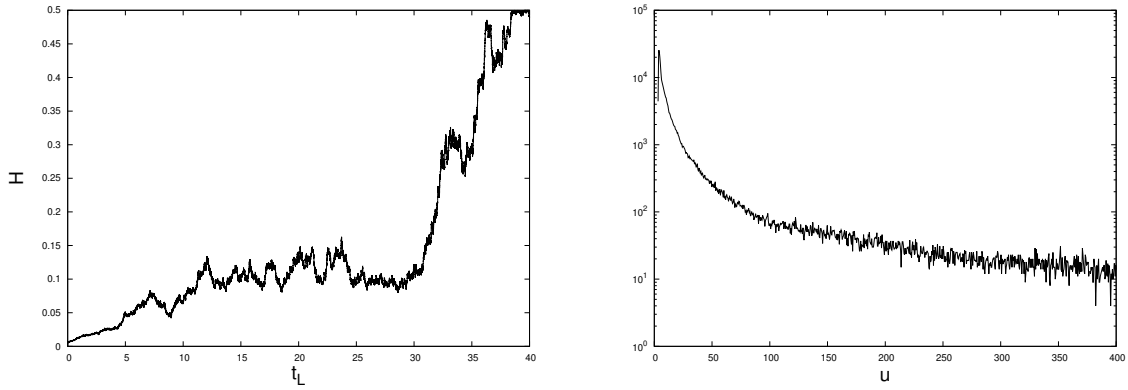

Figure 6.1: We plot the results for the bosonic model with $N = 32$, $\beta = 2.5$, $\kappa = 0.4$ and $(s, k) = (-0.8, 0)$. The simulation starts from the Pauli-matrix configuration which is obtained from a simulation at $(s, k) = (-1, 0)$ with the same parameter setting. (Left) A Hermiticity norm is plotted against the Langevin time. The norm gradually increases and finally reaches 0.5. (Right) We plot a histogram of the drift terms. We can see a long tail in the histogram.

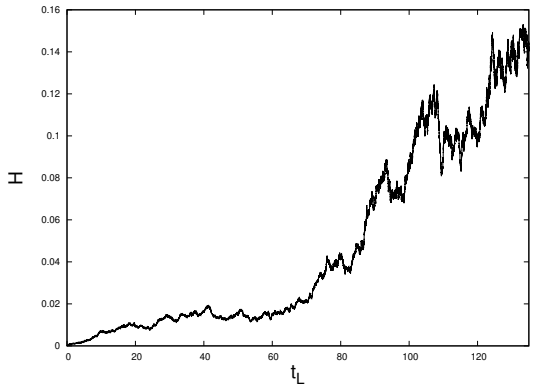

Figure 6.2: We plot the results for the bosonic model with $N = 256$, $\beta = 2.5$, $\kappa = 1.0$ and $(s, k) = (-0.8, 0)$. The simulation starts from the Pauli-matrix configuration which is obtained from a simulation at $(s, k) = (-1, 0)$ with the same parameter setting. A Hermiticity norm is plotted against the Langevin time. We cannot see a tendency for the norm to be stable at some small value which is less than 0.5.

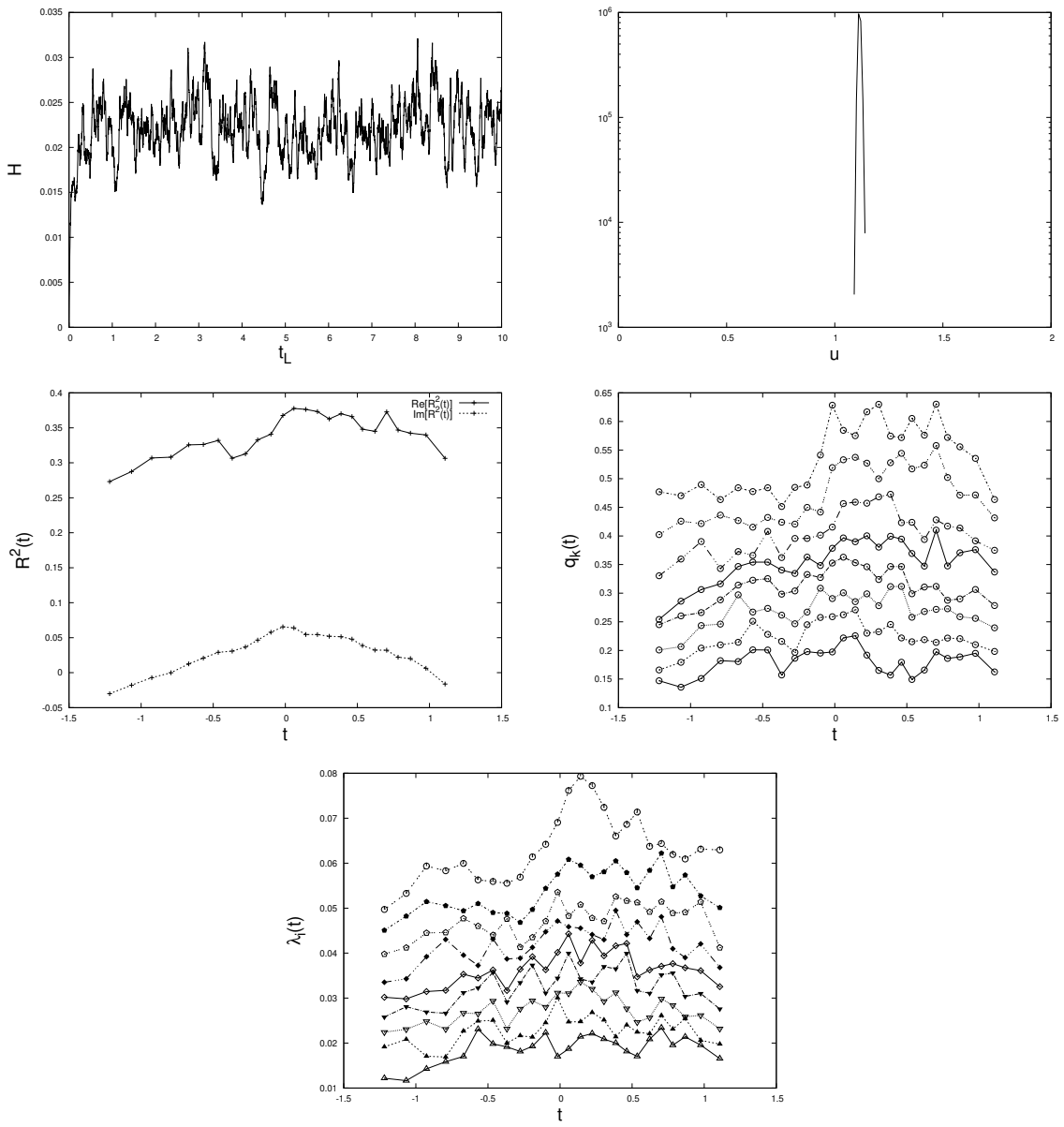

Figure 6.3: We plot the results for the bosonic model with $N = 32$, $\beta = 2.5$, $\kappa = 0.8$ and $(s, k) = (-0.8, 0)$. (Top-Left) A history of the Hermiticity norm where the horizontal axis is the Langevin time. The Hermiticity seems to be controlled. (Top-Right) A histogram of the drift term. This histogram falls off faster than exponential which means the criterion for the correct convergence is satisfied. (Middle-Left) We plot the real and imaginary part of $R^2(t)$ against the time. (Middle-Right) The eigenvalues of $Q(t)$ are plotted against time. This plot shows that the space is continuous. (Bottom) We plot the eigenvalues of $T_{ij}(t)$ which shows that there is no SSB of SO(9).

On the other hand, when simulations start from scratch at $s = -0.8$, the CLM works well. In Fig. 6.3 (Top-Left), we plot a history of the Hermiticity norm which is stable for a long time at a small value. Therefore, the excursion problem does not occur in this simulation. In Fig. 6.3 (Top-Right), we plot the histogram of the drift terms which falls off very quickly. This means that the criterion for correct convergence is satisfied. We show the extent of space $R^2(t)$ whose definition is (5.1.19) in Fig. 6.3 (Middle-Left). The space slightly expands as time proceeds. In Fig. 6.3 (Middle-Right) and (Bottom), we also show the eigenvalues of the moment of inertia tensor $T_{ij}(t)$ defined by (5.1.20) and the eigenvalus of $Q(t)$ defined by (5.2.1). When we calculate $T_{ij}(t)$ and $Q(t)$, instead of $\bar{\mathcal{A}}_i(t)$, we use Hermitian matrices $\bar{A}_i^{\mathrm{Herm}}(t)$ which are defined as

$$\bar{A}_i^{\mathrm{Herm}}(t) = \frac{1}{2}\left(\bar{\mathcal{A}}_i(t) + \bar{\mathcal{A}}_i^{\dagger}(t)\right), \tag{6.3.1}$$

where $\mathcal{A}_i$ are obtained by rescaling $\mathcal{X}_i$ as (6.2.13), and $\bar{\mathcal{A}}_i(t)$ is the block matrices defined like (5.1.17). Since the Hermiticity norm is very small, using these Hermitian matrices is a good approximation. The spectrum for the eigenvalues of $Q(t)$ looks very continuous, therefore the space continuously spreads in the radial direction. However, the 9 eigenvalues of $T_{ij}(t)$ are almost the same value, therefore the SO(9) symmetry is preserved. We also found that this new phase appears at $N = 128$ (see Fig. 6.4).

We increase s to approach the Lorentzian model. In Fig. 6.5, we show the results for various values of s. We found that the CLM works well even at the Lorentzian model. We also found that the shape of $R^2(t)$ changes from a bell-shaped curve to a parabola like curve which we have seen in the classical solutions [91]. In Fig. 6.6, we plots the results of the $s = 0$ case. At least, in this parameter choice ($\beta = 2.5$ and $\kappa = 0.8$), we cannot see the SSB of SO(9) even if we reach the Lorentzian model.

It is possible that the reason for no SSB of the SO(9) is the parameter choice for β and κ. When we decrease β or κ, although the criterion for correct convergence is satisfied, the SSB does not occur. Therefore, we try to increase β or κ at $N = 128$. However, in the large β or the large κ region, the criterion is not satisfied.

This no SSB behavior reminds us of results for the Euclidean bosonic model case in which there is no SSB of SO(10) [59]. Therefore, we study whether this new phase is smoothly connected to $(s, k) = (1, 1)$ which corresponds to the Euclidean model with the constraints[2].

In Fig. 6.7 and Fig. 6.8, we plot the results at $k = s$ line which lineally connects the Lorentzian case and the Euclidean case. We find that there are no qualitative differences between them. Therefore this new phase which we found at $(s, k) = (0, 0)$ is smoothly connected to the Euclidean case.

[2]Actually, the Euclidean model is well defined without the cutoffs. Therefore, strictly speaking, the generalized model at $(s, k) = (1, 1)$ is not the Euclidean type IIB matrix model.

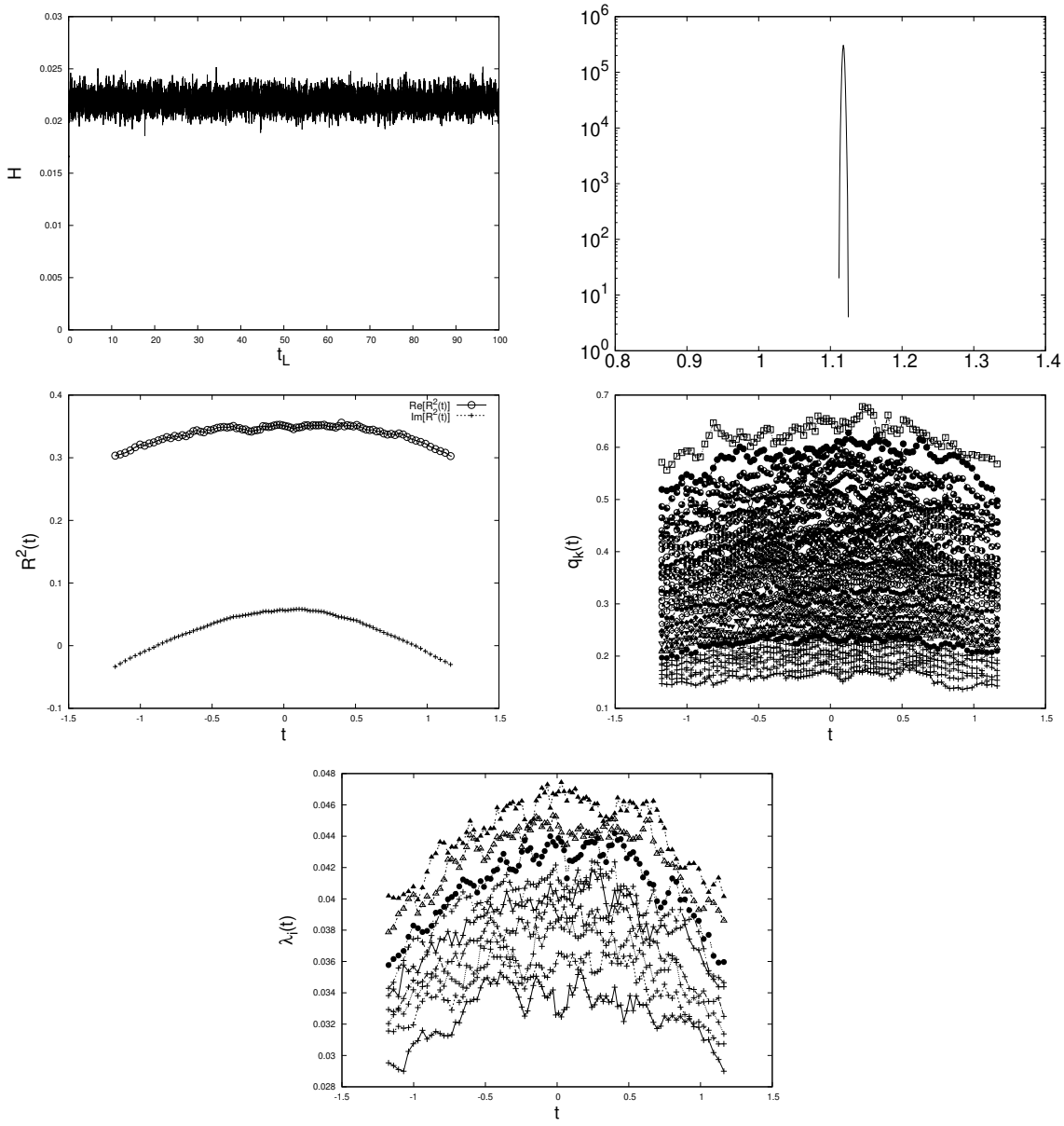

Figure 6.4: We plot the results for the bosonic model with $N = 128$, $\beta = 2.5$, $\kappa = 0.8$ and $(s, k) = (-0.8, 0)$. (Top-Left) The history of the Hermiticity norm where the horizontal axis is the Langevin time. The Hermiticity seems to be controlled. (Top-Right) The histogram of the drift term. This histogram falls off faster than exponential which means the criterion for the correct convergence is satisfied. (Middle-Left) We plot the real and imaginary part of $R^2(t)$ against the time. There is a little expansion. (Middle-Right) The eigenvalues of $Q(t)$ are plotted against time. This plot shows that the space is continuous. (Bottom) We plot the eigenvalues of $T_{ij}(t)$ which shows that there is no SSB of SO(9).

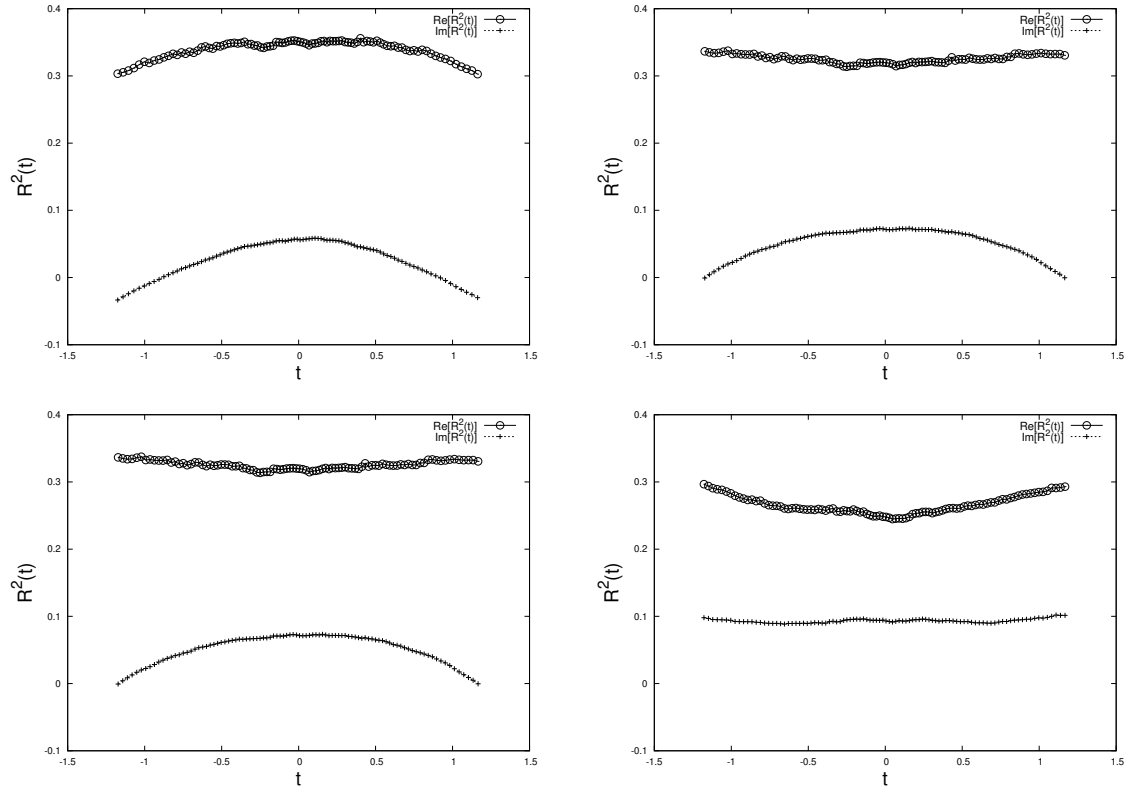

Figure 6.5: We plot the $R^2(t)$ against time for the bosonic model with $N = 128$, $\beta = 2.5$, $\kappa = 0.8$, and $k = 0$. (Top-Left), (Top-right), (Bottom-Left), and (Bottom-right) correspond to $s = -0.8, -0.6, -0.4,$ and 0 respectively.

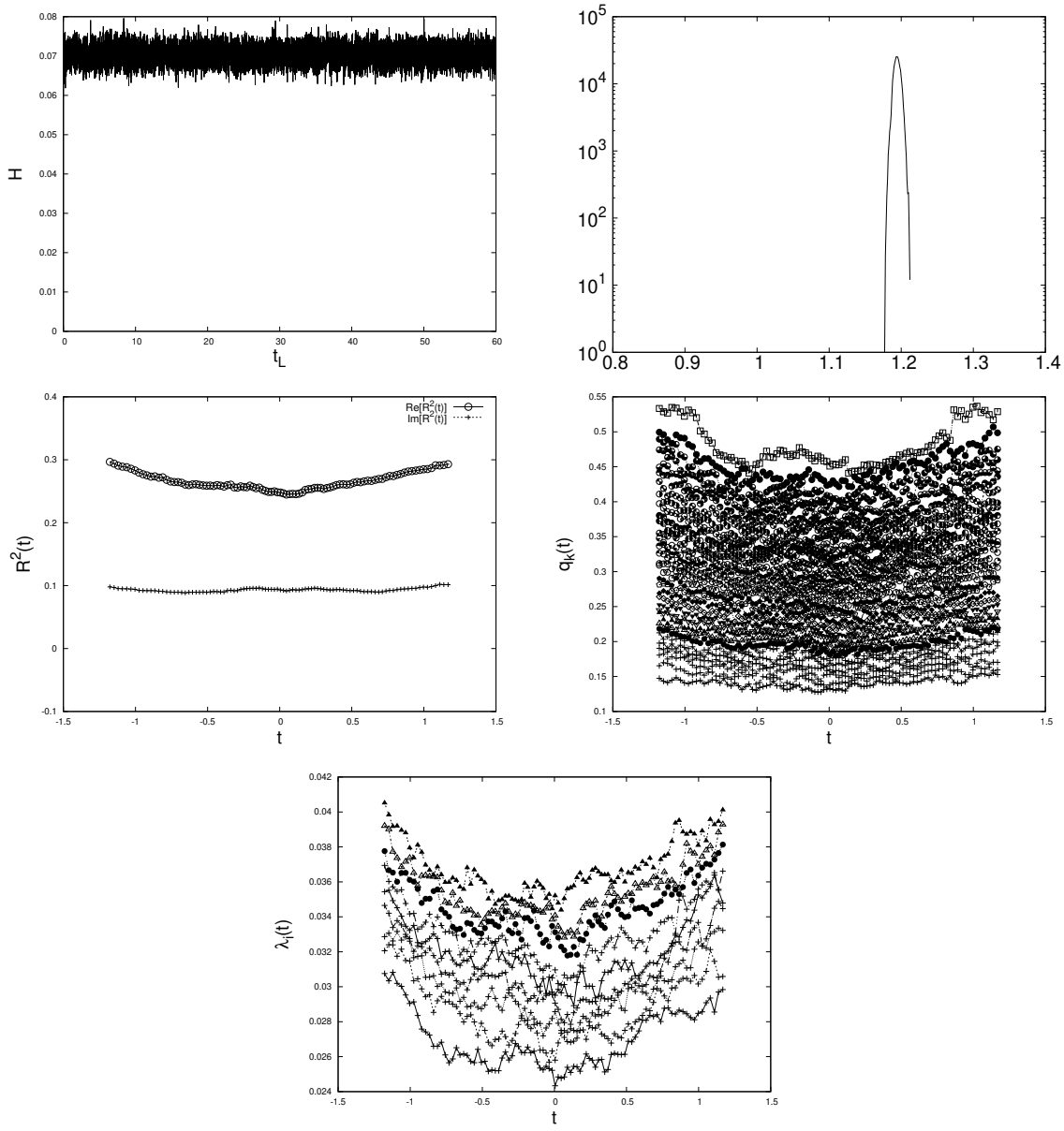

Figure 6.6: We plot the results for the bosonic model with $N = 128$, $\beta = 2.5$, $\kappa = 0.8$ and $(s, k) = (0, 0)$. (Top-Left) A history of the Hermiticity norm where the horizontal axis is the Langevin time. The Hermiticity seems to be controlled. (Top-Right) A histogram of the drift term. This histogram falls off faster than exponential which means the criterion for the correct convergence is satisfied. (Middle-Left) We plot the real and imaginary part of the $R^2(t)$ against the time. There is a little expansion. (Middle-Right) The eigenvalues of $Q(t)$ are plotted against time. This plot shows that the space is continuous. (Bottom) We plot the eigenvalues of $T_{ij}(t)$ which shows that there is no SSB of SO(9).

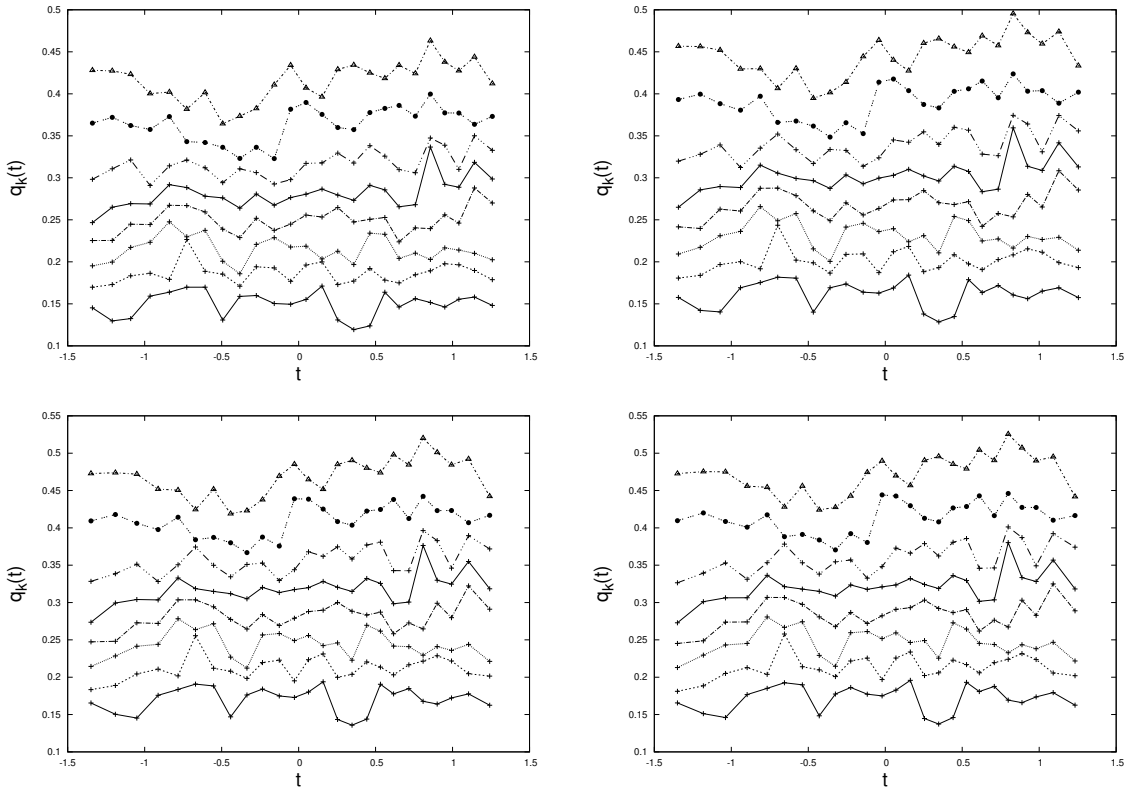

Figure 6.7: We plot the eigenvalues of $Q(t)$ against time for the bosonic model with $N = 32, \beta = 1.4,$ and $\kappa = 1.0$. (Top-Left), (Top-right), (Bottom-Left), and (Bottom-right) correspond to $s = k = 0, 0.3, 0.7,$ and 1 respectively.

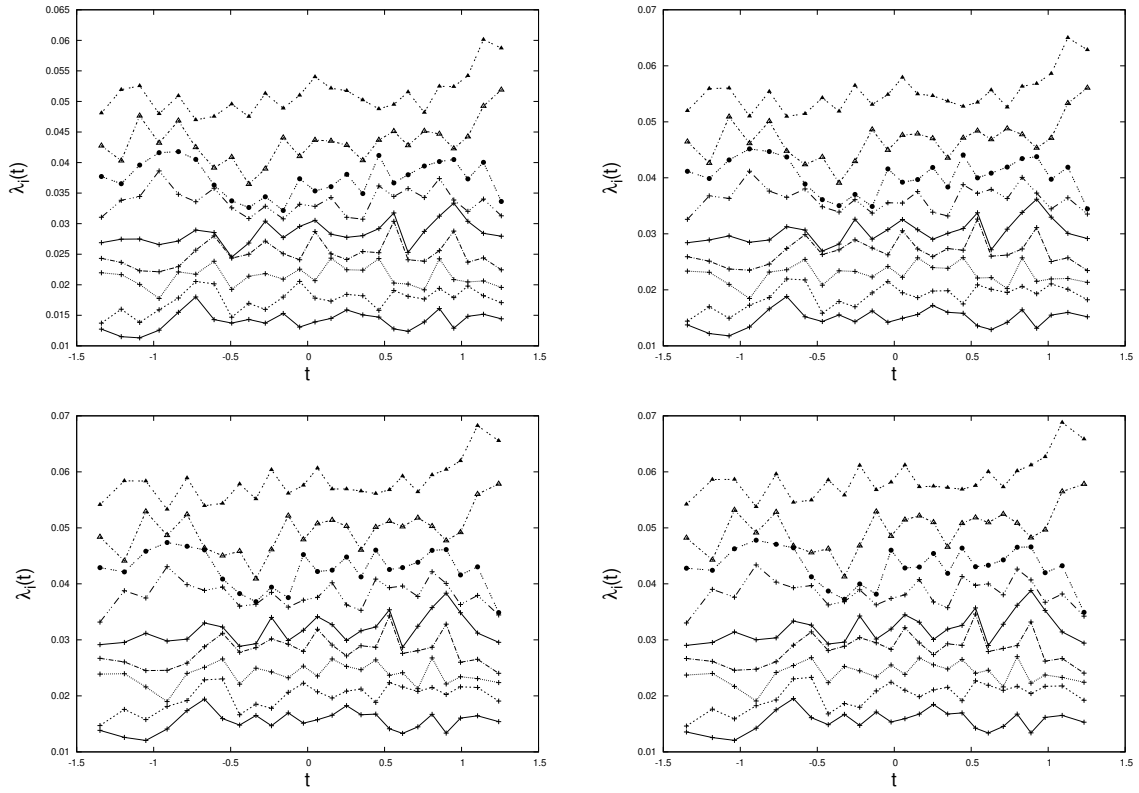

Figure 6.8: We plot the eigenvalues of $T_{ij}(t)$ against time for the bosonic model with $N = 32, \beta = 1.4,$ and $\kappa = 1.0$. (Top-Left), (Top-right), (Bottom-Left), and (Bottom-right) correspond to $s = k = 0, 0.3, 0.7,$ and 1 respectively.

6.3.2 Effects from the fermionic part

In the Euclidean type IIB matrix model, the phase of the Pfaffian plays an essential role in the SSB of the rotational SO(10) symmetry [59]. Therefore, it is expected that the Pfaffian plays an important role also in the Lorentzian type IIB matrix model.

When some of the eigenvalues of the Dirac operator approach 0 the drift term becomes very large. The appearance of such drift terms causes the failure of the CLM. This problem is known as the singular drift problem. In order to avoid this problem, usually, the deformation term is added to the action. The suitable deformation term depends on the model, especially the spectrum of the Dirac operator.

Here we focus on the 6d type IIB matrix model due to the numerical cost. In the 6d model, after the integration for the fermionic matrices, the determinant of the Dirac operator appears instead of Pfaffian which appears in the 10d case. In the Lorentzian type IIB matrix model, the Dirac operator is defined as

$$\mathcal{M}(e^{-ik\pi/2}\mathcal{A}_0, \mathcal{A}_i) := -\Gamma_0[e^{-ik\pi/2}\mathcal{A}_0\ ,\ \cdot\ ] + \Gamma_i[\mathcal{A}_i\ ,\ \cdot\ ], \tag{6.3.2}$$

where matrices Γ_μ are constructed from Pauli matrices σ_i as

$$\begin{aligned} &\Gamma_0 = \mathbb{1} \otimes \mathbb{1}, \quad \Gamma_1 = \sigma_1 \otimes \sigma_2, \quad \Gamma_2 = \sigma_2 \otimes \sigma_2 \\ &\Gamma_3 = \sigma_3 \otimes \sigma_2, \quad \Gamma_4 = \mathbb{1} \otimes \sigma_2, \quad , \Gamma_5 = \mathbb{1} \otimes \sigma_3. \end{aligned} \tag{6.3.3}$$

When the matrices $\mathcal{A}_\mu$ are Hermitian $\mathcal{A}_\mu^\dagger = \mathcal{A}_\mu$ this Dirac operator satisfies the following relation:

$$\mathcal{M}(e^{-ik\pi/2}\mathcal{A}_0, \mathcal{A}_i) = \mathcal{M}^\dagger(e^{-ik\pi/2}\mathcal{A}_0, \mathcal{A}_i). \tag{6.3.4}$$

Therefore the eigenvalues of the Dirac operator are real.

In this case, a suitable deformation term is

$$im_{\mathrm{f}}\Gamma_0\bar{\psi}\psi \tag{6.3.5}$$

where $m_{\mathrm{f}} \in \mathbb{R}$ is called as the deformation parameter. By adding this term to the action, the eigenvalues of the Dirac operator shift to the imaginary direction. As a result, we can avoid the singular drift problem. Since this term modifies the theory, taking $m_{\mathrm{f}} \to 0$ limit is needed.

In Fig. 6.9 and Fig. 6.10, we plot the results at $s = k$ line for the $m_{\mathrm{f}} = 5$ case. We find that there is no qualitative difference between them. Moreover, we cannot see the qualitative differences between the results obtained for the bosonic model and that for the fermionic model. We expect that the reason is the large deformation parameter. We plot the results for the $m_{\mathrm{f}} = 2$ and $m_{\mathrm{f}} = 1$ cases in Fig. 6.11, the results are almost the same as the results for $m_{\mathrm{f}} = 5$ case. Therefore, we consider that $m_{\mathrm{f}} = 1$ is still large to see the fermionic effects.

In Fig. 6.12, we plot the eigenvalues of the Dirac operator. We find that the average of the imaginary part of the eigenvalues is close to the values of m_{f}. Note that, since

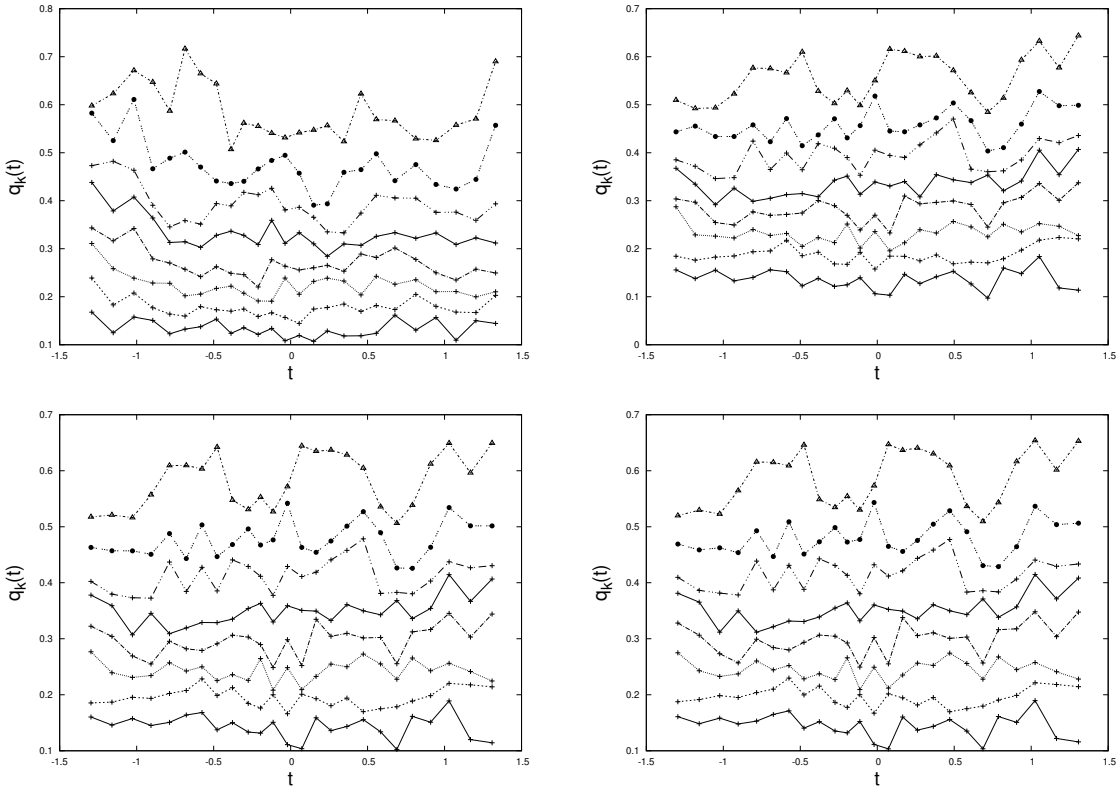

Figure 6.9: We plot the eigenvalues of $Q(t)$ against time for the 6d model with $N = 32$ and $m_{\rm f} = 5$. (Top-Left), (Top-right), (Bottom-Left), and (Bottom-right) correspond to $s = k = 0, 0.3, 0.7,$ and 1 respectively.

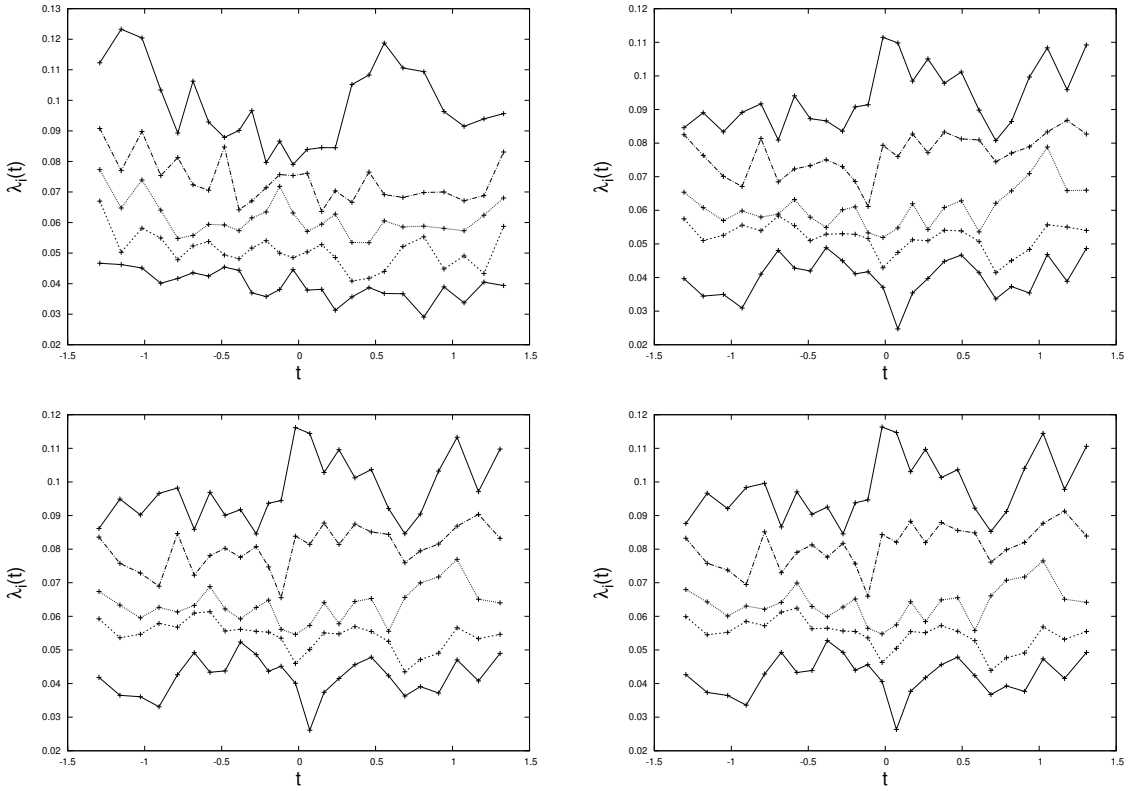

Figure 6.10: We plot the eigenvalues of $T_{ij}(t)$ against time for the 6d model with $N = 32$ and $m_{\rm f} = 5$. (Top-Left), (Top-right), (Bottom-Left), and (Bottom-right) correspond to $s = k = 0, 0.3, 0.7,$ and 1 respectively.

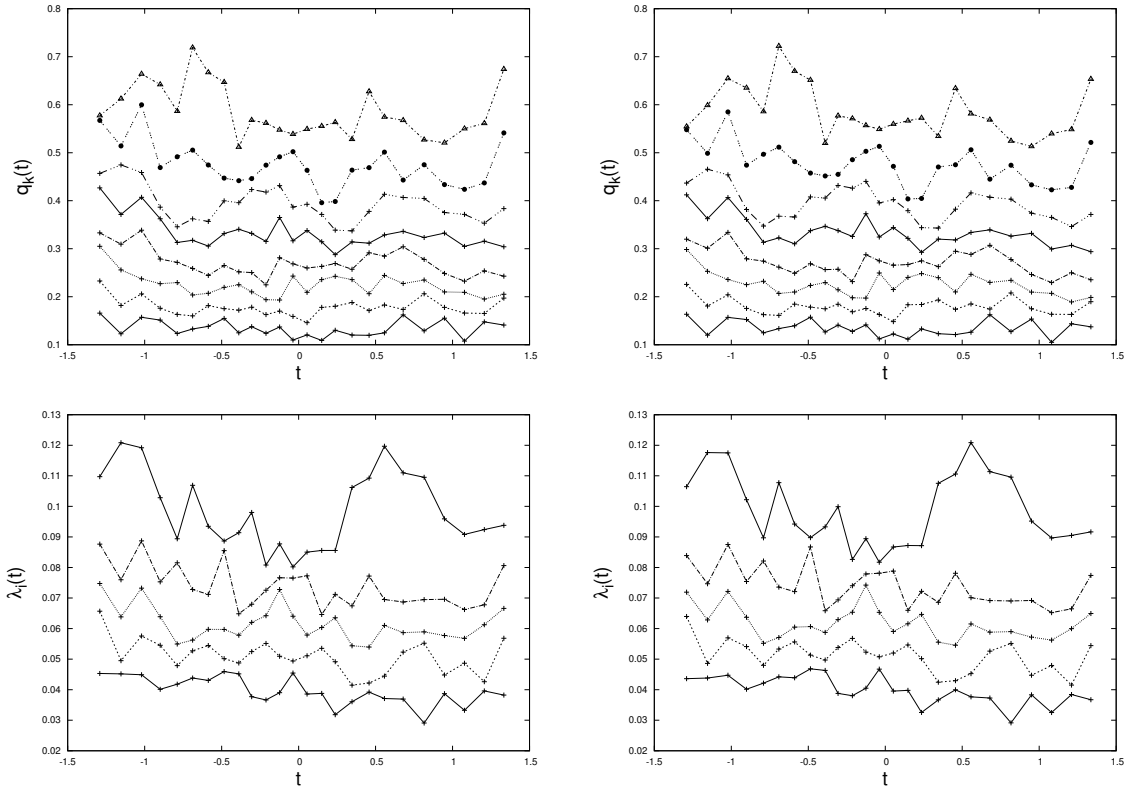

Figure 6.11: The results for the 6d model with $N = 32$. We plot the eigenvalues of $Q(t)$ in (Top) and the eigenvalues of $T_{ij}(t)$ against time in (Bottom). (Left) and (Right) correspond to $m_{\rm f} = 2,$ and 1 respectively.

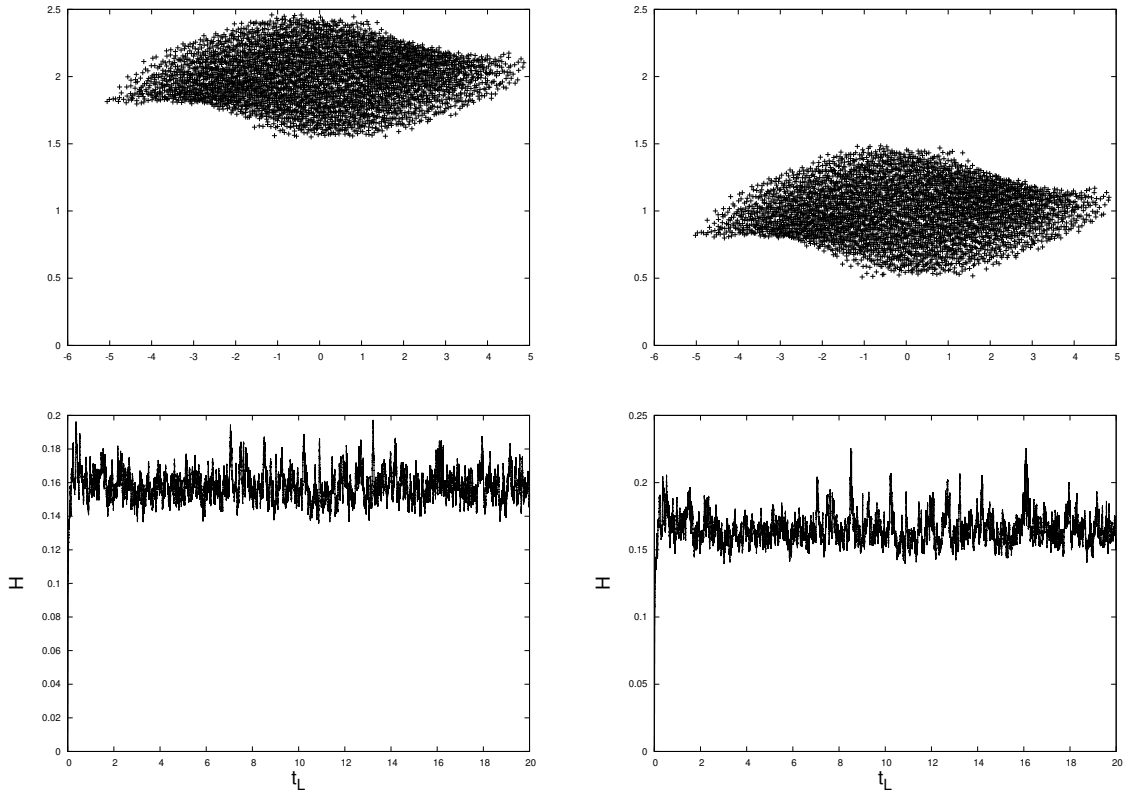

Figure 6.12: The results for the 6d model with $N = 32$. (Top) The eigenvalues of $\mathcal{M}(e^{-ik\pi/2}\mathcal{A}_0, \mathcal{A}_i)$ where the horizontal and vertical axes correspond to real and imaginary part of the eigenvalues respectively. (Bottom) We plot the Hermiticity norm against the Langevin time. (Left) and (Right) correspond to $m_{\rm f} = 2,$ and 1 respectively.

the matrices $\mathcal{A}_\mu$ are deviated from being Hermitian, the eigenvalues are distributed with some width in the imaginary direction. Even at $m_{\rm f} = 1$, the near-zero eigenvalues do not appear. Therefore it is possible to decrease $m_{\rm f}$ more.

Chapter 7

Summary and discussions

In this thesis, we applied the CLM to gauge theories with a θ term and the Lorentzian type IIB matrix model.

7.1 Gauge theories with a θ term

7.1.1 2D U(1) lattice gauge theory with a θ term

In this work, we have made an attempt to apply the CLM to gauge theories with a θ term. As a first step, we applied the CLM to the 2D U(1) case, which is exactly solvable on a finite lattice with various boundary conditions. We find that a naive implementation of the method fails due to the topological nature of the θ term.

While the gauge configurations are complexified in the CLM, one can still define the notion of topological sectors by $\mathrm{Re}\, Q_{\log} \in \mathbb{Z}$. When a transition between different topological sectors occurs, one of the plaquettes has to cross the branch cut inevitably, which causes the appearance of large drift terms. This indeed happens at small β, where we find that the criterion for correct convergence of the CLM is not satisfied. Increasing β makes all the plaquettes close to unity. The large drift terms do not appear in this case, and the criterion for correct convergence of the CLM is satisfied. However, the topology change does not occur during the simulation and the ergodicity is violated. This is analogous to the topology freezing problem, which is known to occur for $\theta = 0$. The results obtained in this case correspond to the expectation values for an ensemble restricted to a particular topological sector specified by the initial configuration.

In order to avoid this problem, we have considered the punctured model, which can be obtained by removing one plaquette from the action, both from the gauge action and from the θ term. While the quantity $\mathrm{Re}\, Q_{\log}$ is no more restricted to integer values, we can still formally classify the complexified configurations into "topological sectors" by adding back the contribution of the removed plaquette to $\mathrm{Re}\, Q_{\log}$. Even for large β, the removed plaquette can cross the branch cut easily, which results in frequent transitions

between different "topological sectors". Note also that, as far as β is sufficiently large, all the other plaquettes are close to unity, and hence large drift terms do not appear. Thus the criterion for correct convergence of the CLM can be satisfied by simply approaching the continuum limit without causing the topology freezing problem. Indeed our results obtained by the CLM for the punctured model reproduce the exact results even at large θ.

In the case of the punctured model, the drift term from the θ term appears only for the link variables composing the removed plaquette, and it is given by $\pm i\frac{\theta}{2\pi}$, which causes multiplication by a constant factor $e^{\mp\Delta t\frac{\theta}{2\pi}}$ to these link variables at each Langevin step. The local unitarity norm of these link variables grows exponentially at early Langevin times, but it saturates at some point to some constant, which increases exponentially for large $|\theta|V_{\rm phys}$. We have seen that the CLM works perfectly even in this situation as far as β is sufficiently large. This provides a counterexample to the common wisdom that the CLM fails when the unitarity norm becomes large. Thus our results also give us new insights into the method itself.

The punctured model is actually equivalent to the non-punctured model in the infinite volume limit for $|\theta| < \pi$. In that limit, the topological charge can take arbitrarily large values, so the discretization of Q to integers is no more important. This equivalence has been confirmed explicitly by obtaining exact results for the punctured model. In fact, the exact results also reveal the absence of finite volume effects in the punctured model as opposed to the non-punctured model, which exhibits sizable finite volume effects around $\theta \sim \pi$. It is conceivable that the smearing of the topological charge somehow results in the reduction of finite volume effects. If so, a similar conclusion should hold more generally.

7.1.2 4D SU(2) lattice gauge theory with a θ term

Since the application of the CLM to the 2D U(1) case was successful, we next applied the CLM to the SU(2) gauge theory with a θ term. First, we naively applied the CLM to the theory. At very small β, the topological charge freely changes during a simulation, however, the criterion for the correct convergence of the CLM is not satisfied. In 4D SU(2) case, unlike in the 2D U(1) case, there is a region for β where the simulations are free from both the topology freezing problem and the wrong convergence. At $\beta = 3.25$, the criterion is satisfied for $|\theta| \leq 2\pi$, however we cannot see the 2π periodicity which the theory has. A possible reason for the absence of 2π periodicity is the UV fluctuations. The fluctuations hinder the appearance of the comb-shaped distribution of the topological charge, as a result, the 2π periodicity does not appear.

One of the ways to reduce the UV fluctuations is using the cooling procedure such as the gradient flow. We applied the gradient flow for $\theta = 0$ case, and then we saw the appearance of the comb-shaped distribution of the topological charge. However, we cannot use the gradient flow in the CLM because this procedure is cannot be justified in

the method. Another way to reduce the UV fluctuations is decreasing the lattice spacing a, which corresponds to increasing β. However, we found that the topology freezing problem occurs at large β.

It is known that the open boundary conditions alleviate the topology freezing problem, however, as a drawback, the strong finite volume effects appear. Therefore, we tried to solve the problem by imposing the open boundary condition for only one of the spatial directions. At $\beta = 6$, we found that the topology freezing is alleviated, however, the alleviation is not enough. Thus, we imposed the open boundary condition for all spatial directions, and we found that the topology freezing is milder than that for the case of open boundary for a spatial direction.

We apply the CLM to the theory with the open boundary condition for all spatial directions and found that the criterion is satisfied for $|\theta| < 2\pi$. In order to study phase structure, we measured the Im Q which is an order parameter for the SSB of the CP symmetry, and the result shows that the Im $Q \neq 0$ at $\theta = \pi$ in the deconfined region. It seems that this result naively implies the CP symmetry is spontaneously broken there. There are two possibilities. One is that critical temperatures satisfy $T_{\rm dec}(\theta = \pi) < T_{\rm CP}$, and the other is that we cannot see the CP restoration due to the finite volume effects and the finite lattice spacing effects.

In order to study the finite volume effects, we performed the simulation for various spatial volume up to $L_{\rm s}^3 = 80^3$. We cannot see the finite volume scaling so far, therefore, we need to increase $L_{\rm s}$ more to take the extrapolation for infinite volume limit. Since the CLM works well at sufficiently large θ, we expect that the phase diagram can be determined by the complex Langevin simulations if we take the infinite volume and the continuum limits.

7.2 The Lorentzian type IIB matrix model

7.2.1 On the emergence of the space-time structure in the type IIB matrix model

In this work, we have investigated the space-time structure of the matrix configurations obtained in Monte Carlo studies of the Lorentzian type IIB matrix model and the simplified models. In these models, the time-evolution can be extracted from the matrix configurations by working in the SU(N) basis which diagonalizes the temporal matrix A_0. The $n \times n$ spatial submatrices $\bar{A}_i(t)$ $(i = 1, \cdots, 9)$ at each time t show that only three out of nine directions expand after some critical time suggesting the SSB of rotational SO(9) symmetry to SO(3). By calculating the eigenvalues of $\bar{A}_i(t)$ at each t, however, we have found that only two of them increase in magnitude with t in the extended directions, while the rest are independent of t and SO(9) symmetric. This implies that the SSB is caused

only by the two eigenvalues. In the continuum limit, the magnitude of the two eigenvalues diverges in physical units and the spatial matrices $\bar{A}_i(t)$ approach a configuration which is essentially described by the Pauli matrices.

We have attributed this problem to the approximation used in Monte Carlo simulation to avoid the sign problem, which actually amounts to replacing $\mathrm{e}^{iS_{\mathrm{b}}}$ by $\mathrm{e}^{\beta S_{\mathrm{b}}}$ in the partition function (5.1.11) of the Lorentzian type IIB matrix model. This new interpretation of the Monte Carlo simulation enables us to understand the interesting aspects of the obtained results such as the band-diagonal structure of the spatial matrices A_i as well as the appearance of the (3+1)d expanding behavior with the Pauli-matrix structure.

7.2.2 Complex Langevin simulation of the Lorentzian type IIB matrix model

In order to treat the weight $\mathrm{e}^{iS_{\mathrm{b}}}$ appropriately, we applied the CLM instead of the approximation. We generalized the model by introducing two parameters s and k which are related to the Wick rotation on the world sheet and that in target space respectively. This generalized model interpolates among the Lorentzian case, the Euclidean case, and a model with $\mathrm{e}^{\beta S_{\mathrm{b}}}$, which correspond to setting $(s,k) = (0,0),\ (1,1),$ and $(-1,0)$ respectively.

In the complex Langevin simulation, when we use quadratic functions for the IR cutoffs, we need to use large coefficients, which sometimes results in the appearance of large drift terms. If these large drift terms appear frequently, the criterion for the correct convergence of the CLM is not satisfied. Therefore, we improved the treatment of the cutoffs by changes of the variables (6.2.3).

We first applied the CLM to the bosonic version of the generalized model which is obtained by neglecting the fermionic part in $\tilde{S}$. We found that, in $(s,k) \neq (-1,0)$ case, if the simulation starts from a configuration obtained from a simulation at $(s,k) = (-1,0)$ then the excursion problem occurs, as a result, the criterion for the correct convergence of the CLM was not satisfied for small matrix size case ($N = 32$). In the $N = 256$ case, although the excursion has not been horrible so far, however, if one continues the simulation for a long time the excursion problem might occur. In other words, the singular structure phase which we observed in a model with the weight $\mathrm{e}^{\beta S_{\mathrm{b}}}$ seems to be unstable at the Lorentzian case.

On the other hand, when the complex Langevin simulation started from scratch the CLM worked well and a new phase appeared. In a new phase, the space is continuous but the spontaneously breaking of the SO(9) symmetry doesn't occur in our preliminary studies. The behaviors in the new phase remind us of the Euclidean bosonic case in which the SO(9) does not break spontaneously. In order to clarify this point, we studied the model on the $s = k$ line, and found the phase in the Lorentzian case is smoothly connected to that in the Euclidean case.

According to the study of the Euclidean type IIB matrix model, the fermionic part plays an important role in the SSB of SO(9). We expect that the same is true in the Lorentzian case. Therefore we applied the CLM to see the 6D version of the generalized model to study the effects of the fermion. When the action includes the fermionic part, in order to avoid the singular drift problem, we add a "mass term" m_{f} which is called a deformation term to the action. We simulated the model at various values of the deformation parameter, and we found that the values which we studied are too large to see the fermionic effects. Fortunately, according to the spectrum of the eigenvalues of the Dirac operator, it may be possible to decrease the value of the parameter more. We expect that the SSB of the SO(9) occurs in the Lorentzian model after taking both the large N and the $m_{\mathrm{f}} \to \infty$ limit as in the case of the Euclidean model.

Acknowledgment

I would like to thank my supervisor Prof. Jun Nishimura for valuable discussions, advices, encouragements, and supports. I also would like to my collaborators, Prof. Asato Tsuchiya, Prof. Konstantinos N. Anagnostopoulos, Prof. Takehiro Azuma, Prof. Masazumi Honda, Prof. Yuta Ito, Dr. Kohta Hatakeyama, Dr. Toshihiro Aoki, Dr. Stratos Kovalkov Papadoudis, Mr. Akira Matsumoto, and Mr. Atis Yosprakob for valuable discussions through collaborations. Numerical computation was carried out on K computer (Project ID : hp170229, hp180178), Oakbridge-CX in University of Tokyo (Project ID : hp120281, hp200106), TSUBASA in KEK (Program No. 2020-009), FX10 in University of Tokyo, the PC clusters in KEK Computing Research Center and KEK Theory Center, and XC40 at YITP in Kyoto University.

Appendix A

Derivation of the exact result

In 2D lattice gauge theory, we can obtain the partition function explicitly on any manifold at finite lattice spacing and finite volume [40], from which various observables can be obtained. In this section, we review the derivation using the so-called K-functional [39].

A.1 The K-functional

Let us consider a lattice gauge theory with a θ term on a 2D lattice manifold $\mathcal{M}$. Here we take the gauge group to be U(N), which is a generalization of U(1) considered so far. Note that the topology of the gauge field becomes trivial for SU(N) in 2D gauge theories.

As a building block for evaluating the partition function, we define the K-functional K_A for the region $A \subset \mathcal{M}$ defined by [39]

$$K_A(\Gamma) = \int \left(\prod_{U_i \in A \setminus C} dU_i \right) e^{-S_A} \ , \tag{A.1.1}$$

where the integral goes over the link variables inside A leaving out those on the boundary C. (See Fig. A.1.) The action S_A in Eq. (A.1.1) is given by

$$S_A = \sum_{P_i \in A} \mathrm{Tr} \left[-\frac{\beta}{2} \left(P_i + P_i^{-1} \right) - \frac{\theta}{2\pi} \log P_i \right] \ , \tag{A.1.2}$$

where the sum goes over the plaquettes P_i included in the region A. Here we use the log definition (3.1.12) of the topological charge, but the results for the sine definition (3.1.13) can be obtained in a similar manner as we mention at the end of Section A.4.

The K-functional depends on the link variables on the boundary $C = \partial A$, but due to the gauge invariance, it actually depends only on

$$\Gamma = \prod_{U_i \in C} U_i \ , \tag{A.1.3}$$

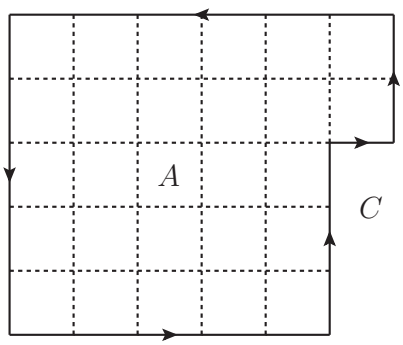

Figure A.1: An example of the region A, which has a boundary $C = \partial A$. The K-functional for this region is defined by integrating out the link variables represented by the dashed lines. The result depends on Γ defined by (A.1.3) for the loop C represented by the solid line with arrows.

which is a consecutive product of link variables along the loop C. The choice of the starting point of the loop C does not matter since a different choice simply corresponds to making a gauge transformation of Γ, which leaves the K-functional invariant.

We can calculate the K-functional for any A by gluing the K-functional for a single plaquette P, which is nothing but

$$K(P) = \exp \mathrm{Tr} \left[\frac{\beta}{2} \left(P + P^{-1} \right) + \frac{\theta}{2\pi} \log P \right] \ . \tag{A.1.4}$$

Note here that (A.1.4) is a function of the group element $P \in \mathrm{U}(N)$, which is invariant under

$$P \to g P g^{-1} \ ; \qquad g \in \mathrm{U}(N) \ . \tag{A.1.5}$$

It is known that any function having this property can be expressed by the so-called character expansion

$$K(P) = \sum_r \lambda_r \chi_r(P) \ , \tag{A.1.6}$$

which is analogous to the Fourier expansion for periodic functions. Here $\chi_r(P)$ is the group character, which is defined by the trace of P for an irreducible representation r, and it satisfies the orthogonality relation

$$\int dU \, \chi_{r_1}(U^{-1}) \chi_{r_2}(U) = \delta_{r_1, r_2} \ . \tag{A.1.7}$$

Using this relation, the coefficient λ_r in the expansion (A.1.6) can be readily obtained as

$$\lambda_r = \int dU \, \chi_r(U^{-1}) K(U) \ . \tag{A.1.8}$$

As an example, let us obtain the K-functional $K_{2\times 1}$ for a 2×1 rectangle by gluing two neighboring plaquettes $P_1 = U_1 \Omega$ and $P_2 = \Omega^{-1} U_2$ as shown in Fig. A.2. The group

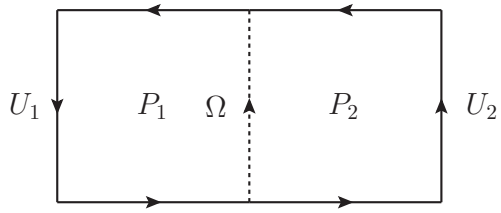

Figure A.2: The K-functional $K_{2\times1}$ for a 2×1 rectangle is obtained by considering the K-functional for the two plaquettes $P_1 = U_1\Omega$ and $P_2 = \Omega^{-1}U_2$, which are glued together by integrating out the shared link variable Ω.

elements U_1 and U_2 are the products of three link variables, and Ω represents the link variable shared by P_1 and P_2. Integrating out the shared link variable Ω, we get

$$\begin{aligned} K_{2\times1}(U_1U_2) &= \int d\Omega\, K(P_1)K(P_2) \\ &= \sum_{r_1,r_2} \lambda_{r_1}\lambda_{r_2} \int d\Omega\, \chi_{r_1}(U_1\Omega)\chi_{r_2}(\Omega^{-1}U_2) \\ &= \sum_r d_r \left(\frac{\lambda_r}{d_r}\right)^2 \chi_r(U_1U_2) \ , \end{aligned} \tag{A.1.9}$$

where $d_r = \chi_r(1)$ is the dimension of the representation r and we have used a formula

$$\int d\Omega\, \chi_{r_1}(U_1\Omega)\chi_{r_2}(\Omega^{-1}U_2) = \frac{1}{d_{r_1}}\chi_{r_1}(U_1U_2)\delta_{r_1,r_2} \ . \tag{A.1.10}$$

Iterating this procedure, we obtain the K-functional for any simply connected region A as

$$K_A(\Gamma) = \sum_r d_r \left(\frac{\lambda_r}{d_r}\right)^{|A|} \chi_r(\Gamma) \ , \tag{A.1.11}$$

where $|A|$ is the number of plaquettes in A, and Γ is defined by (A.1.3).

In the U(1) case, the representation can be labeled by the charge $n \in \mathbb{Z}$, and the dimension of the representation is $d_n = 1$ for $\forall n \in \mathbb{Z}$. Since the character for the plaquette $P = e^{i\phi}$ is given by $\chi_n(P) = e^{in\phi}$, the K-functional for a single plaquette (A.1.6) reduces to

$$K(P) = \sum_{n=-\infty}^{+\infty} \lambda_n e^{in\phi} \ , \tag{A.1.12}$$

where the coefficient λ_n is a function of θ and β given explicitly as

$$\begin{aligned} \lambda_n &\equiv \mathcal{I}(n,\theta,\beta) \\ &= \frac{1}{2\pi}\int_{-\pi}^{\pi} d\phi\, e^{-in\phi} K\left(P = e^{i\phi}\right) \\ &= \frac{1}{2\pi}\int_{-\pi}^{\pi} d\phi\, \exp\left[\beta\cos\phi + i\left(\frac{\theta}{2\pi} - n\right)\phi\right] \end{aligned} \tag{A.1.13}$$

using (A.1.4) with $P = e^{i\phi}$. This function reduces to the modified Bessel function of the first kind for $\theta = 0$.

The character expansion in the U(N) case is more complicated, so we only show the end results referring the reader, for instance, to the appendix of Ref. [92] for the details. The representation of the U(N) group is labeled by N integers

$$\rho = (\rho_1, \rho_2, \cdots, \rho_N) \in \mathbb{Z}^N \tag{A.1.14}$$

satisfying $\rho_i \geq \rho_{i+1}$, and the dimension of the representation ρ can be calculated by

$$d_\rho = \chi_\rho(1) = \prod_{i>j}^{N} \left(1 - \frac{\rho_i - \rho_j}{i-j}\right) \ . \tag{A.1.15}$$

The coefficient λ_ρ in (A.1.6) that corresponds to the representation ρ is expressed as a determinant

$$\lambda_\rho = \det \mathcal{M}(\rho, \theta, \beta) \ , \tag{A.1.16}$$

where the matrix $\mathcal{M}(\rho, \theta, \beta)$ is given as

$$\mathcal{M}_{jk}(\rho, \theta, \beta) = \frac{1}{2\pi} \int_{-\pi}^{\pi} d\phi \, \exp\left[\beta \cos\phi + i\left(\frac{\theta}{2\pi} + \rho_k + j - k\right)\phi\right] \ , \tag{A.1.17}$$

which may be viewed as a generalization of (A.1.13).

A.2 Partition function for the non-punctured model

Let us evaluate the partition function for the 2D U(N) lattice gauge theory on a torus. For that, we first consider the K-functional $K_{L_1 \times L_2}$ for a rectangle composed of $V = L_1 \times L_2$ plaquettes, which can be expressed as (A.1.11). As is shown in Fig. A.3, we identify the top and bottom sides represented by U^{-1} and U, respectively, and identify the left and right sides represented by W^{-1} and W, respectively. Integrating out the group elements U and W, we obtain the partition function for the non-punctured model as

$$\begin{aligned} Z_{\text{nonpunc}} &= \int dU dW \, K_{L_1 \times L_2}(UWU^{-1}W^{-1}) \\ &= \sum_r d_r \left(\frac{\lambda_r}{d_r}\right)^V \int dU dW \chi_r(UWU^{-1}W^{-1}) \\ &= \sum_r \left(\frac{\lambda_r}{d_r}\right)^V \int dU \chi_r(U)\chi_r(U^{-1}) \\ &= \sum_r \left(\frac{\lambda_r}{d_r}\right)^V \ , \end{aligned} \tag{A.2.1}$$

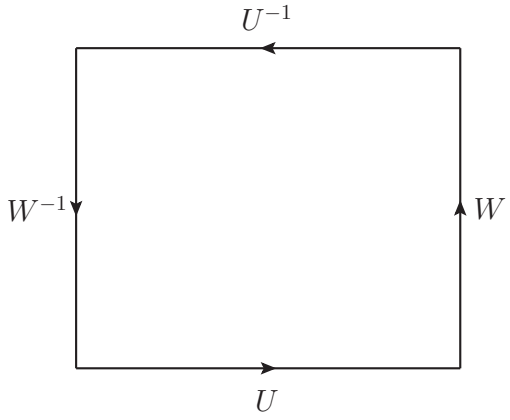

Figure A.3: The partition function for the 2D U(N) gauge theory on a torus is obtained from the K-functional for the rectangle by integrating out the group elements U and W corresponding to the identified sides.

where we have used the orthogonality relation (A.1.7) and a formula

$$\int d\Omega\, \chi_r(U\Omega W\Omega^{-1}) = \frac{1}{d_r}\chi_r(U)\chi_r(W)\ . \tag{A.2.2}$$

In the U(1) case, the partition function (A.2.1) reduces to

$$Z_{\text{nonpunc}} = \sum_{n=-\infty}^{+\infty} \left[\mathcal{I}(n,\theta,\beta)\right]^V\ . \tag{A.2.3}$$

As one can see from (A.1.13), the integral $\mathcal{I}(n,\theta,\beta)$ has a property $\mathcal{I}(n,\theta+2\pi k,\beta) = \mathcal{I}(n-k,\theta,\beta)$ for $\forall k \in \mathbb{Z}$, which guarantees the 2π periodicity of (A.2.3) in θ.

Let us consider taking the $V \to \infty$ and $\beta \to \infty$ limits simultaneously with fixed $V_{\text{phys}} \equiv V/\beta$, which corresponds to the continuum limit. In this limit, the integral (A.1.13) can be evaluated as

$$\mathcal{I}(n,\theta,\beta) \simeq \frac{1}{\sqrt{2\pi\beta}} e^{\beta - \frac{1}{2\beta}\left(\frac{\theta}{2\pi}-n\right)^2}\ . \tag{A.2.4}$$

Plugging this into (A.2.3), we obtain

$$\begin{aligned} Z_{\text{nonpunc}} &\simeq \left(\frac{e^\beta}{\sqrt{2\pi\beta}}\right)^V \sum_{n=-\infty}^{+\infty} \exp\left[-\frac{V}{2\beta}\left(\frac{\theta}{2\pi}-n\right)^2\right] \\ &\sim \sum_{n=-\infty}^{+\infty} \exp\left[-\frac{1}{2}V_{\text{phys}}\left(\frac{\theta}{2\pi}-n\right)^2\right]\ , \end{aligned} \tag{A.2.5}$$

omitting the divergent constant factor.

A.3 Partition function for the punctured model

Let us extend the calculation in the previous section to the punctured model. First, we calculate the K-functional for a rectangle with a hole shown in Fig. A.4, which we divide

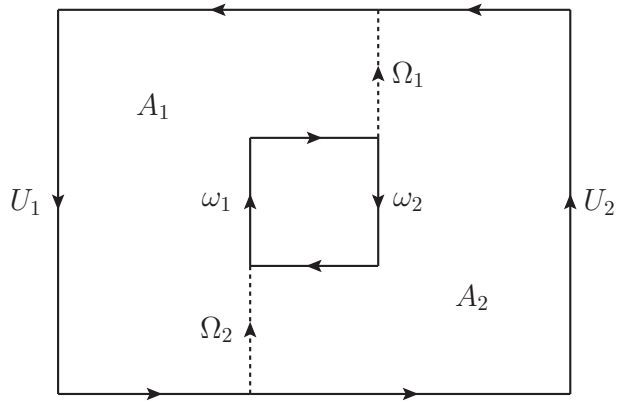

Figure A.4: The K-functional for a rectangle with a hole is obtained by gluing the two regions A_1 and A_2. From this, the K-functional for the punctured torus is obtained similarly to what we did in Fig. A.3. Integrating out the link variables surrounding the puncture, we obtain the partition function for the 2D U(N) gauge theory on a punctured torus.

into two regions A_1 and A_2 by cutting along two segments Ω_1 and Ω_2. The outer and inner boundaries of the rectangle are divided into two segments (U_1, U_2) and (ω_1, ω_2), respectively. Then, the K-functional for each region is given, respectively, as

$$K_{A_1}(U_1\Omega_2\omega_1\Omega_1) = \sum_{r_1} d_{r_1} \left(\frac{\lambda_{r_1}}{d_{r_1}}\right)^{|A_1|} \chi_{r_1}(U_1\Omega_2\omega_1\Omega_1) \ , \tag{A.3.1}$$

$$K_{A_2}(\Omega_1^{-1}\omega_2\Omega_2^{-1}U_2) = \sum_{r_2} d_{r_2} \left(\frac{\lambda_{r_2}}{d_{r_2}}\right)^{|A_2|} \chi_{r_2}(\Omega_1^{-1}\omega_2\Omega_2^{-1}U_2) \ . \tag{A.3.2}$$

By gluing the two regions A_1 and A_2 together at Ω_1 and Ω_2, we obtain the K-functional for the rectangle with a hole as

$$\begin{aligned} K_{A_1\cup A_2} &= \int d\Omega_1 d\Omega_2 \, K_{A_1}(U_1\Omega_2\omega_1\Omega_1) K_{A_2}(\Omega_1^{-1}\omega_2\Omega_2^{-1}U_2) \\ &= \sum_{r_1,r_2} d_{r_1} d_{r_2} \left(\frac{\lambda_{r_1}}{d_{r_1}}\right)^{|A_1|} \left(\frac{\lambda_{r_2}}{d_{r_2}}\right)^{|A_2|} \int d\Omega_1 d\Omega_2 \chi_{r_1}(U_1\Omega_2\omega_1\Omega_1)\chi_{r_2}(\Omega_1^{-1}\omega_2\Omega_2^{-1}U_2) \\ &= \sum_{r} d_r \left(\frac{\lambda_r}{d_r}\right)^{|A_1|} \left(\frac{\lambda_r}{d_r}\right)^{|A_2|} \int d\Omega_2 \chi_r(U_1\Omega_2\omega_1\omega_2\Omega_2^{-1}U_2) \\ &= \sum_{r} \left(\frac{\lambda_r}{d_r}\right)^{V} \chi_r(U_1U_2)\chi_r(\omega_1\omega_2) \ , \end{aligned} \tag{A.3.3}$$

where we have defined $V = |A_1 \cup A_2| = |A_1| + |A_2|$.

Let us introduce the group elements U and W for the outer boundary as we did in Fig. A.3 so that $U_1U_2 = UWU^{-1}W^{-1}$, and define $\omega = \omega_1\omega_2$ for the inner boundary. Integrating out the group elements U and W, we obtain the K-functional for the punctured

torus as

$$
\begin{aligned}
K_{\text{punc}}(\omega) &= \sum_r \left(\frac{\lambda_r}{d_r}\right)^V \chi_r(\omega) \int dU dW \chi_r(UWU^{-1}W^{-1}) \\
&= \sum_r \left(\frac{\lambda_r}{d_r}\right)^V \chi_r(\omega) \int dU \frac{1}{d_r} \chi_r(U)\chi_r(U^{-1}) \\
&= \sum_r \frac{1}{d_r} \left(\frac{\lambda_r}{d_r}\right)^V \chi_r(\omega) \ . \qquad \text{(A.3.4)}
\end{aligned}
$$

Finally, we integrate out the link variables surrounding the puncture to get the partition function for the punctured model as

$$
Z_{\text{punc}} = \int d\omega \, K_{\text{punc}}(\omega) = \sum_r \frac{1}{d_r} \left(\frac{\lambda_r}{d_r}\right)^V \delta_{r,0} = (\lambda_0)^V \ , \qquad \text{(A.3.5)}
$$

where $r = 0$ corresponds to the trivial representation, which has $d_0 = 1$.

In the U(1) case, the partition function reduces to

$$
Z_{\text{punc}} = \left[\mathcal{I}(0, \theta, \beta)\right]^V \ , \qquad \text{(A.3.6)}
$$

which does not have the 2π periodicity in θ.

Let us consider taking the $V \to \infty$ and $\beta \to \infty$ limits simultaneously with fixed $V_{\text{phys}} \equiv V/\beta$, which corresponds to the continuum limit. Similarly to the case of the non-punctured model discussed in Section A.2, we obtain

$$
\begin{aligned}
Z_{\text{punc}} &\simeq \left(\frac{e^\beta}{\sqrt{2\pi\beta}}\right)^V \exp\left[-\frac{V}{2\beta}\left(\frac{\theta}{2\pi}\right)^2\right] \\
&\sim \exp\left[-\frac{1}{2} V_{\text{phys}} \left(\frac{\theta}{2\pi}\right)^2\right] \ , \qquad \text{(A.3.7)}
\end{aligned}
$$

omitting the divergent constant factor. This coincides with (A.2.5) in the $V_{\text{phys}} \to \infty$ limit for $|\theta| < \pi$. Note, however, that the equivalence between the punctured and non-punctured models does not hold for finite V_{phys}.

A.4 Evaluation of the observables

We can evaluate the expectation values of various observables defined in Section 3.2.4 from the partition function derived above, namely (A.2.3) for the non-punctured model and (A.3.6) for the punctured model. Since the latter case is easier due to the absence of an infinite sum, we only discuss the former case in what follows.

The average plaquette w defined by (3.2.14) is given as

$$
w = \frac{1}{Z_{\text{nonpunc}}} \sum_{n=-\infty}^{+\infty} \mathcal{A}(n, \theta, \beta) \left[\mathcal{I}(n, \theta, \beta)\right]^V \ , \qquad \text{(A.4.1)}
$$

where we have defined

$$\begin{aligned}\mathcal{A}(n,\theta,\beta) &= \frac{\partial}{\partial\beta}\log\mathcal{I}(n,\theta,\beta) \\ &= \frac{1}{\mathcal{I}(n,\theta,\beta)}\frac{1}{2\pi}\int_{-\pi}^{\pi}d\phi\,\cos\phi\exp\left[\beta\cos\phi+i\left(\frac{\theta}{2\pi}-n\right)\phi\right] \\ &= \frac{\mathcal{I}(n-1,\theta,\beta)+\mathcal{I}(n+1,\theta,\beta)}{2\mathcal{I}(n,\theta,\beta)}\ .\end{aligned} \tag{A.4.2}$$

Similarly, the topological charge density defined by (3.2.15) can be obtained from

$$\langle Q\rangle = -i\frac{V}{Z_{\text{nonpunc}}}\sum_{n=-\infty}^{+\infty}\mathcal{B}(n,\theta,\beta)\left[\mathcal{I}(n,\theta,\beta)\right]^V\ , \tag{A.4.3}$$

where we have defined

$$\begin{aligned}\mathcal{B}(n,\theta,\beta) &= \frac{1}{\mathcal{I}(n,\theta,\beta)}\frac{\partial}{\partial\theta}\mathcal{I}(n,\theta,\beta) \\ &= \frac{i}{\mathcal{I}(n,\theta,\beta)}\frac{1}{4\pi^2}\int_{-\pi}^{\pi}d\phi\,\phi\exp\left[\beta\cos\phi+i\left(\frac{\theta}{2\pi}-n\right)\phi\right]\ .\end{aligned} \tag{A.4.4}$$

Finally, the topological susceptibility defined by (3.2.16) can be obtained from

$$\langle Q^2\rangle = -\frac{V}{Z_{\text{nonpunc}}}\sum_{n=-\infty}^{+\infty}\left[\mathcal{C}(n,\theta,\beta)+(V-1)\mathcal{B}(n,\theta,\beta)^2\right]\left[\mathcal{I}(n,\theta,\beta)\right]^V\ , \tag{A.4.5}$$

where we have defined

$$\begin{aligned}\mathcal{C}(n,\theta,\beta) &= \frac{1}{\mathcal{I}(n,\theta,\beta)}\frac{\partial^2}{\partial\theta^2}\mathcal{I}(n,\theta,\beta) \\ &= -\frac{1}{\mathcal{I}(n,\theta,\beta)}\frac{1}{8\pi^3}\int_{-\pi}^{\pi}d\phi\,\phi^2\exp\left[\beta\cos\phi+i\left(\frac{\theta}{2\pi}-n\right)\phi\right]\ .\end{aligned} \tag{A.4.6}$$

Note that $\mathcal{I}(n,\theta,\beta)$ and the functions (A.4.2), (A.4.4) and (A.4.6) derived from it are all real-valued, and we can calculate them by numerical integration with sufficient precision. Also, when we evaluate the infinite sum in the expressions (A.4.1), (A.4.3) and (A.4.5), we have to truncate it at some n. Note here that $|\mathcal{I}(n,\theta,\beta)|$ vanishes quickly as $|\theta/2\pi-n|$ increases. We can therefore evaluate the infinite sum with sufficient precision by keeping only a few terms when the lattice volume V is sufficiently large.

In this section, we have derived the exact results for the log definition (3.1.12) of the topological charge. As is clear from the derivation, we can obtain the exact results for the sine definition (3.1.13) by simply replacing $\mathcal{I}(n,\theta,\beta)$ with

$$\tilde{\mathcal{I}}(n,\theta,\beta) = \frac{1}{2\pi}\int_{-\pi}^{\pi}d\phi\exp\left[\beta\cos\phi+i\frac{\theta}{2\pi}\sin\phi-in\phi\right]\ . \tag{A.4.7}$$

Appendix B

The punctured model with the sine definition $Q_{\sin}$

In Sections 3.3 and 3.4, we have discussed the punctured model with the log definition (3.1.12) of the topological charge for simplicity. In fact, we can also use the sine definition (3.1.13) in the punctured model. Here we discuss what happens in this case.

The drift terms for the sine definition are given already for the non-punctured model in Section 3.2.1. When we consider the punctured model, the only modification from the non-punctured model appears in the drift terms for the four link variables surrounding the puncture; i.e., $\mathcal{U}_{K,1}$, $\mathcal{U}_{K+\hat{2},1}$, $\mathcal{U}_{K,2}$ and $\mathcal{U}_{K+\hat{1},2}$. Thus the drift terms are given as

$$D_{n,1}S = \begin{cases} -i\frac{\beta}{2}(P_n - P_n^{-1} - P_{n-\hat{2}} + P_{n-\hat{2}}^{-1}) - i\frac{\theta}{4\pi}(P_n + P_n^{-1} - P_{n-\hat{2}} - P_{n-\hat{2}}^{-1}) \\ \qquad\qquad\qquad\qquad\qquad\qquad\qquad\qquad \text{for } n \neq K,\ K+\hat{2}\ , \\ -i\frac{\beta}{2}(-P_{K-\hat{2}} + P_{K-\hat{2}}^{-1}) + i\frac{\theta}{4\pi}(P_{K-\hat{2}} + P_{K-\hat{2}}^{-1}) \qquad \text{for } n = K\ , \\ -i\frac{\beta}{2}(P_{K+\hat{2}} - P_{K+\hat{2}}^{-1}) - i\frac{\theta}{4\pi}(P_{K+\hat{2}} + P_{K+\hat{2}}^{-1}) \qquad \text{for } n = K+\hat{2}\ , \end{cases} \tag{B.0.1}$$

$$D_{n,2}S = \begin{cases} -i\frac{\beta}{2}(-P_n + P_n^{-1} + P_{n-\hat{1}} - P_{n-\hat{1}}^{-1}) - i\frac{\theta}{4\pi}(-P_n - P_n^{-1} + P_{n-\hat{1}} + P_{n-\hat{1}}^{-1}) \\ \qquad\qquad\qquad\qquad\qquad\qquad\qquad\qquad \text{for } n \neq K,\ K+\hat{1}\ , \\ -i\frac{\beta}{2}(P_{K-\hat{1}} - P_{K-\hat{1}}^{-1}) - i\frac{\theta}{4\pi}(P_{K-\hat{1}} + P_{K-\hat{1}}^{-1}) \qquad \text{for } n = K\ , \\ -i\frac{\beta}{2}(-P_{K+\hat{1}} + P_{K+\hat{1}}^{-1}) + i\frac{\theta}{4\pi}(P_{K+\hat{1}} + P_{K+\hat{1}}^{-1}) \qquad \text{for } n = K+\hat{1}\ . \end{cases} \tag{B.0.2}$$

At large β, all the plaquettes except P_K, namely the one that is removed, approach unity. The drift term from the θ term therefore vanishes for all the link variables except for those surrounding the puncture, which have constant drifts $\pm i\frac{\theta}{2\pi}$. Thus in the continuum limit, the drift terms for the sine definition agree with those for the log definition given by (3.4.1) and (3.4.2). This connection makes it easier to understand why we can safely ignore the issue of δ-function in the drift term for the log definition described in Section 3.2.1.

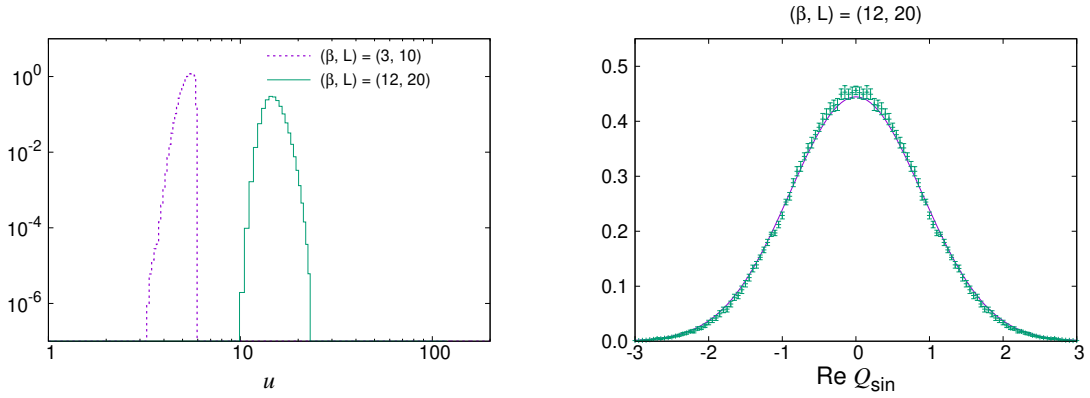

Figure B.1: The results obtained by the CLM for the punctured model using the sine definition of the topological charge. (Left) The histogram of the magnitude u of the drift term is shown for $(\beta, L) = (3, 10)$ and $(12, 20)$ with $\theta = \pi$. (Right) The histogram of $\mathrm{Re}\, Q_{\rm sin}$ for the punctured model is shown for $(\beta, L) = (12, 20)$ with $\theta = \pi$. The exact result obtained for $(\beta, L) = (12, 20)$ with $\theta = 0$ is shown by the solid line for comparison.

It is therefore expected that the results of the CLM for the sine definition are essentially the same as those for the log definition for large β. In Fig. B.1, we show our results for the punctured model with the sine definition for the same (β, L) as those in Fig. 3.7 with the log definition. For $(\beta, L) = (12, 20)$, we find that the histogram of the magnitude u of the drift term falls off rapidly, and that the histogram of $\mathrm{Re}\, Q_{\rm sin}$ obtained by the CLM is widely distributed within the range $-3 \lesssim \mathrm{Re}\, Q_{\rm sin} \lesssim 3$. Hence the topology freezing problem is circumvented without causing large drifts similarly to the situation with the log definition.

On the other hand, for $(\beta, L) = (3, 10)$, we find that the histogram of the magnitude u of the drift term falls off fast and that the condition for the validity of the CLM is satisfied unlike the case of the log definition. As a result, all the observables are in complete agreement with the exact results for all values of θ even with $(\beta, L) = (3, 10)$. This can be seen from Fig. B.2, where we show our results for the punctured model with the sine definition for the same values of (β, L) as the ones used in Fig. 3.12. For $(\beta, L) = (1.92, 8)$ corresponding to the same $V_{\rm phys} \equiv L^2/\beta$, however, we actually find that the histogram has a power-law tail similarly to the case of the log definition. Therefore, the difference between the two definitions is merely a small shift in the validity region of the CLM.

We also show the exact results for the punctured model with the log and sine definitions, which tend to agree as β is increased with fixed $V_{\rm phys} \equiv L^2/\beta$, which corresponds to the continuum limit.

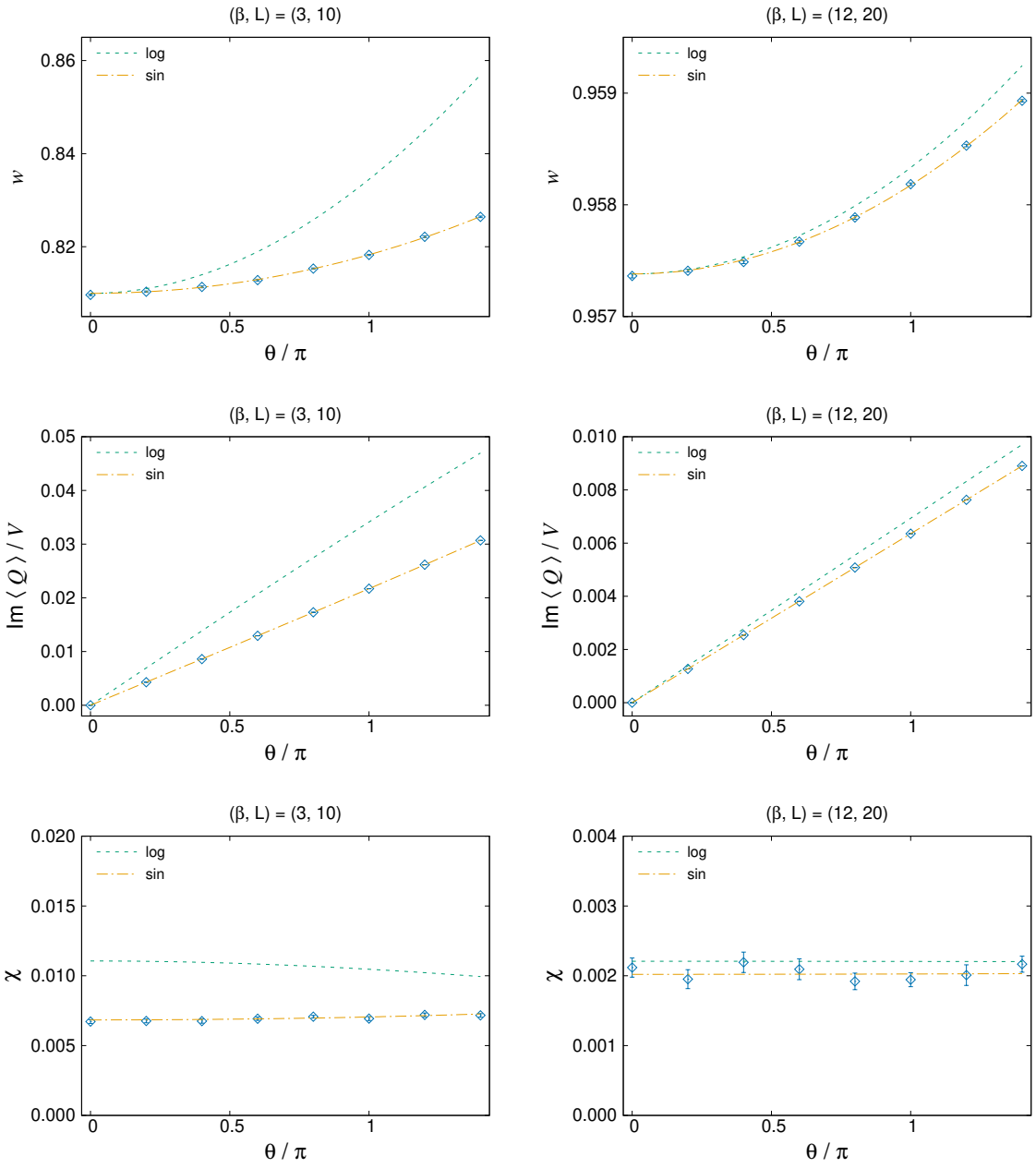

Figure B.2: The results for various observables obtained by the CLM for the punctured model with the sine definition $Q_{\sin}$. The average plaquette (Top), the imaginary part of the topological charge density (Middle), the topological susceptibility (Bottom) are plotted against θ for $(\beta, L) = (3, 10)$ (Left) and $(12, 20)$ (Right). The exact results for the punctured model with the log and sine definitions are shown for the same (β, L) by the dashed lines and the dash-dotted lines, respectively, for comparison.

Appendix C

The determination of the parameter p

In this appendix, we explain how we determine the parameter p in the IR cutoff (5.1.13) and (5.1.14). While a naive choice would be $p = 1$, it was proposed in ref. [87] that one should choose a slightly larger value so that the results become almost independent of p. There it was found in the VDM model that the results for the extent of space $R^2(t)$ become independent of p when p is larger[1] than $p_c = 1.2 \sim 1.3$. Based on this observation, we used $p = 1.4$ when we simulate the VDM model in section 5.2.3.

Here we repeat the same analysis in the case of the bosonic model and the original model. In Fig. C.1, we plot the extent of space $R^2(t)/R^2(t_c)$ against time $(t - t_c)/R(t_c)$ for the bosonic model (Left) and the original model (Right), respectively, with various values of p. For all values of p, we find that only three directions start to expand at some critical time t_c. In the bosonic model, the results scale for $p = 1.3, 1.4, 1.5$ except for the data around the peak of $R^2(t)$. Similar scaling behavior is observed for the original model for $p = 1.4, 1.5, 1.6$. Based on these results, we use $p = 1.5$ for the bosonic model and $p = 1.6$ for the original model in sections 5.2.1 and 5.2.2, respectively.

[1] For the values of p in this region, it was also observed [87] from the analysis of the Schwinger-Dyson equations that the effect of the IR cutoff decreases as one takes the infinite volume limit.

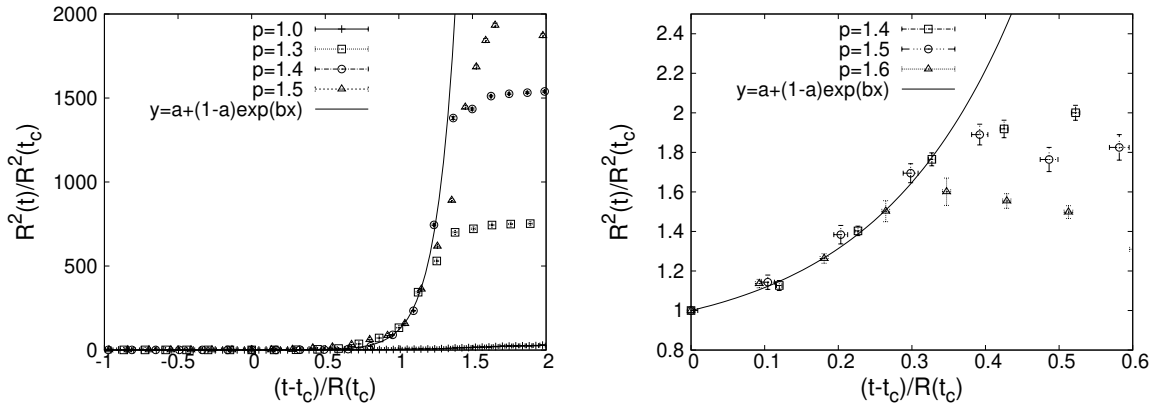

Figure C.1: (Left) The extent of space $R^2(t)/R^2(t_c)$ obtained for the bosonic model is plotted against $x = (t - t_c)/R(t_c)$ for various values of p with $N = 256$, $C = 100$, $\kappa = 1.0$. The block size is chosen as $n = 32, 24, 20, 18$ for $p = 1.0, 1.3, 1.4, 1.5$, respectively. The solid line represents a fit to the $p = 1.4$ data with $R^2(t)/R^2(t_c) = a+(1-a)\exp(bx)$, which gives $a = 0.92(5)$, $b = 7.3(6)$. (Right) The extent of space $R^2(t)/R^2(t_c)$ obtained for the original model is plotted against $x = (t - t_c)/R(t_c)$ for various values of p with $N = 16$, $C = 5$, $\kappa = 0.46$. The block size is chosen as $n = 7, 6, 6$ for $p = 1.4, 1.5, 1.6$, respectively. The solid line represents a fit to the $p = 1.6$ data with $R^2(t)/R^2(t_c) = a + (1 - a)\exp(bx)$, which gives $a = 0.83(4)$, $b = 5.3(7)$.

Bibliography

[1] John R. Klauder. Coherent State Langevin Equations for Canonical Quantum Systems With Applications to the Quantized Hall Effect. Phys. Rev. A, 29:2036–2047, 1984.

[2] G. Parisi. ON COMPLEX PROBABILITIES. Phys. Lett. B, 131:393–395, 1983.

[3] Gert Aarts, Erhard Seiler, and Ion-Olimpiu Stamatescu. The Complex Langevin method: When can it be trusted? Phys. Rev. D, 81:054508, 2010.

[4] Gert Aarts, Frank A. James, Erhard Seiler, and Ion-Olimpiu Stamatescu. Complex Langevin: Etiology and Diagnostics of its Main Problem. Eur. Phys. J. C, 71:1756, 2011.

[5] Keitaro Nagata, Jun Nishimura, and Shinji Shimasaki. Justification of the complex Langevin method with the gauge cooling procedure. PTEP, 2016(1):013B01, 2016.

[6] Keitaro Nagata, Jun Nishimura, and Shinji Shimasaki. Argument for justification of the complex Langevin method and the condition for correct convergence. Phys. Rev. D, 94(11):114515, 2016.

[7] Michael Levin and Cody P. Nave. Tensor renormalization group approach to 2d classical lattice models. Phys.Rev.Lett., 99(12):120601, 2007.

[8] Z. Y. Xie, J. Chen, M. P. Qin, J. W. Zhu, L. P. Yang, and T. Xiang. Coarse-graining renormalization by higher-order singular value decomposition. Phys. Rev. B, 86:045139, Jul 2012.

[9] G. Evenbly and G. Vidal. Tensor network renormalization. Phys. Rev. Lett., 115:180405, Oct 2015.

[10] Daiki Adachi, Tsuyoshi Okubo, and Synge Todo. Anisotropic tensor renormalization group.

[11] Daisuke Kadoh and Katsumasa Nakayama. Renormalization group on a triad network.

[12] Edward Witten. Analytic continuation of Chern-Simons theory. AMS/IP Stud. Adv. Math., 50:347–446, 2011.

[13] Marco Cristoforetti, Francesco Di Renzo, and Luigi Scorzato. New approach to the sign problem in quantum field theories: High density qcd on a lefschetz thimble. Phys.Rev.D, 86:074506, 2012.

[14] H. Fujii, D. Honda, M. Kato, Y. Kikukawa, S. Komatsu, and T. Sano. Hybrid monte carlo on lefschetz thimbles - a study of the residual sign problem. JHEP, 10:147, 2013.

[15] Andrei Alexandru, Gokce Basar, Paulo F. Bedaque, Gregory W. Ridgway, and Neill C. Warrington. Sign problem and monte carlo calculations beyond lefschetz thimbles. JHEP, 05:053, 2016.

[16] Masafumi Fukuma and Naoya Umeda. Parallel tempering algorithm for integration over lefschetz thimbles. PTEP, 2017(7):073B01, 2017.

[17] Masafumi Fukuma, Nobuyuki Matsumoto, and Naoya Umeda. Implementation of the hmc algorithm on the tempered lefschetz thimble method.

[18] Yuto Mori, Kouji Kashiwa, and Akira Ohnishi. Toward solving the sign problem with path optimization method. Phys.Rev.D, 96(11):111501, 2017.

[19] Yuto Mori, Kouji Kashiwa, and Akira Ohnishi. Application of a neural network to the sign problem via the path optimization method. PTEP, 2018(2):023B04, 2018.

[20] Kouji Kashiwa, Yuto Mori, and Akira Ohnishi. Controlling the model sign problem via the path optimization method: Monte carlo approach to a qcd effective model with polyakov loop. Phys.Rev.D, 99(1):014033, 2019.

[21] Kouji Kashiwa, Yuto Mori, and Akira Ohnishi. Application of the path optimization method to the sign problem in an effective model of qcd with a repulsive vector-type interaction. Phys.Rev.D, 99(11):114005, 2019.

[22] C.A. Baker et al. An improved experimental limit on the electric dipole moment of the neutron. Phys.Rev.Lett., 97:131801, 2006.

[23] J. M. Pendlebury et al. Revised experimental upper limit on the electric dipole moment of the neutron. Phys. Rev. D, 92(9):092003, 2015.

[24] R. D. Peccei and Helen R. Quinn. CP conservation in the presence of instantons. Phys. Rev. Lett., 38:1440–1443, 1977. [,328(1977)].

[25] R.D. Peccei and Helen R. Quinn. Constraints imposed by cp conservation in the presence of instantons. Phys.Rev.D, 16:1791–1797, 1977.

[26] Steven Weinberg. A new light boson? Phys.Rev.Lett., 40:223–226, 1978.

[27] Frank Wilczek. Problem of strong p and t invariance in the presence of instantons. Phys.Rev.Lett., 40:279–282, 1978.

[28] Davide Gaiotto, Anton Kapustin, Zohar Komargodski, and Nathan Seiberg. Theta, time reversal, and temperature. JHEP, 05:091, 2017.

[29] Ryuichiro Kitano, Takao Suyama, and Norikazu Yamada. $\theta = \pi$ in $su(n)/\mathbb{Z}\_n$ gauge theories. JHEP, 09:137, 2017.

[30] Naoto Kan, Ryuichiro Kitano, Shimon Yankielowicz, and Ryo Yokokura. From 3d dualities to hadron physics.

[31] Andrei Parnachev and Ariel R. Zhitnitsky. Phase transitions, theta behavior and instantons in qcd and its holographic model. Phys.Rev.D, 78:125002, 2008.

[32] Sergei Dubovsky, Albion Lawrence, and Matthew M. Roberts. Axion monodromy in a model of holographic gluodynamics. JHEP, 02:053, 2012.

[33] Francesco Bigazzi, Aldo L. Cotrone, and Roberto Sisca. Notes on theta dependence in holographic yang-mills. JHEP, 08:090, 2015.

[34] Daniel Arean, Ioannis Iatrakis, Matti Jarvinen, and Elias Kiritsis. Cp-odd sector and θ dynamics in holographic qcd. Phys.Rev.D, 96(2):026001, 2017.

[35] Ryuichiro Kitano, Norikazu Yamada, and Masahito Yamazaki. Is $N = 2$ Large? 10 2020.

[36] Ettore Vicari and Haralambos Panagopoulos. Theta dependence of su(n) gauge theories in the presence of a topological term. Phys.Rept., 470:93–150, 2009.

[37] Mitsuaki Hirasawa, Akira Matsumoto, Jun Nishimura, and Atis Yosprakob. Complex Langevin analysis of 2D U(1) gauge theory on a torus with a θ term. JHEP, 09:023, 2020.

[38] U.J. Wiese. Numerical simulation of lattice θ vacua: The 2-d u(1) gauge theory as a test case. Nucl.Phys.B, 318:153–175, 1989.

[39] B. E. Rusakov. Loop averages and partition functions in U(N) gauge theory on two-dimensional manifolds. Mod. Phys. Lett., A5:693–703, 1990.

[40] Claudio Bonati and Paolo Rossi. Topological susceptibility of two-dimensional $U(N)$ gauge theories. Phys. Rev., D99(5):054503, 2019.

[41] Ahmed S. Hassan, Masahiro Imachi, Norimasa Tsuzuki, and Hiroshi Yoneyama. Character expansion, zeros of partition function and theta term in u(1) gauge theory. Prog.Theor.Phys., 94:861–872, 1995.

[42] Jan C. Plefka and Stuart Samuel. Monte Carlo studies of two-dimensional systems with a theta term. Phys. Rev., D56:44–54, 1997.

[43] Yoshinobu Kuramashi and Yusuke Yoshimura. Tensor renormalization group study of two-dimensional U(1) lattice gauge theory with a θ term. JHEP, 04:089, 2020.

[44] Christof Gattringer and Oliver Orasch. Density of states approach for lattice QCD with a θ-term. 4 2020.

[45] Erhard Seiler, Denes Sexty, and Ion-Olimpiu Stamatescu. Gauge cooling in complex Langevin for QCD with heavy quarks. Phys. Lett., B723:213–216, 2013.

[46] Shi Chen, Kenji Fukushima, Hiromichi Nishimura, and Yuya Tanizaki. Deconfinement and $\mathcal{CP}$ breaking at $\theta = \pi$ in Yang-Mills theories and a novel phase for SU(2). Phys. Rev. D, 102(3):034020, 2020.

[47] N. Ishibashi, H. Kawai, Y. Kitazawa, and A. Tsuchiya. A Large N reduced model as superstring. Nucl. Phys. B, 498:467–491, 1997.

[48] Tohru Eguchi and Hikaru Kawai. Reduction of Dynamical Degrees of Freedom in the Large N Gauge Theory. Phys. Rev. Lett., 48:1063, 1982.

[49] David J. Gross and Yoshihisa Kitazawa. A Quenched Momentum Prescription for Large N Theories. Nucl. Phys. B, 206:440–472, 1982.

[50] Alfred Schild. Classical Null Strings. Phys. Rev. D, 16:1722, 1977.

[51] Michael B. Green, John H. Schwarz, and Lars Brink. Superfield Theory of Type II Superstrings. Nucl. Phys. B, 219:437–478, 1983.

[52] Masafumi Fukuma, Hikaru Kawai, Yoshihisa Kitazawa, and Asato Tsuchiya. String field theory from IIB matrix model. Nucl. Phys. B, 510:158–174, 1998.

[53] Jun Nishimura and Fumihiko Sugino. Dynamical generation of four-dimensional space-time in the IIB matrix model. JHEP, 05:001, 2002.

[54] H. Kawai, Shoichi Kawamoto, Tsunehide Kuroki, T. Matsuo, and S. Shinohara. Mean field approximation of IIB matrix model and emergence of four-dimensional space-time. Nucl. Phys. B, 647:153–189, 2002.

[55] T. Aoyama and H. Kawai. Higher order terms of improved mean field approximation for IIB matrix model and emergence of four-dimensional space-time. Prog. Theor. Phys., 116:405–415, 2006.

[56] Jun Nishimura, Toshiyuki Okubo, and Fumihiko Sugino. Systematic study of the SO(10) symmetry breaking vacua in the matrix model for type IIB superstrings. JHEP, 10:135, 2011.

[57] Konstantinos N. Anagnostopoulos, Takehiro Azuma, and Jun Nishimura. Monte Carlo studies of the spontaneous rotational symmetry breaking in dimensionally reduced super Yang-Mills models. JHEP, 11:009, 2013.

[58] Konstantinos N. Anagnostopoulos, Takehiro Azuma, Yuta Ito, Jun Nishimura, and Stratos Kovalkov Papadoudis. Complex Langevin analysis of the spontaneous symmetry breaking in dimensionally reduced super Yang-Mills models. JHEP, 02:151, 2018.

[59] Konstantinos N. Anagnostopoulos, Takehiro Azuma, Yuta Ito, Jun Nishimura, Toshiyuki Okubo, and Stratos Kovalkov Papadoudis. Complex Langevin analysis of the spontaneous breaking of 10D rotational symmetry in the Euclidean IKKT matrix model. 2 2020.

[60] Sang-Woo Kim, Jun Nishimura, and Asato Tsuchiya. Expanding (3+1)-dimensional universe from a Lorentzian matrix model for superstring theory in (9+1)-dimensions. Phys. Rev. Lett., 108:011601, 2012.

[61] Yuta Ito, Sang-Woo Kim, Jun Nishimura, and Asato Tsuchiya. Monte Carlo studies on the expanding behavior of the early universe in the Lorentzian type IIB matrix model. PoS, LATTICE2013:341, 2014.

[62] Yuta Ito, Jun Nishimura, and Asato Tsuchiya. Power-law expansion of the Universe from the bosonic Lorentzian type IIB matrix model. JHEP, 11:070, 2015.

[63] Toshihiro Aoki, Mitsuaki Hirasawa, Yuta Ito, Jun Nishimura, and Asato Tsuchiya. On the structure of the emergent 3d expanding space in the Lorentzian type IIB matrix model. PTEP, 2019(9):093B03, 2019.

[64] G. Parisi and Yong-shi Wu. Perturbation Theory Without Gauge Fixing. Sci. Sin., 24:483, 1981.

[65] Gert Aarts, Pietro Giudice, and Erhard Seiler. Localised distributions and criteria for correctness in complex Langevin dynamics. Annals Phys., 337:238–260, 2013.

[66] Gert Aarts, Frank A. James, Erhard Seiler, and Ion-Olimpiu Stamatescu. Adaptive stepsize and instabilities in complex Langevin dynamics. Phys. Lett. B, 687:154–159, 2010.

[67] Zhenning Cai, Yana Di, and Xiaoyu Dong. How does Gauge Cooling Stabilize Complex Langevin? 2019.

[68] Jun Nishimura and Shinji Shimasaki. New Insights into the Problem with a Singular Drift Term in the Complex Langevin Method. Phys. Rev. D, 92(1):011501, 2015.

[69] Gert Aarts, Erhard Seiler, Denes Sexty, and Ion-Olimpiu Stamatescu. Complex Langevin dynamics and zeroes of the fermion determinant. JHEP, 05:044, 2017. [Erratum: JHEP 01, 128 (2018)].

[70] A. Mollgaard and K. Splittorff. Complex Langevin Dynamics for chiral Random Matrix Theory. Phys. Rev. D, 88(11):116007, 2013.

[71] Jeff Greensite. Comparison of complex Langevin and mean field methods applied to effective Polyakov line models. Phys. Rev. D, 90(11):114507, 2014.

[72] Manuel Scherzer, Erhard Seiler, Dénes Sexty, and Ion-Olimpiu Stamatescu. Complex Langevin and boundary terms. Phys. Rev. D, 99(1):014512, 2019.

[73] M. Scherzer, E. Seiler, D. Sexty, and I.-O. Stamatescu. Controlling Complex Langevin simulations of lattice models by boundary term analysis. Phys. Rev. D, 101(1):014501, 2020.

[74] Yusuke Namekawa. Comparative study of topological charge. PoS, LATTICE2014:344, 2015.

[75] Constantia Alexandrou, Andreas Athenodorou, Krzysztof Cichy, Arthur Dromard, Elena Garcia-Ramos, Karl Jansen, Urs Wenger, and Falk Zimmermann. Comparison of topological charge definitions in Lattice QCD. Eur. Phys. J. C, 80(5):424, 2020.

[76] P. Di Vecchia, K. Fabricius, G.C. Rossi, and G. Veneziano. Preliminary Evidence for U(1)-A Breaking in QCD from Lattice Calculations. pages 426–442, 5 1981.

[77] G.G. Batrouni, G.R. Katz, Andreas S. Kronfeld, G.P. Lepage, B. Svetitsky, and K.G. Wilson. Langevin Simulations of Lattice Field Theories. Phys. Rev. D, 32:2736, 1985.

[78] M. Fukugita, Y. Oyanagi, and A. Ukawa. Langevin Simulation of the Full {QCD} Hadron Mass Spectrum on a Lattice. Phys. Rev. D, 36:824, 1987.

[79] Martin Luscher and Stefan Schaefer. Lattice QCD without topology barriers. JHEP, 07:036, 2011.

[80] Christopher Czaban, Arthur Dromard, and Marc Wagner. Studying and removing effects of fixed topology. Acta Phys. Polon. Supp., 7(3):551, 2014.

[81] Simon Mages, Balint C. Toth, Szabolcs Borsanyi, Zoltan Fodor, Sandor D. Katz, and Kalman K. Szabo. Lattice QCD on nonorientable manifolds. Phys. Rev. D, 95:094512, 2017.

[82] Wolfgang Bietenholz, Christopher Czaban, Arthur Dromard, Urs Gerber, Christoph P. Hofmann, Héctor Mejía-Díaz, and Marc Wagner. Interpreting Numerical Measurements in Fixed Topological Sectors. Phys. Rev. D, 93(11):114516, 2016.

[83] Wolfgang Bietenholz, Krzysztof Cichy, Philippe de Forcrand, Arthur Dromard, and Urs Gerber. The Slab Method to Measure the Topological Susceptibility. PoS, LATTICE2016:321, 2016.

[84] Martin Hasenbusch. Fighting topological freezing in the two-dimensional CP^{N-1} model. EPJ Web Conf., 175:02004, 2018.

[85] Werner Krauth, Hermann Nicolai, and Matthias Staudacher. Monte Carlo approach to M theory. Phys. Lett. B, 431:31–41, 1998.

[86] Peter Austing and John F. Wheater. Convergent Yang-Mills matrix theories. JHEP, 04:019, 2001.

[87] Yuta Ito, Jun Nishimura, and Asato Tsuchiya. Universality and the dynamical space-time dimensionality in the Lorentzian type IIB matrix model. JHEP, 03:143, 2017.

[88] Yuta Ito, Sang-Woo Kim, Yuki Koizuka, Jun Nishimura, and Asato Tsuchiya. A renormalization group method for studying the early universe in the Lorentzian IIB matrix model. PTEP, 2014(8):083B01, 2014.

[89] Takehiro Azuma, Yuta Ito, Jun Nishimura, and Asato Tsuchiya. A new method for probing the late-time dynamics in the Lorentzian type IIB matrix model. PTEP, 2017(8):083B03, 2017.

[90] Jun Nishimura and Asato Tsuchiya. Complex Langevin analysis of the space-time structure in the Lorentzian type IIB matrix model. JHEP, 06:077, 2019.

[91] Kohta Hatakeyama, Akira Matsumoto, Jun Nishimura, Asato Tsuchiya, and Atis Yosprakob. The emergence of expanding space–time and intersecting D-branes from classical solutions in the Lorentzian type IIB matrix model. PTEP, 2020(4):043B10, 2020.

[92] Jean-Michel Drouffe and Jean-Bernard Zuber. Strong coupling and mean field methods in lattice gauge theories. Phys. Rept., 102:1, 1983.